

## ***Saccharomyces cerevisiae* Rev7 promotes non-homologous end-joining by blocking Mre11 nuclease and Rad50's ATPase activities and homologous recombination**

Sugith Badugu,<sup>1,2</sup> Kshitiza M. Dhyani,<sup>1,2</sup> Manoj Thakur<sup>3</sup> and Kalappa Muniyappa<sup>1\*</sup>

<sup>1</sup>Department of Biochemistry, Indian Institute of Science, Bengaluru 560012,<sup>3</sup>Sri Venkateswara College, University of Delhi, New Delhi 110021, India

<sup>2</sup>Authors contributed equally to this work and are listed alphabetically

\*Corresponding authors: E-mail: kmbc@iisc.ac.in; Tel.: +91 80 2293 2235

### **IMPACT STATEMENT**

The mechanisms steering DNA double-strand break repair pathway choice is a topic of intense investigation, but remains incompletely understood. Our findings suggest that yeast Rev7 promotes DSB repair via NHEJ and inhibits homologous recombination by blocking Mre11 nuclease and Rad50's ATPase activities.

### **ABSTRACT**

Recent studies have shown that, in human cancer cells, the tetrameric Shieldin complex (comprising REV7, SHLD1, SHLD2, and SHLD3) facilitates non-homologous end-joining (NHEJ) while blocking homologous recombination (HR). Surprisingly, several eukaryotic species lack SHLD1, SHLD2 and SHLD3 orthologs, suggesting that Rev7 may leverage an alternative mechanism to regulate the double-strand break (DSB) repair pathway choice. Exploring this hypothesis, we discovered that *Saccharomyces cerevisiae* Rev7 physically interacts with the Mre11-Rad50-Xrs2 (MRX) subunits, impedes G-quadruplex DNA synergised-HU-induced toxicity and facilitates NHEJ, while antagonizing HR. Notably, we reveal that a 42-amino acid C-terminal fragment of Rev7 binds to the subunits of MRX complex, protects *rev7Δ* cells from G-quadruplex DNA-HU-induced toxicity, and promotes NHEJ by blocking HR. By comparison, the N-terminal HORMA domain, a conserved protein–protein interaction

module, was dispensable. We further show that the full-length Rev7 impedes Mre11 nuclease and Rad50's ATPase activities without affecting the latter's ATP-binding ability. Combined, these results provide unanticipated insights into the functional interaction between the MRX subunits and Rev7 and highlight a mechanism by which Rev7 facilitates DSB repair via NHEJ, and attenuation of HR, by blocking Mre11 nuclease and Rad50's ATPase activities in *S. cerevisiae*.

## INTRODUCTION

A hallmark of low fidelity DNA polymerases, also known as DNA translesion synthesis polymerases (TLS polymerases), with no detectable proofreading activity, is their ability to catalyse DNA synthesis across a variety of bulky, helix-distorting DNA lesions (**Prakash et al., 2005; Vaisman et al., 2017; Maiorano et al., 2021; Ling et al., 2022**). The TLS polymerases are also involved in a plethora of cellular processes, including but not limited to epigenetics, immune signalling, viral mutagenesis and cancer development (**Paniagua and Jacobs, 2023**). Indeed, translesion DNA synthesis is a source of mutagenesis, potentially contributing to the development of cancer and drug resistance (**Lange et al., 2011; Baranovskiy et al., 2012; Pilzecker et al., 2019**). The *Saccharomyces cerevisiae* TLS Pol $\zeta$  (henceforth referred to as ScPol $\zeta$ ) is a four-subunit enzyme, comprised of catalytic subunit Rev3, two regulatory subunits of Rev7 and the accessory subunits Pol31 and Pol32 (**Johnson et al., 2012; Makarova et al., 2012**). Current evidence suggests that the error rate during ScPol $\zeta$ -catalysed replication of undamaged DNA templates is much higher than that of DNA polymerases, as it lacks 3'-to-5' proofreading exonuclease activity (**Lawrence et al., 1985a; 1985b; Huang et al., 2002; Northam et al., 2006; Zhong et al., 2006; Kochanova et al., 2017**). Consistent with this, *S. cerevisiae rev3, rev7* or *pol32* mutant strains show greatly reduced spontaneous mutation frequencies, confirming that ScPol $\zeta$  is responsible for DNA damage-induced mutagenesis (**Quah et al., 1980; Lawrence et al., 1985a; 1985b; Morrison et al., 1989; Nelson et al., 1996; Makarova et al., 2015**).

The TLS Pol $\zeta$  exists in a wide range of unicellular and multicellular eukaryotes, including fungi, plants, and animals (**Maiorano et al., 2021; Ling et al., 2022**;

**Paniagua and Jacobs, 2023).** While the catalytic subunit Rev3 alone is capable of replicating damaged DNA, Rev7 enhances its catalytic efficiency by twenty- to thirtyfold (**Quah et al., 1980; Morrison et al., 1989; Nelson et al., 1996, Makarova et al., 2015**) and the accessory subunits Pol31 and Pol32 further raise it by three- to tenfold (**Johnson et al., 2012; Makarova et al., 2012**), suggesting that they abet the processivity of translesion DNA synthesis by Pol $\zeta$  (**Acharya et al., 2006; Bezalel-Buch et al., 2020**). Indeed, Rev7 (also known as MAD2B and MAD2L2) is an adapter protein, which acts as a bridge between Rev3 and Rev1 (**Haracska et al., 2001; Kikuchi et al., 2012; Pustovalova et al., 2012**). Various structural and biochemical investigations have uncovered unique structural features of Pol $\zeta$ , wherein its subunits interact with each other to form a highly proficient, multi-subunit TLS holoenzyme (**Gómez-Llorente et al., 2013; Malik et al., 2020; Du Truong et al., 2021**). The high-resolution cryo-EM structures of ScPol $\zeta$  holoenzyme have revealed that the subunits Rev3, Rev7, Pol31, and Pol32 assemble into a pentameric ring-shaped structure in which they are maintained by a chain of uninterrupted protein-protein interaction networks (**Gómez-Llorente et al., 2013; Malik et al., 2020; Du Truong et al., 2021**). Precise details of how Pol $\zeta$  holoenzyme achieves its substrate specificity have not been fully understood. Shedding light on this, A. Aggarwal's lab has recently provided insights into the mechanism by which the active site of ScPol $\zeta$  responds to the A:C mismatched duplex DNA distortion (**Malik et al., 2022**).

A flurry of research has documented that the tetrameric Shieldin complex - comprising REV7, SHLD1, SHLD2 and SHLD3 – binds single-stranded DNA (ssDNA), blocks 5' end resection and homologous recombination (HR), antagonizes the recruitment of BRCA1 to the DSB, while facilitating non-homologous end-joining (NHEJ) (**Xu et al., 2015; Boersma et al., 2015; Mirman et al., 2018; Findlay et al., 2018; Gupta et al., 2018; Ghezraoui et al., 2018; Dev et al., 2018; Tomida et al., 2018; Gao et al., 2018; Noordermeer et al., 2018; Liang et al., 2020**). Investigations have also shown that the N-terminus of SHLD3 interacts with REV7 using a stereotypical “safety-belt” interaction mechanism (**Gupta et al., 2018; Ghezraoui et al., 2018; Dev et al., 2018; Tomida et al., 2018; Gao et al., 2018; Noordermeer et al., 2018; Liang et al., 2020; Clairmont et al., 2020; Dai et al., 2020**). In the alternative pathway, Shieldin-53BP1-RIF1 counteracts DSB resection and recruits the CST-Pol $\alpha$ -primase complex to promote fill-in at the resected DNA ends (**Mirman et al., 2018; 2022; 2023**). Cells

derived from Fanconi anaemia patients, caused by biallelic *REV7* mutations, display hypersensitivity to DNA cross-linking agents, accumulate chromosome breaks during S/G2 phase of the cell cycle and activation of the p53/p21 axis (**Bluteau et al., 2016**), revealing its critical role in providing protection against FA disease. It is worth pointing out that Rev7 inhibits the anaphase-promoting complex by sequestering Cdh1, and modulates the transition from metaphase to anaphase, thereby contributing to mitotic fidelity (**Listovsky and Sale, 2013; Vaisman et al., 2017; Ling et al., 2022**). However, a mechanistic understanding of how Rev7 regulates cell cycle events and how such roles differ or relate to its role in TLS remains underexplored. Although the emphasis of the findings differ, the fact that Rev7 functions as an anti-resection factor has spurred a new wave of experiments on DNA repair pathways (**Setiaputra and Durocher, 2019; Clairmont and D'Andrea, 2021**).

At DSBs in *S. cerevisiae*, the Mre11–Rad50–Xrs2 (MRX) in conjunction with Sae2 first catalyses endonucleolytic cleavage of 5'-terminated DNA strands and then its 3'→5' exonucleolytic activity produces a short 3'-ssDNA overhang, which is followed by resection in a 5'→3' direction by either Exo1 or Dna2–Sgs1 complex to produce long tracks of ssDNA that are critically important for HR (**Cejka and Symington, 2021**). As such, the mechanism by which cells restrain over-resection of DSBs remains incompletely understood, although hyper-resection could potentially hinder optimal HR and trigger genomic instability. Surprisingly, however, Shieldin orthologs are absent in different organisms such as yeast, fruit fly, nematode worm, zebrafish and frog (**Setiaputra and Durocher, 2019**). Consequently, we hypothesized that Rev7 in *S. cerevisiae* (hereafter referred to as ScRev7) may recruit an unknown functional equivalent(s) of Shieldin orthologs to regulate the DSB repair pathway choice between HR and NHEJ. Thus, an alternative mechanism might involve the MRX complex on the basis of current knowledge that it plays multiple roles in signalling, processing and repair of DSBs (**Cejka and Symington, 2021**). In this study, we provide robust evidence that ScRev7, via its 42-aminoacid C-terminal fragment in the “safety belt” region, physically interacts with the Mre11, Rad50 or Xrs2 subunits, protects *rev7Δ* cells from G-quadruplex DNA/HU-induced toxicity and facilitates DSB repair via NHEJ while antagonizing HR. Mechanistic studies revealed that ScRev7 binds to the MRX subunits with sub-micromolar affinity, attenuates Mre11 nuclease and Rad50's ATPase activities, without affecting the ability of the latter to bind ATP. Collectively,

our findings not only provide evidence for functional interaction between Rev7 and the MRX subunits, but also reveal novel insights into how Rev7 regulates the pathway choice between HR and NHEJ in *S. cerevisiae*.

## RESULTS

### ScRev7 interacts with the MRX subunits

As noted above, studies in cancer cells have shown that the Rev7-Shieldin effector complex facilitates NHEJ by blocking 5' end resection and HR (Xu *et al.*, 2015; Boersma *et al.*, 2015; Mirman *et al.*, 2018; Findlay *et al.*, 2018; Gupta *et al.*, 2018; Ghezraoui *et al.*, 2018; Cejka and Symington, 2021). Since there are no identifiable Shieldin orthologs in *S. cerevisiae* (Setiaputra and Durocher, 2019), we began our investigations with a hypothesis that Rev7 may recruit alternative factors such as the MRX subunits to block HR and enable NHEJ. To this end, yeast two-hybrid assay (Y2H) was leveraged for the purpose of studying binary protein-protein interactions between ScRev7 and the subunits of MRX complex, whereas in follow-up studies we mapped the minimal region of ScRev7 required for its association with the MRX subunits. The yeast strain PJ69-4A was co-transformed with plasmids (prey vectors) encoding the Mre11, Rad50 or Xrs2 subunits fused to GAL4 activation domain and ScRev7 fused to the GAL4 DNA-binding domain (bait vector). The positive colonies were selected on SC-/Trp-Leu-His dropout nutrient medium containing 3-aminotriazole (3-AT) (Fields and Song, 1989; James *et al.*, 1996). Remarkably, we found interactions between Rev7 and the Mre11, Rad50 and Xrs2 subunits (**Figure 1A**), whereas cells bearing empty vector and a plasmid expressing Mre11, Rad50 or Xrs2 subunits did not. Consistent with results from prior research (Rizzo *et al.*, 2018), yeast cells transformed with prey and bait vectors expressing Rev7 showed robust growth (**Figure 1A**), indicating the assembly of Rev7 homodimers, which served as a positive control. In an analogous experiment, cells co-transformed with bait and prey vectors expressing Sae2 and Rev7, respectively, failed to grow in different strain backgrounds (**bottom panel of Figure 1A-C**), indicating lack of binary interaction between Sae2 and Rev7. Collectively, these results confirmed the binding specificity of Rev7 to the subunits of MRX complex.

Given that Rev3 has also been implicated in HR-mediated DSB repair (**Sonoda et al., 2003**), we asked whether the MRX subunits interact with ScRev7 in the *rev3Δ* mutant strain. To address this question, the *S. cerevisiae rev3Δ* strain was co-transformed with a combination of bait (pGBKT7 or pGBKT7-REV7) and prey vectors (pGADT7, pGADT7-REV7, pGADT7-*MRE11*, pGADT7-*RAD50*, pGADT7-*XRS2* or pGADT7-*SAE2*). Interestingly, we observed binary interactions between the subunits of MRX complex and ScRev7 in the *rev3Δ* mutant in the Y2H system (**Figure 1B**), indicating that Rev3 is dispensable for the binding of ScRev7 to the MRX subunits. Analogously ScRev7 showed binary interactions with the subunits of MRX complex in the *mre11Δ rad50Δ xrs2Δ* triple mutant strain (**Figure 1C**), thereby confirming that their association is independent of endogenous MRX subunits.

### ScRev7 physically interacts with the MRX subunits

Microscale thermophoresis (MST) allows for quantitative analysis of protein-protein interactions in free solution (**Wienken et al., 2010**). Since the binding of ScRev7 to the MRX subunits was unanticipated, we sought to validate their interaction by an orthogonal assay and determine their binding affinities using purified proteins. To this end, we purified eGFP-tagged ScRev7 (**Figure 1—figure supplement 1A**), confirmed its identity (**Figure 1—figure supplement 2**), and leveraged MST titration approach to measure its binding affinity to purified Mre11, Rad50, Xrs2 and Rev1 subunits, and also to the Mre11-Rad50 complex (**Figure 1—figure supplement 1C, D**). The MST signals were plotted as a function of ligand concentration (**Figure 1—figure supplement 3A-F**). Normalized MST data were fitted to a logistic binding curve, resulting in an apparent dissociation constants ( $K_d$ ) of  $0.16 \pm 0.07$ ,  $0.23 \pm 0.06$  and  $0.18 \pm 0.03 \mu\text{M}$  for Rad50, Mre11 subunits and Mre11-Rad50 complex, respectively, which is two- to threefold greater as compared with Xrs2 (**Figure 1D**). *S. cerevisiae* Rev1 was used as a positive control to ensure the accuracy of the Y2H assay. The binding kinetics measured demonstrated that purified Rev1 (**Figure 1—figure supplement 1D**) bound to Rev7 with an affinity (**Figure 1D** and **Figure 1—figure supplement 3D**), comparable to previously reported value (**Rizzo et al., 2018; Guo et al., 2003**). On the other hand, negative controls such as purified Sae2 (**Figure 1—figure supplement 1E**) and eGFP showed no significant binding to the MRX subunits and GFP-tagged Rev7, respectively (**Figure 1—figure supplement 3F**). We next tested the affinity of Rev7-C1 for the Mre11, Rad50 and MR complex. The results

showed that Rev7C1 binds to Mre11 with approximately 3-fold reduced affinity and to the Rad50 and MR complex with 10-fold reduced affinity (**Figure 1—figure supplement 4**). Collectively, these results confirm the specificity of interaction between Rev7 and the MRX subunits. It is also noteworthy that the Hill coefficients ( $n_H$ ) indicate larger than one, implying positive cooperativity (**Figure 1D**). The quantitative assessment of binding affinities together with Y2H data suggest that Rev7 robustly interacts with the MRX subunits.

### A 42-aminoacid C-terminal segment of Rev7 is critical for its interaction with the MRX subunits

Since the data obtained from the Y2H screening system and MST based protein–protein interaction assay suggested pairwise association between the subunits of MRX complex and Rev7, we sought to identify the functional domain(s) in the ScRev7 required for interaction with the MRX subunits. For this purpose, we generated three N-terminally truncated and an equal number of C-terminally truncated variants. We refer to these variants as Rev7-N1; Rev7-N2; Rev7-N3, and Rev7-C1, Rev7-C2 and Rev7-C3, respectively (**Figure 2A**). We then asked whether these variants bind to the MRX subunits and enable the growth of yeast cells on selection nutrient medium. Our experiments surprisingly revealed that cells expressing the ScRev7 N-terminally truncated variants showed robust cell growth (**bottom panel of Figure 2B**) similar to the WT (**Figure 1A-C**), indicating that they interact with the subunits of MRX complex. Further, these results indicated that the Rev7's N-terminal HORMA domain (residues 1-149), an evolutionarily conserved protein–protein interaction module, is dispensable for binding to the MRX subunits (**Figure 2B**). Notwithstanding, we do not exclude the possibility that it may play a role that is undetectable by the Y2H assay.

Next, we performed Y2H experiments using the C-terminally truncated species (**Figure 2A**) and found that deletion of C-terminal forty-two amino acid residues (i.e., 203-245) resulted in loss of cell proliferation and growth (**bottom panel of Figure 2C**). Similarly, deletion of the C-terminal 150 to 203 amino acid residues of ScRev7 abrogated yeast cell growth (**Figure 2C**). These results indicate that the C-terminal 42-residue segment of ScRev7 is critical for its interaction with the MRX subunits. To further confirm these results, an Y2H experiment was carried out with cells co-

expressing 42 aa peptide and the Mre11, Rad50 or Xrs2 subunits. Such an analysis showed that the ScRev7's 42 residue peptide alone was sufficient for interaction with each subunit of the MRX complex (**Figure 2—figure supplement 1**). However, it remained possible that the inability of cells expressing the C-terminally truncated variants of ScRev7 (with appropriate prey proteins) to grow in selection medium (**Figure 2C, bottom panel**) may be due to altered expression or decreased abundance of truncated species. To explore this possibility, whole cell lysates derived from cells expressing the N- and C-terminally truncated variants, tagged with c-Myc epitope at the N-terminus, were resolved by SDS-PAGE and probed with anti-c-Myc antibody. Reassuringly, the results revealed comparable levels of N- and C-terminally truncated species of ScRev7 in the whole cell lysates of strains that were employed for Y2H analyses (**Figure 2—figure supplement 2**).

### **Models predicted by AlphaFold-Multimer reveal that Mre11 and Rad50 subunits independently associate with Rev7**

To further characterize the interaction between the MRX subunits and ScRev7, a structure prediction algorithm, AF2-multimer (**Evans et al., 2022**), was leveraged to construct structural models of ScRev7-Mre11 and ScRev7-Rad50 heterodimers. The models with the high pLDDT scores were considered for further analysis. Strikingly, the models indicated that Mre11 and Rad50 binding surfaces overlap with ScRev7, suggesting that the latter can bind these subunits (**Figure 2—figure supplement 3**). In the model of Rev7-Mre11 complex, residues Asp 206 and Ile 240 in the Rev7 C-terminal “safety belt region” (green) mediate dimerization with Mre11 through residues Asp 131 and Arg 181. Interestingly, His 127 in the Rev7 N-terminal HORMA domain also contribute its binding to Asp 131 of Mre11 (**Figure 2—figure supplement 3A, Supplementary Table S1**). Furthermore, modelling studies of Rev7-Rad50 complex showed that the ScRev7 C-terminal residues Lys 168, Glu 184, Asn 189 and Asp 188 mediate dimerization with ScRad50 via residues Glu 577, Lys 596 and Arg 603 (**Figure 2—figure supplement 3B, Supplementary Table S2**). Curiously, the AF2-multimer models also revealed that amino acid residues outside of the 42-residue fragment also contribute to pairwise interactions between Rev7 and the Mre11 and Rad50 subunits, although Y2H assays did not identify such interaction. Indeed, similar findings have been previously noted for several other interacting partners (**You et al., 2006; Koegl and Uetz, 2007; Hoff et al., 2010**).

## The Rev7's C-terminal 42-residue fragment mitigates the G-quadruplex-HU induced toxic effects

Several studies have documented the genome-wide prevalence of G-quadruplex DNA structures in various organisms ranging from viruses to humans, which play regulatory roles in diverse cellular processes (**Rhodes and Lipps, 2015; Spiegel et al., 2020; Yadav et al., 2021**). For instance, it has been shown that Rev1-deficient chicken DT40 cells exhibit defects in replicating G quadruplex-forming motifs (**Sarkies et al., 2010, 2012**). Similarly, computational and genetic studies in *S. cerevisiae* have revealed that G-quadruplex-forming motifs cause slow growth in replication stressed Pif1-deficient cells and affect genome integrity (**Capra et al., 2010; Paeschke et al., 2011, 2013**). Inspired by these findings, we sought to understand whether ScRev7 plays a role in genome maintenance using the assay developed by the V. Zakian's lab (**Paeschke et al., 2011**). We first compared the viability of *rev7Δ* mutant cells devoid of exogenous G-quadruplex forming sequences with that of WT under conditions of optimal growth and HU-induced replication stress. This analysis revealed that, like the WT, *rev7Δ* mutant cells grew robustly in the absence or presence of HU (**Figure 3A**).

Next, we next sought to determine whether the G-quadruplex DNA motifs affect cell viability in the absence and presence of HU. To address this question, we tested the effect of exogenous G-quadruplex forming sequences, positioned on either the leading or lagging template strands, on the viability of WT and *rev7Δ* mutant strains, relative to cells expressing the ScRev7 variants (Rev7-C1 or 42-residue C-terminal peptide) on SC/-Leu medium lacking HU. We found that all strains used in this experiment showed comparable growth phenotypes on this medium (**Figure 3B**). On the other hand, *rev7Δ* mutant and the strains expressing the variant Rev7-C1 were highly sensitive to exposure to HU when compared to the wild type cells (**Figure 3C**). Remarkably, however, cells expressing the Rev7's 42-residue C-terminal peptide exhibited robust growth in the same medium containing HU (**Figure 3C**). Combining the results presented, we suggest that the 42-residue C-terminal peptide, but not Rev7-C1 variant, confers protection to cells from the toxic effects of HU/G-quadruplex

DNA forming sequences, regardless of whether they occur in the leading or lagging template strands.

### Rev7 inhibits Mre11 nucleolytic activities

Decades of work has documented that Mre11 is a Mn<sup>2+</sup>-dependent bifunctional enzyme with both endo- and exonuclease activities, which are critical for DNA end resection (Paull and Gellert, 1998; Tsubouchi and Ogawa, 1998; Ghosal and Muniyappa, 2007; Stracker and Petrini, 2011; Ghodke and Muniyappa, 2013; Paull, 2018; Casari *et al.*, 2019). Further, it has been demonstrated that Mre11 cleaves non-B DNA structures such as DNA hairpins, as well as intra- and intermolecular G-quadruplex structures (Trujillo and Sung, 2001; Lobachev *et al.*, 2002; Ghosal and Muniyappa, 2005; 2007). To further explore the functional significance of complex formation between Rev7 and Mre11, ScRev7 and its truncated derivative ScRev7-C1 were expressed in and purified from *E. coli* whole cell lysates to homogeneity (**Figure 4A and 4B**). We then performed an experiment in which equimolar amounts of MRX subunits were incubated with 5'-<sup>32</sup>P-labelled dsDNA in the presence or absence of ScRev7. The reaction products were analyzed as previously described (Ghosal and Muniyappa, 2005). The results informed that (a) ScRev7 has no nuclease activity (**Figure 5A, Lane 2**) and (b) Mre11 cleaved <sup>32</sup>P-labelled dsDNA, generating a pattern of DNA fragments in a ladder-like pattern (**Figure 5A, Lane 3**). Subsequently, we investigated the effect of ScRev7 on MRX nuclease activity by co-incubating various concentrations of ScRev7 and a fixed amount of MRX complex, prior to the addition of 5'-<sup>32</sup>P-labelled dsDNA. We detected a notable and substantial inhibition in the MRX complex-mediated DNA cleavage activity, and almost complete inhibition at 2 μM (**Figure 5A, lanes 4-12**). We carried out additional experiments to test the effect Rev7-C1 on Mre11 nuclease activity. By comparison, the efficiency of inhibition was expectedly less than that of full-length ScRev7. Curiously, we note that the ScRev7-C1 does not faithfully recapitulate the Y2H results. One possible reason is that amino acid residues in the ScRev7-C1 fragment interact with Mre11 and cause partial inhibition, in good agreement with the AF2 modeling data (**Figure 2—figure supplement 2**).

Many studies have demonstrated that Mre11 exhibits both endonuclease and exonuclease activities independently of Rad50 and Xrs2 subunits (**Cejka and Symington, 2021**). Thus, we next examined the effect of ScRev7 on the Mre11 ssDNA-specific endonuclease activity in reactions lacking Rad50 and Xrs2. In accord with previous studies, Mre11 digested all the input ssDNA substrate into small fragments/nucleotides in a manner dependent on its concentration (**Figure 5C**). Interestingly, we found that the addition of increasing concentrations of ScRev7 coincided with a concomitant decrease in the Mre11 endonuclease activity (**Figure 5D**). To ascertain the specificity, the effect of ScRev7 on Sae2's endonuclease activity was investigated. As expected (**Lengsfeld et al., 2007; Ghodke et al., 2016**), Sae2 exhibited concentration-dependent nuclease activity on dsDNA (**Figure 5-figure supplement 1A-B**). However, ScRev7 did not inhibit Sae2's nuclease activity, even at the highest concentration tested (**Figure 5-figure supplement 1C and D**). Together, these results support the idea that inhibition of Mre11 endonuclease activity is due to its direct interaction with ScRev7.

### **ScRev7 impedes Rad50's ATPase activity without affecting its ATP binding ability**

Several studies have demonstrated that the ATPase activity of Rad50 plays an important regulatory role in DNA recombination and repair (**Cejka and Symington, 2021**). Given that ScRev7 specifically associated with Rad50, we asked whether such association affects the ability of Rad50 to bind ATP and catalyze its hydrolysis. To test this possibility, different concentrations of purified Rad50 were incubated with a fixed amount [ $\gamma$ -<sup>32</sup>P]ATP, and then the reaction mixtures were UV irradiated prior to subjecting the samples to SDS/PAGE. The results showed a single band that migrated as a 153 kDa species corresponding to the position of ScRad50 (**Figure 6A**). Quantitative analyses indicated that Rad50 binds [ $\gamma$ -<sup>32</sup>P]ATP in a manner dependent on its concentration (**Figure 6C**). The results from an accompanying experiment revealed comparable levels of [ $\gamma$ -<sup>32</sup>P]ATP binding by Rad50 in the presence or absence of ScRev7 (**Figure 6B and 6D**), suggesting that it does not impair the ATP-binding ability of Rad50.

We next explored the potential effect of ScRev7 on ATP hydrolysis catalyzed by Rad50 using thin layer chromatography. Consistent with previous studies (**Ghosal and Muniyappa, 2007**), Rad50 catalyzed [ $\gamma$ -<sup>32</sup>P]ATP hydrolysis to ADP and <sup>32</sup>Pi in a manner dependent on its concentration in the absence of ScRev7 (**Figure 6E and 6F**). Interestingly, while ScRev7 itself has no ATPase activity, its addition led to inhibition of ATP hydrolysis catalyzed by Rad50 in a dose-dependent manner (**Figure 6G and 6J**). The results of a parallel experiment indicated that Rev7 does not affect the ATPase activity of a meiosis-specific *S. cerevisiae* Dmc1, indicating its inhibitory specificity towards Rad50 (**Figures 6H and 6J**). Similar analysis showed that ScRev7-C1 inhibited the ATP hydrolysis of Rad50 but three-fold less efficiently than its full-length counterpart (**Figures 6I and 6J**). These results were validated using a colorimetric molybdate/malachite green-based assay (**Lanzetta et al., 1979**). While ScRev7 inhibited the ATPase activity of Rad50 to an extent of 60% at the highest concentration tested, Rev7-C1 was about three-fold less inhibitory than its full-length counterpart at an identical concentration (**Figure 6—figure supplement 1**). Collectively, our results support a model in which ScRev7 negatively regulates the catalytic activities of Mre11 and Rad50 subunits.

### ***REV7 facilitates NHEJ in *S. cerevisiae****

In *S. cerevisiae*, the heterotrimeric MRX complex has been implicated in both Ku-dependent NHEJ and microhomology-mediated end joining repair (**Moore and Haber, 1996; Boulton and Jackson, 1998; Ma et al., 2003; Zhang and Paull, 2005**). Multiple studies in cancers have shown that Rev7 inhibits DNA end-resection and favors NHEJ over HR (**Gupta et al., 2018; Ghezraoui et al., 2018; Dev et al., 2018; Gao et al., 2018; Liang et al., 2020**). To our knowledge, it is unknown whether these findings are relevant to other species. However, we note that *Schizosaccharomyces pombe* Rev7 has been shown to inhibit long-range resection at DSBs (**Leland et al., 2018**). Furthermore, it is unclear whether the *S. cerevisiae* Rev1, Rev3 and Rev7 subunits are required for NHEJ. To investigate this, the efficiency of plasmid-based NHEJ repair was analyzed by transforming BamHI-linearized plasmid pRS416, which has no homology with the genomic DNA, into the WT and isogenic mutant strains as previously described (**Boulton and Jackson, 1998; Moreau et al., 1999**) (**Figure 7A**). Consistent with a prior study (**Boulton and Jackson, 1998**), we found that NHEJ was

undetectable in the *mre11Δ* mutant (**Figure 7B, Supplementary Table S3**). Notably, while the *rev1Δ* and *rev3Δ* strains showed a modest decrease in the efficiency of NHEJ, *rev7Δ* single and *rev1Δ rev3Δ* double mutants exhibited about four- and twofold decrease, respectively, compared with the WT. Further analysis revealed that the NHEJ efficiency in double mutants - *rev1Δ rev7Δ*, *rev3Δ rev7Δ* and *sae2Δ rev7Δ* - was comparable to that of *rev7Δ* mutant (**Figure 7B and 7C –Supplementary Table S3**). Intriguingly, however, we found that ScRev7-42 aa peptide, but not the Rev7-C1 variant, fully restored the NHEJ efficiency in *rev7Δ* cells to the WT levels. It remained possible that the significant reduction in NHEJ efficiency observed in the *rev7Δ* cells could be due to aberrant cell cycle progression. To test this possibility, cell cycle progression in both WT and *rev7Δ* cells was monitored using a fluorescence-activated cell sorter. Compared with the wild-type (WT) cells, we observed a slightly delayed cell cycle progression with *rev7Δ* cells at 30 and 45 min after release from G1 arrest, and there were no differences in their mating type phenotypes. However, after 45 minutes, *rev7Δ* cells exhibited a similar distribution of cells in the G1, S, and G2 phases of the cell cycle as observed in WT cells (**Figure 7—figure supplement 1**). Together, these results indicate that *rev7Δ* cells do not possess aberrant cell cycle or mating type defects as compared with the WT cells.

We next sought to determine whether ScRev7 plays a role in NHEJ pathway at the chromosome level. To address this question, the efficiency of NHEJ was evaluated using a “suicide-deletion” assay in which the I-SceI induced DSB can be repaired via NHEJ (**Karathanasis and Wilson, 2002**). Briefly, it is based on an approach wherein galactose-induced I-SceI endonuclease inflicts a pair of site-specific DSBs, resulting in the deletion of its own coding region, thereby facilitating the repair of DSB via NHEJ (**Figure 8A**). Using this approach, we determined the frequency of Ade2+ recombinants in the WT and isogenic mutant strains. A critical NHEJ factor Ku70 was used as a control. As expected, while NHEJ was undetectable in strains lacking *MRE11* and *KU70*, deletion of *REV7*, *REV1* and *REV3* led to a 9-fold, 2.3-fold- and 3.2-fold decrease, respectively, in the frequency of NHEJ compared with the WT strain. Of note, a fourteen-fold decrease in the frequency of Ade2+ recombinants was observed in the *rev7-C1* cells, which could be restored to WT levels by expressing the C-terminal 42 amino acid peptide (**Figure 8B, Supplementary Table S4**). These results reinforce the notion that Rev7 promotes NHEJ repair at DSBs. The PCR

product derived from genomic DNA of Ade2+ recombinants showed a 1.3 kb amplicon, suggesting faithful repair of I-SceI induced DSB (**Figure 8C**).

### ***REV7 plays an anti-recombinogenic role during HR in S. cerevisiae***

As mentioned above, current evidence suggests that the RIF1/REV7/Shieldin complex blocks DNA end resection and BRCA1-mediated HR, but promotes DSB repair through NHEJ in cancer cells (**Gómez-Llorente et al., 2013; Du Xu et al., 2015; Boersma et al., 2015; Mirman et al., 2018; Findlay et al., 2018; Gupta et al., 2018; Ghezraoui et al., 2018; Dev et al., 2018; Tomida et al., 2018; Gao et al., 2018; Noordermeer et al., 2018; Liang et al., 2020; Malik et al., 2020; Truong et al., 2021**). A flurry of research on Shieldin complex in human cancer cells from other laboratories soon followed (Clairmont and D'Andrea, 2021). However, the generality of these findings has remained elusive. Therefore, we leveraged a spot assay (**Paeschke et al., 2013**) to understand whether *REV7* plays a role in the regulation of HR in *S. cerevisiae*. In this assay, under conditions of optimal growth and replication stress, we measured the frequency of HR between the *ura3-1* allele on chromosome V and *ura3-G4* allele (*ura3* interrupted by G4 motifs) on the pFAT10-G4 plasmid (**Figure 9A**). In the absence of HU, while no Ura3+ papillae were observed in the *ura3-1* strain carrying the empty vector (**Figure 9B, top row**), all other strains harboring the plasmid pFAT10-G4 formed Ura3+ papillae (**Figure 9B**).

We sought to build on these observations by testing the effect of HU on the formation of Ura3+ papillae by the strains (carrying pFAT10-G4 plasmid) used in the experiment. This analysis revealed that the *ura3-1 rev7Δ* double mutant strain formed significantly more Ura3+ papillae than *ura3-1* strains, but less than what was seen in the absence of HU. As anticipated, we observed that both *mre11-D56N,H125N* (used as an internal control) and *rev7Δ mre11-D56N,H125N* mutant strains did not form Ura3+ papillae (**Figure 9B**). A similar analysis showed that *ura3-1* strain and the same strain expressing ScRev7-42 amino acid peptide, but not Rev7-C1 variant, displayed a very few, and small Ura3+ papillae. As expected, Ura3+ papillae formation was not observed in the *ura3-1* strain carrying the empty vector. Quantification indicated that the *ura3-1 rev7Δ* mutant showed 11.5-fold increase in the formation of Ura3+ papillae as compared with *ura3-1* strain (**Figure 9C**). Thus, we envision that the absence of Ura3+ papillae in the *ura3-1* strain (with or without empty vector) in the presence of

HU might be related to Rev7-mediated suppression; whereas their absence in cells that lack functional Mre11 nuclease is due to HU-induced toxicity. Such an effect has been described previously in the Mre11 nuclease-deficient cells (**Tittel-Elmer et al., 2009; Hamilton and Maizels, 2010**). Regardless, these results support a model in which *REV7* gene product plays an anti-recombinogenic role during HR, thus its deletion unleashes the cells to facilitate HR between *ura3G4* and *ura3-1* mutant alleles located on the plasmid and chromosome V, respectively.

To confirm whether the G-quadruplex motifs stimulate HR in the *rev7Δ* strain, the frequency of HR was measured using pFAT10-G4-mut plasmid, which harbors mutations within G-tracts of the *ura3G4* allele. The results revealed that the frequency of HR reduced by about 5.8-fold, as compared to the strain carrying plasmid pFAT10-G4 with unmutated sequences, revealing that reduction in HR may be caused by mutations in the G-quadruplex forming sequences (**Figure 9—figure supplement 1**). To assess whether increased frequency of HR is due to the instability of G-quadruplex DNA in *rev7Δ* cells, the length of G4 DNA inserts was assessed in the plasmids isolated from WT and *rev7Δ* cells. The results showed a DNA fragment of 829 bp corresponding to the expected size in both WT and *rev7Δ* cells (**Figure 9—figure supplement 2**), raising the possibility that increased frequency of HR in *rev7Δ* cells could be due to the loss of Rev7 function and instability of G-quadruplex forming sequences.

Finally, a qPCR-based assay (**Mimitou and Symington, 2010; Ferrari et al., 2018**) was employed to quantify the amounts of ssDNA generated in the *rev7Δ* and *rad51Δ mre11-H125N rev7Δ* strains at a HO endonuclease-induced DSB (Figure 9—figure supplement 3A). The results indicated a significant increase in the percentage of ssDNA 0.7 kb distal to the DSB at 4 h after its induction in the *rev7Δ rad51Δ* cells compared with *rad51Δ* cells (**Figure 9—figure supplement 3B**). As expected, the DNA end resection rates in the *mre11-H125N* and *mre11-H125N rev7Δ* cells were similar to that in the *rad51Δ* cells. Importantly, at 3 kb distal to the DSB, *rev7Δ* cells showed comparable rates of DNA end resection, in line with both *rad51Δ* and *mre11-H125N* cells (**Figure 9—figure supplement 3C**). Altogether, these results support the

notion that Rev7 suppresses HR by inhibiting Mre11-mediated short-range DNA end resection.

## DISCUSSION

In this study, we reveal the surprising finding that Rev7 physically associates with the subunits of the MRX complex and also provide unanticipated insights into the mechanism by which it regulates the DSB repair pathway choice between HR and NHEJ in *S. cerevisiae*. Notably, we demonstrate that Rev7 binds to the subunits of the MRX complex, via a 42-residue C-terminal segment (residues 203-245), protects cells from G4 DNA-HU-induced toxicity, facilitates DSB repair via NHEJ while blocking HR. In addition, we present robust evidence that ScRev7 impedes Mre11 nuclease and Rad50's ATPase activities, without affecting the latter's ability to bind ATP. When seen from a teleological perspective, our work is conceptually reminiscent of Shieldin complex-mediated suppression of 5' end resection and repair of DSBs via NHEJ by blocking HR in human cancer cells. It remains plausible that this alternative mechanism of DSB repair pathway choice in *S. cerevisiae* might be conserved across multiple species.

Historically, *REV7* was discovered as playing an important role in DNA damage-induced mutagenesis in *S. cerevisiae* (Lemontt, 1971; Lawrence *et al.*, 1985a). Further investigations showed that Rev7 associates with Rev3 and functions as a regulatory subunit of eukaryotic TLS DNA polymerase Pol $\zeta$  (Prakash *et al.*, 2005; Maiorano *et al.*, 2021; Ling *et al.*, 2022; Paniagua and Jacobs, 2023). While Rev7 has no known enzymatic activity, it acts as a versatile scaffolding protein with pleiotropic functions in diverse cellular processes including, but not limited to, epigenetics, immune signalling, viral mutagenesis and cancer development that were initially considered inconceivable (Decottignies, 2013; de Krijger *et al.*, 2021). However, little is known about the nature of specific effector(s) that associate with Rev7 and regulate DSB repair pathway choice in *S. cerevisiae*. As we discuss below, our work convincingly demonstrates that ScRev7 physically interacts with the individual subunits of MRX complex and regulates their activities. In line with this, MST based protein-protein interaction assays, supported by AF2-multimer modelling, imply tight association between the Mre11 and Rad50 subunits and ScRev7. It is interesting

to note that Sae2, which cooperates with the MRX complex to initiate DNA end resection, does not associate with Rev7, suggesting interaction specificity between MRX subunits and Rev7.

However, an intriguing inquiry arises regarding whether the MRX subunits exist as separate entities in the cell. Although, to our knowledge, the existence and relative amounts of monomeric, dimeric and trimeric species of MRX subunits *in vivo* are unknown, current evidence suggests that both Mre11 and Rad50 subunits independently bind DNA (**Stracker and Petrini, 2011; Paull, 2018; Casari et al., 2019**). Other studies have shown that MRX complex binds and tethers DNA ends, which is thought to be required for DSB repair (**Trujillo et al., 2003; Cassani et al., 2015**). Furthermore, while data obtained from co-immunoprecipitation experiments implicate that Mre11, Rad50 and Xrs2 subunits exist as a hetero-trimeric complex *in vivo* (**Usui et al., 1998**), *in vitro* experiments have shown the formation of dimeric Mre11-Rad50 and trimeric MRX complexes (**Oh et al., 2016; Arora et al., 2017**). Collectively, these results allow us to postulate that the monomeric, dimeric and trimeric species of MRX subunits might exist in a dynamic equilibrium under *in vivo* conditions.

Given that Rev7 and MRX complex play essential roles in DNA repair pathways, our findings provide novel insights into how ScRev7 interacts with the MRX subunits and regulates their functions. Structure-function analysis showed that deletion of 42-amino acid residues (203-245) at the extreme C-terminus of ScRev7 abolished its ability to interact with the MRX subunits, whereas loss of the N-terminal HORMA domain, an evolutionarily conserved protein-protein interaction module (**Muniyappa et al., 2014; Rosenberg and Corbett, 2015; de Krijger et al., 2021;**) had no discernible effect on their interactions. Curiously, further analysis indicated that the 42-aminoacid peptide alone was sufficient to bind to the subunits of MRX complex and regulate the DSB repair pathway choice between NHEJ and HR. Reciprocally, future work will be required to determine the regions/domains of MRX subunits that interact with ScRev7 for a comprehensive understanding of the crosstalk between these components. Work is currently in progress to gather insights into these questions.

The data from MST-based protein-protein interaction assays informed that ScRev7 binds to the MRX subunits with sub-micromolar affinity, analogous to the interaction between HORMA-domain protein hMAD2 and hCDC20 (**Piano et al., 2021**). How might ScRev7 attenuate the function of Mre11 and Rad50 subunits? Our finding indicate that nanomolar amounts of ScRev7 besides attenuating the Mre11 nuclease activity also impedes Rad50's ATPase activity without obstructing the ability of the latter to bind ATP. Whilst the specific nuances of the interaction await further research, we surmise that physical interaction between ScRev7 and the Mre11/Rad50 subunits might contribute to the observed effects. Although we provide compelling Y2H data that the C-terminal 42-aminoacid peptide of Rev7 is critical for binding to the MRX subunits and protect cells from G4 DNA-HU-induced toxicity, and regulate the pathway choice between NHEJ and HR; however, we could not demonstrate its function *in vitro* because of technical difficulties associated with its expression and purification. By comparison, we found that the Rev7-C1 variant, which lacks the ability to interact with the MRX subunits in Y2H assays, was capable of blocking, albeit partially, the catalytic activities of Mre11 and Rad50 subunits *in vitro*. A likely possibility is that amino acid residues in the Rev7-C1 fragment might be involved in pairwise interactions between ScRev7 and the Mre11 and Rad50 subunits, as seen in AlphaFold2 models. Conversely, the 42-amino acid fragment as a part of whole protein might act as a lid to block the residues in the Rev7-C1 fragment, thereby enabling it to function effectively as a single site for binding to the MRX subunits in Y2H assays. Future studies are required to test this hypothesis.

Many lines of evidence indicate that G-quadruplex forming sequences are measurably enriched at certain functional regions in the genomes of all organisms, from humans to plants to microbes (**Huppert and Balasubramanian, 2005; Capra et al., 2010; Castillo Bosch et al., 2014; Lejault et al., 2021**). Furthermore, G-quadruplex structures modulate diverse cellular processes, including DNA replication, transcription, translation, and are associated with certain diseases, characterized by high rates of chromosomal instability (**Rhodes and Lipps, 2015; Spiegel et al., 2020**). Interestingly, we found that *rev7Δ* mutant cells harbouring exogenous G-quadruplex forming sequences exhibit hypersensitivity to HU-induced genotoxic stress and cell death. This is consistent with emerging evidence that DNA replication stress

induced by G-quadruplex structures play a prominent role in triggering genomic instability, which is exacerbated in the presence of HU (**Sato and Knipscheer, 2023**). Although the precise mechanism remains unclear, it is tempting to speculate that Rev7 may recruit G4-resolving helicase(s) such as Sgs1 and Pif1 to unwind G-quadruplex structures prior to or during DNA replication (**Huber et al., 2002, Paeschke et al., 2013**). Alternatively, or in addition, it might generate G4 DNA intermediates which may be processed or cleaved by specific enzymes, including Mus81, Sgs1 or Mre11 (**Regairaz et al., 2011; Sun et al., 1999; Ghosal and Muniyappa, 2005; 2007**). Regardless, our data align with the notion that G-quadruplex structures are endogenous sources of replication stress and their formation and persistence may lead to genomic instability and cell death.

As mentioned above, Shieldin complex facilitates NHEJ-dependent DSB repair, while inhibiting DNA end resection and HR in cancer cells (**Clairmont and D'Andrea, 2021; Paniagua and Jacobs, 2023**). Since 5' end resection is the primary step in HR-mediated DSB repair, we hypothesized that physical interaction between ScRev7 and MRX subunits might block resection of DNA termini, and then facilitate NHEJ-dependent DSB repair instead of HR. Consistent with this premise, we found that ScRev7 promotes NHEJ by blocking HR. However, other regulatory components may also play a role in modulating the levels of NHEJ versus HR-mediated DSB repair. For instance, TRIP13 or p31<sup>comet</sup> inhibits the interaction of Rev7 with the SHLD3 subunit and regulates DNA end resection at DSBs and promotes their repair by HR (**Sarangi et al., 2020**). Additionally, interaction between Rev7 and putative binding partners may be regulated by posttranslational modifications and chromatin accessibility under changing physiological conditions.

Although the mechanism underlying Rev7-mediated regulation of DSB repair between *S. cerevisiae* and human cancer cells indicate broad similarities, we also observed some notable differences. A fundamental difference between the results from cancer cells and *S. cerevisiae* is that, while ScRev7 robustly interacts with and suppresses the biochemical activities of both Mre11 and Rad50 subunits to facilitate NHEJ, Rev7-Shieldin complex acts as a downstream effector of 53BP1-RIF1 in restraining DNA end resection to promote NHEJ (**Clairmont and D'Andrea, 2021**;

Paniagua and Jacobs, 2023). Furthermore, hRev7 interacts with the SHLD3 subunit via the HORMA domain, which is entirely dispensable in the case of ScRev7. Thus, we posit that the Shieldin complex-mediated regulation of DSB repair pathway choice might be a source of evolutionary innovation as an additional layer of regulation. In summary, our data provide novel insights into the alternative mechanism underlying the regulation of DSB repair pathway choice in *S. cerevisiae*.

## MATERIALS AND METHODS

### ***S. cerevisiae* strains, DNA plasmids and oligonucleotides**

All strains and primers used for the construction of DNA substrates in this study are listed in **Supplementary Table S5 and S6**, respectively. The plasmids FT10/Chr.IV<sub>G4</sub>\_Ig and FT10/Chr.IV<sub>G4</sub>\_le were a kind gift from Dr. Virginia Zakian.

### **Construction of strains used in the study**

The *S. cerevisiae* W1588a haploid strains carrying single/double deletions in the genes *rev1Δ*, *rev3Δ*, *rev7Δ*, *rev1Δ rev3Δ*, *rev7Δ mre11Δ* or *sae2Δ rev7Δ* were constructed using appropriate pairs of primers as previously described (**Sambrook and Russell, 2001; Janke et al., 2004**). The *REV7* gene was deleted using the KanMX4 (pFA6a- KanMX4) cassette utilizing the forward primer OSB11 and reverse primer OSB12, and deletion was confirmed by PCR using gene-specific primers OSB13 and OSB14. Similarly, other strains were generated as follows: *MRE11* was deleted using the hphNT1 cassette (pYM-hphNT1) utilizing the OSB52 and OSB54 primers; deletion was verified by PCR using primer OSB53. The *REV1* was deleted in a similar fashion, using the hphNT1 cassette and the OSB55 and OSB56 primers; deletion was ascertained by PCR using primer OSB57. *REV3* gene was deleted using the KanMX4 cassette (derived from pFA6a-hphNT1, pFA6a-KanMX4 respectively) and the primers OSB58 and OSB59; deletion was confirmed by PCR using primer OSB60. The hphNT1 (pYM-hphNT1) cassette was used in the generation of double mutants (listed in **Supplementary Table S6**). The *rev7-C1* and *rev7-42* mutant strains were constructed by inserting sequences encoding N- and C-terminally truncated forms of Rev7 at the endogenous loci using *rev7-C1-9MYC-hphNT1* and *rev7-42-*

3MYC-KANMX4 cassettes via overlapping primer-based PCR. The *rev7-C1-9MYC-hphNT1* cassette was generated using primer pairs OSB116, OSB117 and OSB118, OSB70. Likewise, *rev7-42-3MYC-KANMX4* cassette was generated using primer pairs OSB122, OSB120 and OSB121, OSB70. The N- and C-terminal truncation variants were confirmed by PCR using probes OSB13 and OSB14, respectively.

The *mre11Δ*, *rev1Δ*, *rev3Δ* and *rev7Δ* mutant strains were generated in the strain YW714 using the hphNT1 cassette (derived from pFA6a-hphNT1). The *REV7* truncation variants with the c-myc tag sequence - *rev7-C1-9MYC* and *rev7-42 aa-3MYC* - were generated as described above. The *REV3* gene was deleted using the hphNT1 cassette in the strain PJ694A utilizing primers OSB58 and OSB59 and deletion was confirmed using primer OSB60. Likewise, *mre11Δ rad50Δ xrs2Δ* triple mutant was generated in the strain PJ694A as follows: *mre11Δ::KANMX4* was generated by PCR-amplification of KANMX4 cassette (pFA6a-KANMX4) using forward and reverse primers, OSB52 and OSB53, respectively. Gene deletion was confirmed by PCR using primer OSB54. The *rad50Δ::URA3* strain was constructed by PCR amplification of URA3 cassette (pAG60-URA3) using primers OSB133 and OSB75; deletion was confirmed using primer OSB76. Similarly, *xrs2Δ::HphNT1* was generated by PCR amplification of hphNT1 cassette (pFA6a-hphNT1) using primers OSB134 and OSB78, and deletion was confirmed using primer OSB79. The *rev7Δ* mutants were generated in the strain LSY2172-24C and LSY2265-10D, as described above.

### **Construction of DNA plasmids for expression and recombination assays**

The plasmids FT10/Chr.IV<sub>G4</sub>\_Ig and FT10/Chr.IV<sub>G4</sub>\_le were a kind gift from Dr. Virginia Zakian. *S. cerevisiae* *REV7* gene was amplified from genomic DNA by PCR using primer pair (forward OSB01 and reverse OSB02) and Phusion DNA polymerase (NEB, Ipswich, MA) as previously described (**Sambrook and Russell, 2001**). The reaction yielded an amplicon of expected size, which was digested with BamHI/HindIII, and ligated into a BamHI/HindIII digested pET28a(+) vector (Novagen) using T4 DNA ligase. The resulting expression plasmid was designated pET-28a\_REV7. Analogously, the truncated plasmid pET28a\_ScREV7-C1 was generated by PCR amplification using primers OSB01 and OSB125 and pET28a\_ScREV7 plasmid DNA as a template. The PCR product was digested with BamHI/HindIII and ligated into

BamHI/HindIII digested pET28a vector. Likewise, *S. cerevisiae RAD50* gene was PCR-amplified from genomic DNA using OSB33 (forward) and OSB34 (reverse) primers. The amplicon was digested with BamHI/Xho1 and ligated into a BamHI/Xho1 digested pE-SUMO Kan vector (Life Sensors, Malvern, PA) using T4 DNA ligase. The resulting expression plasmid was designated pE-SUMO\_RAD50. The *REV7-eGFP* expression vector was constructed by PCR amplification of *S. cerevisiae REV7* gene in the pET-28a\_REV7 plasmid using forward Rev7-eGFP primer and reverse Rev7-eGFP primer (**Supplementary Table S6**). The amplicon of expected size was digested with XbaI/Xhol and ligated into XbaI/Xhol digested pPROEX vector, upstream of eGFP coding sequence. The resulting plasmid encodes ScRev7-eGFP fusion protein. Similarly, the DNA sequence encoding ScRev7-C1 was amplified from pET28a-REV7 plasmid using primers as shown in Table S6. The amplicon was then cloned into pPROEX::eGFP vector. The pPROEX::eGFP vector was a kind gift from Deepak Saini.

The *ura3-G4* insert was amplified by overlap extension PCR method using OSB80 and OSB82 as forward and OSB81 and OSB83 as reverse primers, respectively. The amplicon was digested with BamHI/SphI and ligated into a BamHI/SphI digested FAT10 vector. The primer OSB82 corresponds to the DNA sequence 362751-362775 of the coding strand of *S. cerevisiae* Chr X. The primer OSB81 is its complementary strand. Similarly, *ura3-G4* mutant was generated using OSB80 and OSB130 as forward, and OSB129 and OSB83 as reverse primers. The PCR product corresponding to full-length *ura3-G4* mutant was digested with BamHI/SphI and cloned into FAT10 vector. The ODN OSB129 sequence 362751-362775 corresponds to mutant version of *S. cerevisiae* Chr X. The OSB130 is its complementary strand.

### **Construction of DNA plasmids for yeast two-hybrid analysis**

To construct the pGBKT7-*REV7*, the *S. cerevisiae REV7* orf in the pET28a (+) *REV7* construct was PCR-amplified using Phusion DNA polymerase and forward OSB03 and reverse OSB04 primers, respectively. The amplicon was digested with Nde1/BamHI and ligated into Nde1/BamHI digested pGBKT7 vector. The *S. cerevisiae MRE11* gene was PCR-amplified from the genomic DNA using OSB05 forward primer and *MRE11\_RP* reverse primer. The amplicon was digested with BamHI/EcoRI and ligated

into the pGADT7 prey expression vector at the BamHI/EcoRI site. The same procedure was leveraged for the construction of all other prey expression vectors: XRS2 was amplified from the genomic DNA using forward OSB36 and reverse OSB37 primers. The amplicon was digested with Nde1/BamHI and ligated into the pGADT7 prey expression vector at the Nde1/BamHI site; *RAD50* was amplified from the pESUMO\_*RAD50* construct using forward OSB35 and reverse OSB34 primers. The amplicon was digested with EcoRI/Xho1 and ligated into the pGADT7 prey expression vector digested with EcoRI and Xho1; *REV7* was amplified from the pET-28a\_*REV7* construct using the same primers and ligated into pGADT7 prey expression vector as in the case of bait plasmid construction. The *SAE2* gene was amplified from the plasmid pET21a-SAE2 (**Ghodke and Muniyappa, 2013**) using primers OSD150 and OSD151 and the amplicon was digested with NdeI and EcoRI and cloned into pGADT7 vector.

The N-terminally truncated ScREV7 variants (REV7- N1, REV7- N2, and REV7-N3) were constructed by PCR amplification of relevant portions of the *REV7* gene using OSB61, OSB62, OSB63 as a forward primers and OSB4 as a reverse primer (common for all N- terminal deletions), respectively. The C-terminally truncated ScREV7 variants (REV7-C1, REV7- C2 and REV7-C3) were constructed via PCR amplification of relevant portions of the *REV7* gene in the pET-28a\_*REV7* plasmid using OSB3 as a forward primer (common for all C-terminal deletions), and OSB64, OSB65 and OSB66 as reverse primers, respectively. The amplicons, corresponding to the N- and C-terminal variants, were digested with Nde1/BamHI and ligated into Nde1/BamHI digested pGBKT7 vector. *S. cerevisiae* PJ694A strain was used in Y2H analyses.

### Cell viability assay

The *S. cerevisiae* WT and isogenic mutant strains were grown in liquid YPD or SC medium to an OD<sub>600</sub> of 0.5. Ten-fold serial dilutions were spotted on YPD agar plates with or without HU. Similarly, cells were spotted on SC selection medium plates lacking the indicated amino acids, with or without inhibitors, as indicated in the figure legends. The plates were incubated at 30 °C for 3-4 days. The images were captured using epi-illumination at auto-exposure ChemiDoc MP imaging system (Bio-Rad).

## Yeast two-hybrid interaction analysis

The Y2H assays were performed as previously described (**Fields and Song, 1989; Thakur et al., 2020**). Briefly, pairwise combination of plasmids expressing bait proteins, fused to the Gal4 DNA-binding domain (G4BD), and prey proteins, fused to the Gal4 activation domain (G4AD), were co-transformed into the WT strain PJ69-4A, *rev3Δ* single *mre11Δ* *rad50Δ* *xrs2Δ* triple mutant strain. The empty prey vector and a vector expressing Rev7 served as negative and positive controls, respectively. The interactions were analysed by spotting the indicated transformants on SC-/Trp -Leu and SC-/Trp -Leu -His agar plates containing 15 mM 3-aminotrizole (3-AT), which were then incubated for 3-5 days at 30°C. Growth of cells on SC-Leu-Trp-His +3-AT agar plates is indicative of moderate/strong protein-protein interactions between the bait and prey proteins.

## Assay for G-quadruplex DNA-HU-induced toxicity

The assay was performed as previously described (**Paeschke et al., 2011**). The plasmid constructs used in this study were identical to the parent plasmid, pFAT10, except that its derivatives contained three tandem arrays of G sequences derived from chromosome IV, inserted in the lagging or leading templates. Briefly, the *S. cerevisiae* WT, *rev7Δ* mutant, and cells expressing ScRev7 truncation variants (ScRev7-C1, ScRev7-42 aa) harboring the pFAT10 plasmid were synchronized in the G1 phase using α-factor at 30 °C and then released from the pheromone block by washing the cells. Subsequently, the cultures were diluted to yield identical A<sub>600</sub> values. Tenfold serial dilutions of each culture was spotted on SC-/Leu or SC-/Leu/+100 mM HU agar plates, which were incubated at 30 °C for 72 h.

## Expression and purification of ScRev7

The *S. cerevisiae* Mre11, Rad50, Xrs2, and Sae2 proteins were expressed and purified as previously described (**Ghosal and Muniyappa, 2007; Ghodke and Muniyappa, 2016**). The *S. cerevisiae* REV7 gene was sub-cloned into pET28a(+) expression vector with an N-terminal His<sub>6</sub>-tag. The resulting plasmid was designated pET28a(+)\_REV7. The *E. coli* BL21(DE3)pLysS cells harboring pET28a(+)\_REV7 plasmid were grown at 37 °C in Luria-Bertani broth (1% tryptone, 0.5% yeast extract,

1% NaCl, pH 7.0) containing 50 µg/ml kanamycin in an orbital shaking incubator at 180 rpm to an OD<sub>600</sub> of 0.6, and then ScRev7 expression was induced by adding 1-thio-β-D-galactopyranoside (IPTG) to a final concentration of 0.1 mM. Following the addition of IPTG, cultures were grown in an orbital shaking incubator at 25 °C for 12 h. Cells were harvested by centrifugation at 6000 g and the cell paste was resuspended in 50 ml of buffer A (20 mM Tris-HCl (pH 8.0), 150 mM NaCl, 10% glycerol and 5 mM 2-mercaptoethanol containing 1 mM phenylmethylsulfonyl fluoride and 0.05% Triton X-100). The cells were lysed by sonication on ice (7 x 1-min pulses) and subjected to centrifugation at 30000 rpm at 4 °C for 20 min. Solid ammonium sulfate was added (0.472 gm/ml) to the supernatant with continuous stirring for 45 min at 24 °C. The precipitate was collected by centrifugation at 18000 rpm at 4 °C for 1 h. The precipitate was dissolved in buffer A and dialyzed against the same buffer. The dialysate was loaded onto a 5 ml Ni<sup>2+</sup>-NTA column (Qiagen, Valencia, CA). After washing the column with buffer A containing 20 mM imidazole, bound proteins were eluted with a gradient of 20→500 mM imidazole. The fractions containing ScRev7 were pooled and dialyzed against buffer B (20 mM Tris-HCl, pH 8.0, 1.2 M NaCl, 7% glycerol, 5 mM 2-mercaptoethanol). ScRev7 protein was further purified by chromatography using a Superdex S75 gel filtration column, attached to an AKTA Prime FPLC system, which had been equilibrated with and eluted using buffer B. The peak fractions containing Rev7 were pooled and dialyzed against buffer C (20 mM Tris-HCl (pH 8.0), 30 mM NaCl, 30% glycerol, 5 mM 2-mercaptoethanol), and loaded onto a heparin column (5 ml). The bound proteins were eluted with a gradient of 30→350 mM NaCl in buffer C. Aliquots of each fraction were analyzed by SDS-PAGE and the protein bands were visualized by staining the gel with Coomassie brilliant blue. The fractions that contained Rev7 were pooled and dialyzed against buffer D (20 mM Tris-HCl (pH 8.0), 100 mM NaCl, 10% glycerol, 1 mM DTT), and stored at -80 °C.

### **Expression and purification of ScRev7-eGFP and ScRev7C1-eGFP**

The His<sub>6</sub>-tagged ScRev7-eGFP and ScRev7C1-eGFP fusion proteins were expressed in and purified from whole cell lysates of *E. coli* BL21(DE3)pLysS host strain harboring the pPROEX/REV7-eGFP plasmid as described above. The His<sub>6</sub>-tagged eGFP was purified from the cell lysates of *E. coli* BL21\* (DE3) pLysS host strain harboring eGFP pPROEX expression plasmid by Ni<sup>2+</sup>-NTA affinity chromatography. Briefly, the whole

cell lysate was loaded onto a 5 ml Ni<sup>2+</sup>-NTA resin column, which had been equilibrated with a buffer A (HEPES, pH 7.5, 50 mM NaCl and 10% glycerol). The column was washed with buffer A containing 70 mM imidazole. The bound proteins were eluted with a gradient of 70 → 800 mM imidazole in buffer A. Aliquots of each fraction were analyzed by SDS-PAGE and the protein bands were visualized by staining the gel with Coomassie brilliant blue. The protein concentrations were determined by the Bradford assay. The fractions that contained ScRev7-eGFP and eGFP were pooled, dialyzed against buffer A, and stored at -80 °C.

### **Expression and purification of *S. cerevisiae* Rev1**

The GST-tagged Rev1 was purified as described previously with some modifications (**Johnson et al., 2006**). Briefly, the *S. cerevisiae* BJ5464 cells carrying plasmid pBJ842-Rev1-GST were selected on SC plates lacking leucine. Single colonies were inoculated into liquid SC/-Leu medium (200 ml) containing 2% raffinose, and the cultures were grown for 12-14 h at 30°C until the A<sub>600</sub> nm reached 0.5. Following this, the cultures were centrifuged at 14000 rpm for 10 min and the pellet was washed thrice with MilliQ water. Cells were then resuspended in liquid SC/-Leu medium containing 2% galactose. The cultures were grown at 30 °C in an orbital shaking incubator at 250 rpm for 7 h, harvested by centrifugation at 4000 rpm for 10 min, resuspended in CBB buffer (50 mM Tris-HCl pH 7.5, 10% sucrose, 1 mM EDTA, 10 mM β-mercaptoethanol and 5 µg/mL of protease inhibitor cocktail). Cells were lysed using a FastPrep 24 homogenizer and the cell debris was separated by centrifugation at 10000 rpm for 10 min. The supernatant was centrifuged at 35000 rpm for 30 min. The protein(s) in the supernatant was precipitated using ammonium sulfate (0.208 g/ml), followed by centrifugation at 20000 rpm for 45 min. The pellet was resuspended in the GST-binding buffer (GBB, 50 mM Tris-HCl pH 7.5, 10% glycerol, 1 mM EDTA, 10 mM β-mercaptoethanol and 5 µg/mL of protease inhibitor cocktail) and dialyzed extensively against the same buffer. The sample was loaded onto a GST-column (GSTrap High performance column, 5 ml, Cytiva Life Sciences) at a rate of 0.5 mL/min. The column was washed with GBB buffer containing 500 mM NaCl. Bound protein was eluted using GBB buffer containing 40 mM glutathione. Fractions (1 mL each) were collected at a flow rate of 1 mL/min, analyzed on 10% SDS-PAGE and staining the gel with Coomassie brilliant blue. The fractions containing pure Rev1-GST protein were pooled

and dialyzed against MST buffer (HEPES, pH 7.5, 50 mM NaCl, 10% glycerol) and stored at -80°C. The concentration of ScRev1 was determined by the dye-binding assay.

### SDS-PAGE and immunoblot analysis

Western blot analysis was performed as previously described (**Mahmood and Yang, 2012**). The *S. cerevisiae* PJ69-4A strains were co-transformed with empty vectors pGBK7 and pGADT7, or a bait vector harboring Rev7 truncations in combination with prey vectors harboring *REV7*, *MRE11*, *XRS2* or *RAD50*. The transformants were selected by plating on SC/-Leu,-Trp agar medium, and single colonies were inoculated into liquid SC/-Trp,-Leu medium (5 ml) containing 2% dextrose. The cultures were incubated at 30°C for 12-14h in a rotary incubator at a speed of 200 rpm to  $A_{600\text{nm}} = 0.15$ , which were then transferred onto 10 ml of liquid SC/-Trp,-Leu medium. Incubation was continued at 30°C with shaking to until the culture reached  $A_{600\text{nm}} = 0.5$ . The cells were harvested by centrifugation at 4000 rpm for 5 min and the pellet was resuspended in lysis buffer (50 mM sodium-HEPES pH 7.5, 200 mM sodium acetate pH 7.5, 1 mM EDTA, 1 mM EGTA, 5 mM magnesium acetate and 5% glycerol). Cells were lysed with 2 min bursts at 4.0 m/s on a FastPrep-24 homogenizer in the presence of 200 ml of acid-washed glass beads. The samples were centrifuged at 7000 rpm for 5 min to remove the beads and cell debris. The supernatant was centrifuged at 13000 rpm for 10 min. Equal amounts of protein (50 µg protein from the supernatants) were separated by 10% SDS-PAGE. The proteins from the gel were transferred onto a polyvinyl difluoride (PVDF) membrane (0.45 µm). The blot was blocked with 5% nonfat dry milk in TBST (20 mM Tris-HCl buffer, pH 7.5, 150 mM NaCl, 0.1% Tween 20) buffer for 1 h at 25°C, washed, and probed at 25 °C for 1 h with anti-Myc antibodies (dilution 1:3000 dilution). Subsequently, the blots were washed thrice with TBST buffer and incubated with HRP-conjugated anti-rabbit antibodies (dilution 1:20000; Sigma-Aldrich) at 25°C for 1 h. Finally, the blots were washed thrice with TBST buffer and developed using chemiluminescence substrates (Bio-Rad Laboratories, CA, USA) in the Bio-Rad ChemiDoc Imaging systems. Anti-PGK1 antibodies were obtained from Santa-Cruz Biotechnologies, CA, USA.

## AlphaFold-Multimer predictions of Mre11-Rev7 and Rad50-Rev7 protein complexes

The sequences of full-length ScRev7, Mre11 and Rad50 were obtained from the *Saccharomyces* Genome Database (<https://www.yeastgenome.org/>). The ScRev7-Mre11 and ScRev7-Rad50 heterodimer models were built using AF2-multimer (**Evans et al., 2022; Varadi et al., 2022**) via the ColabFold software (<https://github.com/sokrypton/ColabFold>) (**Mirdita et al., 2022**). The models with the highest confidence were analysed using LigPPlot software (Version 2.2) to identify the amino acid residues involved in the interactions between the Mre11/Rad50 subunits and ScRev7. Approximately, 44% and 43% of the residues across the binding interface of ScRev7 and Mre11 displayed confident pLDDT scores greater than 60. Similarly, 67% and 100% of the residues lining the ScRev7 and Rad50 interface exhibited pLDDT scores greater than 60. The PyMOL Molecular Graphics System (Version 2.5.5) was used to visualize and analyze protein structures. Among the five different types of models generated by AlphaFold-Multimer, the top models (based on average pLDDT score) were chosen for display.

## Microscale thermophoresis assay

The microscale thermophoresis (MST) assays were carried out on a Monolith NT.115 instrument (NanoTemper Technologies GmbH) according to the manufacturer's instructions. Samples were prepared in 20 µl MST buffer (HEPES, pH 7.5, 50 mM NaCl, 10% glycerol) containing ScRev7-eGFP or eGFP and different concentrations of ligands in the range: Mre11 (0.00015 to 5 µM), Rad50 (0.00006 to 2 µM), Xrs2 (0.00015 to 5 µM), Mre11-Rad50 (0.00015 to 5 µM), Rev1 (0.00015 to 5 µM) or Sae2 (0.00015 to 5 µM). After incubation at 37 °C for 15 min, samples were transferred into Monolith NT.115 glass capillaries. The measurements were performed using 40% MST power with laser on/off times of 30 s and 5 s, and the MST signals were normalised to fraction bound (X) by  $X = [Y(c) - \text{Min}] / (\text{Max} - \text{Min})$ , error bars (SD) were normalized by  $\text{stdnorm} = \text{std}(c) / (\text{Max} - \text{Min})$ . The Fnorm values or fraction bound were plotted against the ligand concentration to obtain an estimate of binding affinity. The values of the Hill coefficient and equilibrium dissociation constants ( $K_d$ ) were calculated using the isothermal binding equation model in the MO. Affinity Analysis software provided by NanoTemper. Statistical analysis of data was performed using GraphPad Prism software (v5.0).

## Preparation of radiolabeled DNA substrates

The sequences of oligonucleotides (ODNs) used for the preparation of DNA substrates are listed in **supplementary Table S7**. The ODNs were labeled at the 5' end using [ $\gamma$ -<sup>32</sup>P]ATP and T4 polynucleotide kinase, as previously described (**Sambrook and Russell, 2001**). The unincorporated [ $\gamma$ -<sup>32</sup>P]ATP was removed using a Sephadex G-50 superfine mini-column. The dsDNA substrates were prepared as follows: 41 bp dsDNA by mixing aliquots of 5'-end <sup>32</sup>P-labeled OSB17 (upper strand) with a small excess of unlabeled complementary OSB20; 60 bp dsDNA by mixing OSB41 (upper strand) and OSB42 (lower strand) in 1X SSC buffer (0.3 M sodium citrate buffer, pH 7.0, containing 3 M NaCl), followed by heating at 95 °C for 5 min and then slowly cooling to 24 °C over a period of 90 min. The substrates were resolved by non-denaturing 8% PAGE for 4 h at 4 °C (**Thakur et al., 2016**). The substrates were eluted from the gel slices in TE buffer (10 mM Tris-HCl, pH 7.5, and 1 mM EDTA) and stored at 4 °C for further use.

## Exonuclease assay

The assay was performed as previously described (**Arora et al., 2017**) with slight modifications. Two steps are involved in the assay: the first step involves the assembly of the ScRev7-MRX complex, and the second, DNA cleavage. The MRX subunits (100 nM each) were mixed with increasing concentrations of ScRev7 (0.05 to 2.5  $\mu$ M) or ScRev7-C1 (1.5 and 3  $\mu$ M) and incubated on ice for 15 min, prior to the addition of twenty  $\mu$ l of reaction mixture that contained 25 mM MOPS (pH 7.0), 20 mM Tris-HCl (pH 7.5), 80 mM NaCl, 8% glycerol, 5 mM MnCl<sub>2</sub>, 5 mM MgCl<sub>2</sub>, 1 mM ATP, 1 mM DTT, 200  $\mu$ g/ml BSA and 10 nM of <sup>32</sup>P-labeled 60 bp dsDNA. Subsequently, reaction mixtures were incubated at 37 °C for 1 h, and the reaction stopped by adding a two  $\mu$ l solution containing two mg/ml proteinase K, 50 mM EDTA and 1% SDS. After incubation at 37 °C for 30 min, five  $\mu$ l of a solution containing 10  $\mu$ g/ml glycogen, two  $\mu$ l 3 M sodium acetate and 50  $\mu$ l of absolute ethanol was added to each sample and were frozen at -80°C. The thawed samples were centrifuged at 15000 rpm at 4 °C for 30 min. The pellets were washed with 70% ethanol and centrifuged at 15000 rpm at 4 °C for 5 min. The dried pellets were resuspended in 10  $\mu$ l gel-loading dye (80% formamide, 10 mM EDTA, 0.1% xylene cyanol and 0.1%

bromophenol blue) and incubated at 95 °C for 5 min. Aliquots were analyzed on a 8% denaturing polyacrylamide/7 M urea PAGE using TBE buffer (89 mM Tris-borate (pH 8.3) and 1 mM EDTA) for 2 h at 40 W. The gels were dried, exposed to a phosphorimager screen, and scanned using a Fuji FLA 9000 phosphor imager.

### Endonuclease assay

The assay was carried out as previously described (**Shibata et al., 2014**) with slight modifications. Briefly, the reaction mixtures (10 µl) without ScRev7 contained 100 ng of M13 circular ssDNA, 30 mM Tris-HCl, pH 7.5, 25 mM KCl, 5% glycerol, 1 mM DTT, 200 µg/ml BSA, 5 mM MnCl<sub>2</sub> and increasing concentrations of ScMre11 (0.1-2 µM). After incubation at 37 °C for 1 h, the reaction was stopped by adding 2 µl of stop solution (2 mg/ml proteinase K, 50 mM EDTA and 1% SDS) and incubation was extended for 30 min, followed by the addition of 2 µl of gel loading solution. The reaction products were separated by electrophoresis on a 0.8% native agarose gel using 44.5 mM Tris-borate buffer (pH 8.3) containing 0.5 mM EDTA at 10 V/ cm for 1 h. The gel was stained with ethidium bromide and the image was captured using the UVItec gel documentation system (UVItec, Cambridge, UK). To test the effect of ScRev7 on Mre11 endonuclease activity, the assay was carried out as described above, except that the ScRev7-Mre11 heterodimer was first formed by incubating a fixed amount of ScRev7 with increasing concentration of ScRev7 on ice for 15 min, prior to the addition of 10 µl of reaction buffer. The reaction mixtures were incubated and analyzed as described above.

### ATP crosslinking assay

The assay was carried out as previously described (**Thakur et al., 2021b**). The reaction mixture (20 µl) contained 50 mM Tris-HCl (pH 5.0), 10 mM MgCl<sub>2</sub>, 400 pmol [ $\gamma$ -<sup>32</sup>P]ATP and increasing concentrations of Rad50 (0.1-1 µM). Analogously, a fixed concentration of Rad50 (0.2 µM) was incubated with increasing concentrations of ScRev7 (0.5 - 6 µM) at 4 °C for 15 min, prior to transferring the sample into 20 µl buffer containing 50 mM Tris-HCl (pH 5.0), 10 mM MgCl<sub>2</sub> and 400 pmol [ $\gamma$ -<sup>32</sup>P]ATP. After incubation at 4 °C for 25 min, samples were exposed to UV irradiation (1.2 × 10<sup>5</sup> µJ/cm<sup>2</sup> in Hoefer UVC 500 ultraviolet crosslinker) at a distance of 2 cm. The reactions were stopped by adding 5 µl of 5X Laemmli buffer (10 mM Tris-HCl, pH 6.8, 12.5%

SDS, 40% glycerol, and 0.1% bromophenol blue). Samples were incubated at 95 °C for 10 min and resolved by SDS/PAGE in 10% polyacrylamide gel at 35 mA for 2 h. The gels were dried, exposed to a phosphorimager screens, and scanned using a Fuji FLA-9000 phosphor imager and the band intensities of radiolabeled species was quantified using UVI-Band Map software (v. 97.04). Data was plotted as mean and SD in GraphPad Prism (v5.0).

### ATPase assay

The hydrolysis of [ $\gamma$ -<sup>32</sup>P]ATP by Rad50 was assessed by measuring the release of <sup>32</sup>P<sub>i</sub> as previously described (**Thakur et al., 2021a**). A fixed concentration of Rad50 (0.5  $\mu$ M) was incubated on ice for 30 min with increasing concentrations of ScRev7 or ScRev7-C1 to allow protein complex formation, prior to the reaction. Analogously, 200  $\mu$ M [ $\gamma$ -<sup>32</sup>P] ATP and Rad50 (0.5  $\mu$ M) were incubated in 10  $\mu$ l reaction mixture containing 20 mM Tris HCl (pH 7.5), 50 mM KCl, 0.2 mg/ ml BSA, 0.1 mM DTT, 1.0 mM MgCl<sub>2</sub> and 5 % glycerol, with indicated concentrations of Rad50. The reaction mixtures incubated at 30 °C for 30 min and the reaction was stopped by adding 15 mM EDTA. Aliquots (2  $\mu$ l) from each sample were spotted onto a polyethyleneimine-cellulose plate, developed in a solution containing 0.5 M LiCl, 1 M formic acid and 1 mM EDTA. The reaction products were visualized by using a Fuji FLA-9000 phosphor imager, and the band intensities were quantified and plotted using UVI-Band map software. Data was plotted as mean and SD using GraphPad Prism (Version 5.0).

### Malachite green phosphate assay

ATP hydrolysis was monitored by measuring the amount of inorganic phosphate released using acidic ammonium molybdate and malachite green assay (**Lanzetta et al., 1979**). The reaction mixtures (80  $\mu$ l) contained 20 mM Tris-HCl (pH 7.5), 50 mM KCl, 5% glycerol, 0.1 mM DTT, 0.2 mg/ml BSA, 1 mM MgCl<sub>2</sub>, 150  $\mu$ M ATP, and increasing concentrations of ScRad50 (0.05 - 1  $\mu$ M). After incubation at 30°C for 30 min, reaction was stopped by adding 20  $\mu$ l of malachite green reagent (Sigma-Aldrich, MAK307). Incubation was continued for 15 min at 24 °C to allow the formation of phosphomolybdate malachite green chromogenic complex. The absorbance values, as a measure of the extent of ATP hydrolysis, at 620 nm (y-axis) were plotted against increasing concentrations of ScRad50 (x-axis). To test the effect of ScRev7 or

ScRev7-C1 on Rad50 ATPase activity, increasing concentrations of ScRev7 or ScRev7-C1 (0.1 - 2 µM) were incubated with 0.25 µM of ScRad50 on ice for 20 min, prior to mixing it with the reaction mixture. After incubation at 30 °C for 30 min, ATP hydrolysis was monitored as described above. The data were plotted, and the best-fit line was determined by nonlinear regression incorporating using GraphPad Prism (v. 5.0).

### **Mass spectrometry analysis**

Mass spectrometry analysis of Rev7-GFP was carried out to ascertain its identity using orbitrap mass spectrometry (**Zubarev and Makarov, 2013**). In-gel trypsin digestion was performed as follows: 50 mM ammonium bicarbonate and acetonitrile in 7:3 ratio was used for de-staining; following which, samples were reduced for 30 min by adding 10 mM DTT diluted in 50 mM ammonium bicarbonate. Following reduction, alkylation buffer (55 mM iodoacetamide in 50 mM ammonium bicarbonate) was added and samples were incubated at room temperature for 30 min. Samples were treated with 10 ng trypsin (Mass spectrometry-grade, Sigma Aldrich, India), at 37°C for 12 h. The peptides were eluted with 70% acetonitrile (300 µL) containing 0.1% trifluoracetic acid, and the samples were dried in speed vacuum and the pellet was resuspended in 40 µL resuspension buffer (2% acetonitrile in LC-MS grade Milli-Q). Samples (10 µL) were injected into the Orbitrap Fusion tribrid mass spectrometer (Thermo Fisher Scientific Inc., USA). Samples were run for 110 min using a nano-spray ionization (NSI) source and static spray voltage. Ions were detected by Orbitrap detector at 60000 resolution using quadrupole isolation. Daughter ions were detected by Ion Trap detector using quadrupole isolation mode. Following data acquisition, peptide spectrum matches (PSMs) and percentage peptide coverage were obtained for the samples. Collectively, these results confirmed that the purified protein is GFP-tagged ScRev7.

### **Non-homologous end-joining assay**

The assay was performed using a linear plasmid as previously described (**Zhang and Paull, 2005; Ghodke and Muniyappa, 2013**). Briefly, 60 ng of BamHI-digested or undigested plasmid pRS416 was transformed into the WT and isogenic *rev1Δ*, *rev3Δ*, *rev7Δ*, *mre11Δ*, *sae2Δ*, *rev1Δrev3Δ*, *rev1Δrev7Δ*, *rev3Δrev7Δ*, *mre11Δrev7Δ*, *sae2Δrev7Δ* *rev7-C1* or *rev7-42* strains. The uncut plasmid pRS416 served as a

control. The transformants arising from plasmid re-circularization were selected on SC-/Ura agar plates after incubation at 30 °C for 3-5 days. The efficiency of transformation was calculated as a ratio of the number of transformants with digested plasmid DNA to that with undigested plasmid DNA. The graph was obtained using GraphPad Prism (Version 5.0) and statistical significance was calculated using one-way ANOVA Dunnett's multiple comparisons test.

### Cell cycle analysis

Cell cycle analysis was performed using a fluorescence-activated cell sorter (FACS) as previously described (**Ghodke and Muniyappa, 2016**). Cells were cultured to A<sub>600</sub> of 0.5 and synchronized in the G1 phase by treatment with α-factor (100 ng/ml, Sigma Aldrich) for 2 h at 30°C. The cells were washed three times with 1X PBS and resuspended in fresh liquid YPD medium. Aliquots were collected after release from G1 arrest at 15, 30, 45, 60, 75, 90, 105, and 120 min. The cells were fixed in 70% ethanol and stored at 4°C. Subsequently, samples were treated with RNase A (0.4 mg/mL) at 37°C for 12 h, stained with propidium iodide (15 µg/mL) and incubated at 37°C for an additional 3 h. FACS analysis was performed on a FACSVerse analyzer (BD Biosciences). Dead and aggregated cells were excluded through gating, and cell cycle distribution was analyzed using FlowJo software (Version 10).

### Non-homologous end-joining using a “suicide deletion” reporter assay

The assay was performed as previously described (**Karathanasis and Wilson, 2002**). Briefly, *S. cerevisiae* YW714 strains WT, *rev1Δ*, *rev3Δ*, *rev7Δ*, *mre11Δ*, *ku70Δ*, *rev7-C1* and *rev7-42* cells were grown in an orbital shaking incubator at 200 rpm in a liquid SC-/Ura medium overnight at 30 °C. The cells were pelleted by centrifugation at 4000 rpm for 10 min. Cell pellets were washed thrice with MilliQ water and resuspended in liquid SC medium at an OD<sub>600</sub> of 1. Serial dilutions were plated on SC-/Ura agar plates containing glucose, and SC-/Ade agar plates containing galactose. After 5 days of incubation at 30 °C, the number of colonies was counted. The rate of NHEJ, as a function of Ade<sup>+</sup> colonies, was calculated using the FALCOR software (**Hall et al., 2009**). The differences between experimental results and relevant controls were tested with Dunnett's multiple comparison test. The graph was generated using GraphPad Prism (Version 5.0). Statistical tests and p-values are mentioned in each figure legend.

## Plasmid-chromosome recombination assay

The assay was performed as previously described (**Paeschke et al., 2013**). The WT and isogenic *ura3-1*, *ura3-1 rev7Δ*, *ura3-1 mre11-D56N,H125N ura3-1 rev7Δ mre11-D56N,H125N*, *ura3-1 rev7-C1* and *ura3-1 rev7-42* strains were transformed with 60 ng of empty vector (pFAT10) or a plasmid bearing G4 DNA forming sequences (pFAT10-G4). The synchronous cells were grown in liquid SC/-Leu medium to an OD<sub>600</sub> of 0.5. Equal numbers of cells were replica-spotted on SC/-Ura medium and SC/-Ura medium plates containing 0.1 M HU. After incubation for 4-6 days at 30 °C, the number of papillae was counted. The recombination frequency was calculated using FLCOR software (**Hall et al., 2009**).

## Quantitative PCR analysis

The rate of DNA end resection was determined in *rad51Δ*, *rad51Δ rev7Δ*, *rad51Δ mre11-H125N* and *rad51Δ mre11-H125N rev7Δ* strains, as previously described (**Mimitou and Symington, 2010; Ferrari et al., 2018**). Single colonies grown in liquid YPD medium at 30°C for 12 h were sub-cultured in liquid YP medium containing 2% raffinose at 30°C till A<sub>600</sub> reached 0.5. At this stage, cells were synchronized at G2/M phase by adding nocodazole (10 µg/mL) and HO expression was induced by adding 2% galactose to the cell culture. For each time point, 20 mL samples were collected for each strain and 0.1% sodium azide was added immediately. Cells were collected by centrifugation at 4000 rpm for 10 min. The bead-beating step was used for isolation of genomic DNA from the resuspended pellets (**Amberg et al., 2005**). Samples were incubated with 10 units of Styl-HF and XbaI-HF (New England Biolabs, Ipswich, USA) in a reaction mixture containing 15 µg of genomic DNA, 1X CutSmart buffer at 37 °C for 7 h. In parallel, equal amounts of gDNA was mock-digested as control. DNA was precipitated by adding equal volumes of isopropanol, followed by centrifugation at 13000 rpm for 20 min. Pellets were washed with 1 mL of 70% ethanol, air dried, and resuspended in 50 µL of 1X Tris-EDTA buffer (pH 7.5). In qPCR analysis, equal amounts of DNA (1 ng) was used per reaction in a mixture containing 1X SYBR green master mix (G-Biosciences, St. Louis, MO) and 0.2 µM each of forward and reverse

primers, as indicated in the Table S8. The qPCR reaction was performed using a Bio-Rad CFX96 thermocycler and 96-well PCR plates. The data obtained from the qPCR were analysed using the Bio-Rad CFX Maestro 1.1 software (version 2.3). The specificity of the qPCR was ascertained by (a) agarose gel electrophoresis and (b) melting curve analysis of qPCR products. Similarly, primer efficiencies were calculated by performing qPCR analysis using serially diluted DNA samples. The HO cut efficiencies across strains were estimated by qPCR analysis at a single HO site (Coordinates 284324-294420) with a unique upstream sequence on Chromosome III. Upon DSB induction, the percentage of ssDNA generated by end resection at different time points and distance (0.7 kb and 3 kb) from the break was calculated as previously described (**Ferrari et al., 2018**). The *PRE1* gene situated on chromosome V was used as an internal reference. Two-way ANOVA was performed to statistically analyse the datasets and graphs were generated using GraphPad Prism (Version 5.0).

### Statistical and data analysis

Differences among groups were analyzed by one-way ANOVA Dunnett's multiple comparison test followed by Tukey's post hoc test (GraphPad Prism 6.07). Statistical significance level was set as follows: \*, P-value < 0.05; \*\*, P-value < 0.01; \*\*\*, P-value < 0.001; \*\*\*\*, P-value < 0.0001. The statistical methods employed to analyse the data are indicated in the figures legends.

### Acknowledgements

We thank Drs. Virginia Zakian, Maria Pia Longhese, Lorraine Symington and Thomas Wilson for kindly providing some of the strains used in this study, as well as to Dr. Narottam Acharya for the generous gift of ScRev7 and ScRev1 expression plasmids, *S. cerevisiae* BJ5464 strain, and for his assistance in the purification of expressed proteins, and Naren Chandran Shakthivel for his assistance with the generation of AlphaFold-multimer models.

### Funding

This work was supported by a grant (CRG/2021/000082) from the Science and Engineering Research Board, New Delhi to K. M., who was also the recipient of Bhatnagar Fellowship (SP/CSIR/425/2018) from the council of Scientific and

Industrial Research, New Delhi.

### Author contributions

Sugith Badugu, Kshitiza M. Dhyani, Manoj Thakur: Investigation, Methodology, Software, Validation, Data curation, Writing – original draft and editing; Kshitiza M. Dhyani Manoj Thakur, Kalappa Muniyappa, Conceptualization, Resources, Supervision, Funding acquisition, Formal analysis, Project administration, Writing – review and editing.

### Conflict of interest statement

None declared

## REFERENCES

- Acharya N**, Johnson RE, Prakash S, Prakash L. 2006. Complex formation with Rev1 enhances the proficiency of *Saccharomyces cerevisiae* DNA polymerase zeta for mismatch extension and for extension opposite from DNA lesions. *Molecular and Cellular Biology* **26**: 9555–9563.
- Amberg DC**, Burke DJ, Strathern JN. 2005. Methods in Yeast Genetics: A Cold Spring Harbor Laboratory Course Manual.
- Arora S**, Deshpande RA, Budd M, Campbell J, Revere A, Zhang X, Schmidt KH, Paull TT. 2017. Genetic separation of Sae2 nuclease activity from Mre11 nuclease functions in budding yeast. *Molecular and Cellular Biology* **37**: e00156-17.
- Baranovskiy AG**, Lada AG, Siebler HM, Zhang Y, Pavlov YI, Tahirov TH. 2012. DNA polymerase delta and zeta switch by sharing accessory subunits of DNA polymerase delta. *The Journal of Biological Chemistry* **287**: 17281–17287.
- Bezalel-Buch R**, Cheun YK, Roy U, Schärer OD, Burgers PM. 2020. Bypass of DNA interstrand crosslinks by a Rev1-DNA polymerase  $\zeta$  complex. *Nucleic Acids Research* **48**: 8461–8473.
- Bluteau D**, Masliah-Planchon J, Clairmont C, Rousseau A, Ceccaldi R, Dubois d'Enghien C, Bluteau O, Cuccuini W, Gachet S, Peffault de Latour R, et al. 2016. Biallelic inactivation of REV7 is associated with Fanconi anemia. *The Journal of Clinical Investigation* **126**: 3580–3584.
- Boersma V**, Moatti N, Segura-Bayona S, Peuscher MH, van der Torre J, Wevers BA, Orthwein A, Durocher D, Jacobs JL. 2015. MAD2L2 controls DNA repair at telomeres and DNA breaks by inhibiting 5' end resection. *Nature* **521**: 537–540.
- Boulton SJ**, Jackson SP. 1998. Components of the Ku-dependent non-homologous end-joining pathway are involved in telomeric length maintenance and telomeric silencing. *The EMBO Journal* **17**: 1819–1828.
- Capra JA**, Paeschke K, Singh M, Zakian VA. 2010. G-quadruplex DNA sequences are evolutionarily conserved and associated with distinct genomic features in *Saccharomyces cerevisiae*. *PLoS Computational Biology* **6**: e1000861.
- Casari E**, Rinaldi C, Marsella A, Gnugnoli M, Colombo CV, Bonetti D, Longhese MP. 2019. Processing of DNA double-strand breaks by the MRX complex in a chromatin context. *Frontiers in Molecular Biosciences* **6**: 43.
- Cassani C**, Gobbini E, Wang W, Niu H, Clerici M, Sung P, Longhese MP. 2015. Tel1 and Rif2 regulate MRX functions in end-tethering and repair of DNA double-strand breaks. *PLoS Biol.* **14**: e1002387.

- Castillo Bosch P**, Segura-Bayona S, Koole W, van Heteren JT, Dewar JM, Tijsterman M, Knipscheer P. 2014. FANCJ promotes DNA synthesis through G-quadruplex structures. *The EMBO Journal* **33**: 2521–2533.
- Cejka P**, Symington LS. 2021. DNA End resection: mechanism and control. *The Annual Review of Genetics* **55**: 285–307.
- Clairmont CS**, D'Andrea AD. 2021. REV7 directs DNA repair pathway choice. *Trends in Cell Biology* **31**: 965–978.
- Clairmont CS**, Sarangi P, Ponnienselvan K, Galli LD, Csete I, Moreau L, Adelman G, Chowdhury D, Marto JA, D'Andrea AD. 2020. TRIP13 regulates DNA repair pathway choice through REV7 conformational change. *Nature Cell Biology* **22**: 87–96.
- Dai Y**, Zhang F, Wang L, Shan S, Gong Z, Zhou Z. 2020. Structural basis for shieldin complex subunit 3-mediated recruitment of the checkpoint protein REV7 during DNA double-strand break repair. *The Journal of Biological Chemistry* **295**: 250–262.
- De Krijger I**, Boersma V, Jacobs JJL. 2021. REV7: Jack of many trades. *Trends in Cell Biology* **31**: 686–701.
- Decottignies A**. 2013. Alternative end-joining mechanisms: a historical perspective. *Frontiers in genetics* **4**: 48.
- Dev H**, Chiang TW, Lescale C, de Krijger I, Martin AG, Pilger D, Coates J, Sczaniecka-Clift M, Wei W, Ostermaier M, et al. 2018. Shieldin complex promotes DNA end-joining and counters homologous recombination in BRCA1-null cells. *Nature Cell Biology* **20**: 954–965.
- Du Truong C**, Craig TA, Cui G, Botuyan MV, Serkasevich RA, Chan KY, Mer G, Chiu PL, Kumar R. 2021. Cryo-EM reveals conformational flexibility in apo DNA polymerase  $\zeta$ . *The Journal of Biological Chemistry* **297**, 100912.
- Evans R**, O'Neill M, Pritzel A, Antropova N, Senior A, Green T, et al. 2022. Protein complex prediction with AlphaFold-Multimer. *bioRxiv*. <https://doi.org/10.1101/2021.10.04.463034> 24.
- Ferrari M**, Twayana S, Marini F, Pellicoli A. 2018. A qPCR-based protocol to quantify DSB resection. *Methods in Molecular Biology* **1672**, 119–129. doi: 10.1007/978-1-4939-7306-4\_10. PMID: 29043621.
- Fields S**, Song O. 1989. A novel genetic system to detect protein-protein interactions. *Nature* **340**: 245–246.
- Findlay S**, Heath J, Luo VM, Malina A, Morin T, Coulombe Y, Djerir B, Li Z, Samiei A, Simo-Cheyrou E, et al. 2018. SHLD2/FAM35A co-operates with REV7 to coordinate DNA double-strand break repair pathway choice. *The EMBO Journal* **37**: e100158.
- Gao S**, Feng S, Ning S, Liu J, Zhao H, Xu Y, Shang J, Li K, Li Q, Guo R, et al. 2018. An OB-fold complex controls the repair pathways for DNA double-strand breaks. *Nature Communications* **9**: 3925.
- Ghezraoui H**, Oliveira C, Becker JR, Bilham K, Moralli D, Anzilotti C, Fischer R, Deobagkar-Lele M, Sanchez-Calvo M, Fueyo-Marcos E, et al. 2018. 53BP1 cooperation with the REV7-shieldin complex underpins DNA structure-specific NHEJ. *Nature* **560**: 122–127.
- Ghodke I**, Muniyappa K. 2013. Processing of DNA double-stranded breaks and intermediates of recombination and repair by *Saccharomyces cerevisiae* Mre11 and its stimulation by Rad50, Xrs2, and Sae2 proteins. *The Journal of Biological Chemistry* **288**: 11273–11286.
- Ghodke I**, Muniyappa K. 2016. Genetic and biochemical evidences reveal novel insights into the mechanism underlying *Saccharomyces cerevisiae* Sae2-mediated abrogation of DNA replication stress. *Journal of biosciences* **41**: 615–641.
- Ghosal G**, Muniyappa K. 2005. *Saccharomyces cerevisiae* Mre11 is a high-affinity G4 DNA-binding protein and a G-rich DNA-specific endonuclease: implications for replication of telomeric DNA. *Nucleic Acids Research* **33**: 4692–4703.
- Ghosal G**, Muniyappa K. 2007. The Characterization of *Saccharomyces cerevisiae*

- Mre11/Rad50/Xrs2 complex reveals that Rad50 negatively regulates Mre11 endonucleolytic but not the exonucleolytic activity. *The Journal of Molecular Biology* **372**: 864–882.
- Gómez-Llorente Y**, Malik R, Jain R, Choudhury JR, Johnson RE, Prakash L, Prakash S, Ubarretxena-Belandia I, Aggarwal AK. 2013. The architecture of yeast DNA polymerase  $\zeta$ . *Cell Reports* **5**: 79–86.
- Guo C**, Fischhaber PL, Luk-Paszyc MJ, Masuda Y, Zhou J, Kamiya K, Kisker C, Friedberg EC. 2003. Mouse Rev1 protein interacts with multiple DNA polymerases involved in translesion DNA synthesis. *The EMBO Journal* **22**: 6621–6630.
- Gupta R**, Somyajit K, Narita T, Maskey E, Stanlie A, Kremer M, Typas D, Lammers M, Mailand N, Nussenzweig A, et al. 2018. DNA repair network analysis reveals shieldin as a key regulator of NHEJ and PARP inhibitor sensitivity. *Cell* **173**: 972–988.
- Hall BM**, Ma C-X, Liang P, Singh KK. 2009. Fluctuation analysis CalculatOR: a web tool for the determination of mutation rate using Luria-Delbrück fluctuation analysis. *Bioinformatics* **25**: 1564–1565.
- Hamilton NK**, Maizels N. 2010. MRE11 function in response to topoisomerase poisons is independent of its function in double-strand break repair in *Saccharomyces cerevisiae*. *PLoS One* **5**: e15387.
- Haracska L**, Unk I, Johnson RE, Johansson E, Burgers PM, Prakash S, Prakash L. 2001. Roles of yeast DNA polymerases delta and zeta and of Rev1 in the bypass of abasic sites. *Genes & Development* **15**: 945–954.
- Hoff B**, Kamerewerd J, Sigl C, Mitterbauer R, Zadra I, Kürnsteiner H, Kück U. 2010. Two components of a velvet-like complex control hyphal morphogenesis, conidiophore development, and penicillin biosynthesis in *Penicillium chrysogenum*. *Eukaryotic Cell*. **9**:1236-50.
- Huang ME**, Rio AG, Galibert MD, Galibert F. 2002. Pol32, a subunit of *Saccharomyces cerevisiae* DNA polymerase delta, suppresses genomic deletions and is involved in the mutagenic bypass pathway. *Genetics* **160**: 1409–1422.
- Huber MD**, Lee DC, Maizels N. 2002. G4 DNA unwinding by BLM and Sgs1p: substrate specificity and substrate-specific inhibition. *Nucleic Acids Research* **30**: 3954-3961.
- Huppert JL**, Balasubramanian S. 2005. Prevalence of quadruplexes in the human genome. *Nucleic Acids Research* **33**: 2908-2916.
- James P**, Halladay J, Craig EA. 1996. Genomic libraries and a host strain designed for highly efficient two-hybrid selection in yeast. *Genetics* **144**: 1425–1436.
- Janke C**, Magiera MM, Rathfelder N, Taxis C, Reber S, Maekawa H, Moreno- Borchart A, Doenges G, Schwob E, Schieber E, Knop M. 2004. A versatile toolbox for PCR-based tagging of yeast genes: new fluorescent proteins, more markers and promoter substitution cassettes. *Yeast* **21**: 947–962.
- Johnson RE**, Prakash L, Prakash S. 2006. Yeast and human translesion DNA synthesis polymerases: expression, purification, and biochemical characterization. *Methods in Enzymology* **408**: 390-407.
- Johnson RE**, Prakash L, Prakash S. 2012. Pol31 and Pol32 subunits of yeast DNA polymerase delta are also essential subunits of DNA polymerase zeta. *Proceedings of the National Academy of Sciences USA* **109**: 12455–12460.
- Karathanasis E**, Wilson WT. 2002. Enhancement of *Saccharomyces cerevisiae* end-joining efficiency by cell growth stage but not by impairment of recombination. *Genetics* **161**: 1015–1027.
- Kikuchi S**, Hara K, Shimizu T, Sato M, Hashimoto H. 2012. Structural basis of recruitment of DNA polymerase  $\zeta$  by interaction between REV1 and REV7 proteins. *The Journal of Biological Chemistry* **287**: 33847-33852.
- Kochenova OV**, Bezalel-Buch R, Tran P, Makarova AV, Chabes A, Burgers PM, Shcherbakova PV. 2017. Yeast DNA polymerase  $\zeta$  maintains consistent activity and

- mutagenicity across a wide range of physiological dNTP concentrations. *Nucleic Acids Research* **45**: 1200–1218.
- Koegl M**, Uetz P. 2007. Improving yeast two-hybrid screening systems. *Briefings in functional genomics and proteomics*. **6**: 302-312.
- Lange SS**, Takata K, Wood RD. 2011. DNA polymerases and cancer. *Nature Reviews Cancer* **11**: 96-110.
- Lanzetta PA**, Alvarez LJ, Reinach PS, Candia OA. 1979. An improved assay for nanomole amounts of inorganic phosphate. *Analytical Biochemistry* **100**: 95–97.
- Lawrence CW**, Das G, Christensen RB. 1985a. REV7, a new gene concerned with UV mutagenesis in yeast. *Molecular & General Genetics* **200**: 80–85.
- Lawrence CW**, Nisson PE, Christensen RB. 1985b. UV and chemical mutagenesis in rev7 mutants of yeast. *Molecular & General Genetics* **200**, 86–91.
- Lejault P**, Mitteaux J, Sperti FR, Monchaud D. 2021. How to untie G-quadruplex knots and why? *Cell Chemical Biology* **28**:436-455.
- Leland BA**, Chen AC, Zhao AY, Wharton RC, King MC. 2018. Rev7 and 53BP1/Crb2 prevent RecQ helicase-dependent hyper-resection of DNA double-strand breaks. *Elife* **7**: e33402.
- Lemontt JF**. 1971. Mutants of yeast defective in mutation induced by ultraviolet light. *Genetics* **68**: 21–33.
- Lengsfeld BM**, Rattray AJ, Bhaskara V, Ghirlando R, Paull TT. 2007. Sae2 is an endonuclease that processes hairpin DNA cooperatively with the Mre11/Rad50/Xrs2 complex. *Mol. Cell* **28**: 638-651.
- Liang L**, Feng J, Zuo P, Yang J, Lu Y, Yin Y. 2020. Molecular basis for assembly of the shieldin complex and its implications for NHEJ. *Nature Communications* **11**: 1972.
- Ling JA**, Frevert Z, Washington MT. 2022. Recent advances in understanding the structures of translesion synthesis DNA polymerases. *Genes (Basel)* **13**: 915.
- Listovsky T**, Sale JE. 2013. Sequestration of CDH1 by MAD2L2 prevents premature APC/C activation prior to anaphase onset. *The Journal of Cell Biology* **203**: 87–100.
- Lobachev KS**, Gordenin DA, Resnick MA. 2002. The Mre11 complex is required for repair of hairpin-capped double-strand breaks and prevention of chromosome rearrangements. *Cell* **108**, 183-193.
- Ma JL**, Kim EM, Haber JE, Lee SE. 2003. Yeast Mre11 and Rad1 proteins define a Ku-independent mechanism to repair double-strand breaks lacking overlapping end sequences. *Molecular and Cellular Biology* **23**, 8820–8828.
- Mahmood T**, Yang PC. 2012. Western Blot: Technique, theory, and trouble shooting. *North American journal of medical sciences* **4**: 429–434.
- Maiorano D**, El Etr J, Franchet C, Hoffmann JS. 2021. Translesion synthesis or repair by specialized DNA polymerases limits excessive genomic instability upon replication stress. *The International Journal of Molecular Sciences* **22**: 3924.
- Makarova AV**, Burgers PM. 2015. Eukaryotic DNA polymerase  $\zeta$ . *DNA Repair* **29**: 47–55.
- Makarova AV**, Stodola JL, Burgers PM. 2012. A four-subunit DNA polymerase zeta complex containing Pol delta accessory subunits is essential for PCNA-mediated mutagenesis. *Nucleic Acids Research* **40**: 11618–11626.
- Malik R**, Johnson RE, Prakash L, Prakash S, Ubarretxena-Belandia I, Aggarwal AK. 2022. Cryo-EM structure of translesion DNA synthesis polymerase  $\zeta$  with a base pair mismatch. *Nature Communications* **13**: 1050.
- Malik R**, Kopylov M, Gomez-Llorente Y, Jain R, Johnson RE, Prakash L, Prakash S, Ubarretxena-Belandi I, Aggarwal AK. 2020. Structure and mechanism of B-family DNAPolymerase  $\zeta$  specialized for translesion DNA synthesis. *Nature Structural & Molecular Biology* **27**: 913–924.
- Mimitou EP**, Symington LS. 2010. Ku prevents Exo1 and Sgs1-dependent resection of DNA ends in the absence of a functional MRX complex or Sae2. *The EMBO journal* **29**, 3358–3369. <https://doi.org/10.1038/emboj.2010.193>

- Mirdita M**, Schutze K, Moriwaki Y, Heo L, Ovchinnikov S, Steinegger M. 2022. ColabFold: making protein folding accessible to all. *Nature Methods* **19**:679–682.
- Mirman Z**, Lottersberger F, Takai H, Kibe T, Gong Y, Takai K, Bianchi A, Zimmermann M, Durocher D, de Lange T. 2018. 53BP1-RIF1-shieldin counteracts DSB resection through CST- and Pol $\alpha$ -dependent fill-in. *Nature* **560**: 112–116.
- Mirman Z**, Sasi NK, King A, Chapman JR, de Lange T. 2022. 53BP1-shieldin-dependent DSB processing in BRCA1-deficient cells requires CST-Pol $\alpha$ -primase fill-in synthesis. *Nature cell biology* **24**, 51–61.
- Mirman Z**, Cai S, de Lange T. (2023) CST/Pol $\alpha$ /primase-mediated fill-in synthesis at DSBs. *Cell Cycle* **22**, 379–389.
- Moore JK**, Haber JE. 1996. Cell cycle and genetic requirements of two pathways of nonhomologous end-joining repair of double-strand breaks in *Saccharomyces cerevisiae*. *Molecular and Cellular Biology* **16**, 2164–2173.
- Moreau S**, Ferguson JR, Symington LS. 1999. The nuclease activity of Mre11 is required for meiosis but not for mating type switching, end joining, or telomere maintenance. *Molecular and Cellular Biology* **19**: 556–566.
- Morrison A**, Christensen RB, Alley J, Beck AK, Bernstine EG, Lemontt JF, Lawrence CW. 1989. *REV3*, a *Saccharomyces cerevisiae* gene whose function is required for induced mutagenesis, is predicted to encode a nonessential DNA polymerase. *The Journal of Bacteriology* **171**: 5659–5667.
- Muniyappa K**, Kshirsagar R, Ghodke I. 2014. The HORMA domain: An evolutionarily conserved domain discovered in chromatin-associated proteins, has unanticipated diverse functions. *Gene* **545**: 194–197.
- Nelson JR**, Lawrence CW, Hinkle DC. 1996. Thymine-thymine dimer bypass by yeast DNA polymerase  $\zeta$ . *Science* **272**: 1646–1649.
- Noordermeer SM**, Adam S, Setiaputra D, Barazas M, Pettitt SJ, Ling AK, Olivieri M, Álvarez-Quilón A, Moatti N, Zimmermann M, et al. 2018. The shieldin complex mediates 53BP1-dependent DNA repair. *Nature* **560**: 117–121.
- Northam MR**, Garg P, Baitin DM, Burgers PM, Shcherbakova PV. 2006. A novel function of DNA polymerase  $\zeta$  regulated by PCNA. *The EMBO Journal* **25**: 4316–4325.
- Oh J**, Al-Zain A, Cannavo E, Cejka P, Symington LS. 2016. Xrs2 Dependent and independent functions of the Mre11-Rad50 complex. *Molecular Cell* **64**: 405–415.
- Paeschke K**, Bochman ML, Garcia PD, Cejka P, Friedman KL, Kowalczykowski SC, Zakian VA. 2013. Pif1 family helicases suppress genome instability at G-quadruplex motifs. *Nature* **497**: 458–462.
- Paeschke K**, Capra JA, Zakian VA. 2011. DNA replication through G-quadruplex motifs is promoted by the *Saccharomyces cerevisiae* Pif1 DNA helicase. *Cell* **145**: 678–691.
- Paniagua I**, Jacobs JJL. 2023. Freedom to err: The expanding cellular functions of translesion DNA polymerases. *Molecular Cell* **83(20)**: 3608–3621.
- Paull TT**, Gellert M. 1998. The 3' to 5' exonuclease activity of Mre11 facilitates repair of DNA double-strand breaks. *Molecular Cell* **1**: 969–979.
- Paull TT**. 2018. 20 Years of Mre11 biology: No end in sight. *Molecular Cell* **71**: 419–427.
- Piano V**, Alex A, Stege P, Maffini S, Stoppiello GA, Huis In 't Veld PJ, Vetter IR, Musacchio A. 2021. CDC20 assists its catalytic incorporation in the mitotic checkpoint complex. *Science* **371**, 67–71.
- Pilzecker B**, Buoninfante OA, Jacobs H. 2019. DNA damage tolerance in stem cells, ageing, mutagenesis, disease and cancer therapy. *Nucleic Acids Research* **47**: 7163–7181.
- Prakash S**, Johnson RE, Prakash L. 2005. Eukaryotic translesion synthesis DNA polymerases: specificity of structure and function. *Annual Review of Biochemistry* **74**: 317–353.
- Pustovalova Y**, Bezsonova I, Korzhnev DM. 2012. The C-terminal domain of human Rev1 contains independent binding sites for DNA polymerase  $\eta$  and Rev7 subunit of polymerase

- ζ. *FEBS Letters* **586**: 3051-3056.
- Quah SK**, von Borstel RC, Hastings PJ. 1980. The origin of spontaneous mutation in *Saccharomyces cerevisiae*. *Genetics* **96**: 819-839.
- Rhodes D**, Lipps HJ. 2015. G-quadruplexes and their regulatory roles in biology. *Nucleic Acids Research* **43**: 8627-8637.
- Regairaz M**, Zhang YW, Fu H, Agama KK, Tata N, Agrawal S, Aladjem MI, Pommier Y. 2011. Mus81-mediated DNA cleavage resolves replication forks stalled by topoisomerase I-DNA complexes. *J Cell Biol*. **195**:739-749.
- Rizzo AA**, Vassel FM, Chatterjee N, D'Souza S, Li Y, Hao B, Hemann MT, Walker GC, Korzhnev DM. 2018. Rev7 dimerization is important for assembly and function of the Rev1/Polζ translesion synthesis complex. *Proceedings of the National Academy of Sciences USA* **115**: E8191-E8200.
- Rosenberg SC**, Corbett KD. 2015. The multifaceted roles of the HORMA domain in cellular signaling. *The Journal of Cell Biology* **211**: 745-755.
- Sambrook J**, Russell DW. 2001. Molecular Cloning: A Laboratory Manual. 3: *Cold Spring Harbor Laboratory, Cold Spring Harbor, New York*.
- Sarangi P**, Clairmont CS, Galli LD, Moreau LA, D'Andrea AD. 2020. p31comet promotes homologous recombination by inactivating REV7 through the TRIP13 ATPase. *Proceedings of the National Academy of Sciences USA* **117**: 26795-26803.
- Sarkies P**, Murat P, Phillips LG, Patel KJ, Balasubramanian S, Sale JE. 2012. FANCJ coordinates two pathways that maintain epigenetic stability at G-quadruplex DNA. *Nucleic Acids Research* **40**: 1485-1498.
- Sarkies P**, Reams C, Simpson LJ, Sale JE. 2010. Epigenetic instability due to defective replication of structured DNA. *Molecular Cell* **40**: 703-713.
- Sato K**, Knipscheer P. 2023. G-quadruplex resolution: From molecular mechanisms to physiological relevance. *DNA Repair* **130**:103552.
- Setiaputra D**, Durocher D. 2019. Shieldin- the protector of DNA ends. *EMBO Reports* **20**, e47560.
- Shibata A**, Moiani D, Arvai AS, Perry J, Harding SM, Genois MM, Maity R, van Rossum-Fikkert S, Kertokalio A, Romoli F, et al. 2014. DNA double-strand break repair pathway choice is directed by distinct MRE11 nuclease activities. *Molecular Cell* **53**: 7-18.
- Sonoda E**, Okada T, Zhao GY, Tateishi S, Araki K, Yamaizumi M, Yagi T, Verkaik NS, van Gent DC, Takata M, Takeda S. 2003. Multiple roles of Rev3, the catalytic subunit of polzeta in maintaining genome stability in vertebrates. *The EMBO Journal* **22**: 3188-3197.
- Spiegel J**, Adhikari S, Balasubramanian S. 2020. The structure and function of DNA G-quadruplexes. *Trends in Chemistry* **2**: 123-136.
- Stracker TH**, Petrini JH. 2011. The MRE11 complex: starting from the ends. *Nature Reviews Molecular Cell Biology* **12**: 90-103.
- Sun H**, Bennett RJ, Maizels N. 1999. The *Saccharomyces cerevisiae* Sgs1 helicase efficiently unwinds GG paired DNAs. *Nucleic Acids Res*. **27**: 1978-1984.
- Thakur M**, Agarwal A, Muniyappa K. 2021a. The intrinsic ATPase activity of *Mycobacterium tuberculosis* UvrC is crucial for its damage-specific DNA incision function. *The FEBS journal*, **288**: 1179-1200.
- Thakur M**, Badugu S, Muniyappa K. 2020. UvrA and UvrC subunits of the *Mycobacterium tuberculosis* UvrABC excinuclease interact independently of UvrB and DNA. *FEBS Letters* **594**: 851-863.
- Thakur M**, Mohan D, Singh AK, Agarwal A, Gopal B, Muniyappa K. 2021b. Novel insights into ATP-stimulated cleavage of branched DNA and RNA substrates through structure-guided studies of the Holliday junction resolvase RuvX. *The Journal of Molecular Biology* **433**: 167014.
- Tittel-Elmer M**, Alabert C, Pasero P, Cobb JA. 2009. The MRX complex stabilizes the replisome independently of the S phase checkpoint during replication stress. *EMBO J*. **28**:1142-1156.

- Tomida J**, Takata KI, Bhetawal S, Person MD, Chao HP, Tang DG, Wood RD. 2018. FAM35A associates with REV7 and modulates DNA damage responses of normal and BRCA1-defective cells. *The EMBO Journal* **37**: e99543.
- Trujillo KM**, Sung P. 2001. DNA structure-specific nuclease activities in the *Saccharomyces cerevisiae* Rad50-Mre11 complex. *The Journal of Biological Chemistry* **276**, 35458-35464.
- Trujillo KM**, Roh DH, Chen L, Van Komen S, Tomkinson A, Sung P. 2003. Yeast xrs2 binds DNA and helps target rad50 and mre11 to DNA ends. *The Journal of Biological Chemistry* **278**: 48957-48964.
- Tsubouchi H**, Ogawa H. 1998. A novel mre11 mutation impairs processing of double-strand breaks of DNA during both mitosis and meiosis. *Molecular and Cellular Biology* **18**: 260–268.
- Usui T**, Ohta T, Oshiumi H, Tomizawa T, Ogawa H, Ogawa T. 1998. Complex formation and functional versatility of Mre11 of budding yeast in recombination. *Cell* **95**:705-16.
- Vaisman A**, Woodgate R. 2017. Translesion DNA polymerases in eukaryotes: what makes them tick? *Critical Reviews in Biochemistry and Molecular Biology* **52**: 274-303.
- Varadi M**, Anyango S, Deshpande M, Nair S, Natassia C, Yordanova G, et al. 2022. AlphaFold Protein Structure Database: Massively expanding the structural coverage of protein-sequence space with high-accuracy models. *Nucleic Acids Research* **50**: D439–D444.
- You X**, Nguyen AW, Jabaiah A, Sheff MA, Thorn KS, Daugherty PS. (2006) Intracellular protein interaction mapping with FRET hybrids. *Proceedings of the National Academy of Sciences USA* **103**: 18458-18463.
- Wienken CJ**, Baaske P, Rothbauer U, Braun D, Duhr S. 2010. Protein-binding assays in biological liquids using microscale thermophoresis. *Nature Communications* 2010; **1**: 100.
- Xu G**, Chapman JR, Brandsma I, Yuan J, Mistrik M, Bouwman P, Bartkova J, Gogola E, Warmerdam D, Barazas M, et al. 2015. REV7 counteracts DNA double-strand break resection and affects PARP inhibition. *Nature* **521**: 541–544.
- Yadav P**, Kim N, Kumari M, Verma S, Sharma TK, Yadav V, Kumar A. 2021. G-quadruplex structures in bacteria: biological relevance and potential as an antimicrobial target. *The Journal of Bacteriology* **203**: e0057720.
- Zhang X**, Paull TT. 2005. The Mre11/Rad50/Xrs2 complex and non-homologous end-joining of incompatible ends in *S. cerevisiae*. *DNA Repair* **4**: 1281–1294.
- Zhong X**, Garg P, Stith CM, Nick McElhinny SA, Kissling E, Burgers PM, Kunkel TA. 2006. The fidelity of DNA synthesis by yeast DNA polymerase zeta alone and with accessory proteins. *Nucleic Acids Research* **34**: 4731–4742.
- Zubarev RA**, Makarov A. 2013. Orbitrap mass spectrometry. *Analytical Chemistry* **85**, 5288–5296.

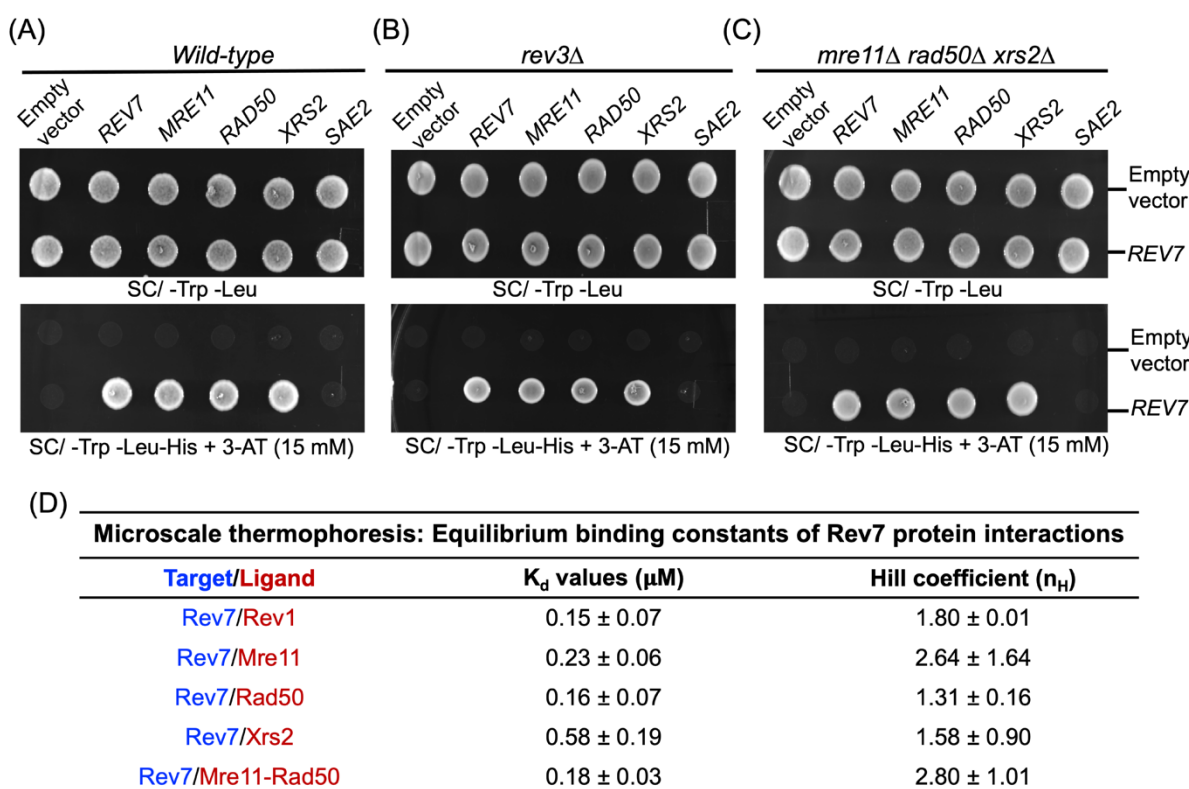


**Figure 1.** Y2H screens suggest interaction between ScRev7 and the MRX subunits. The Y2H assay was performed in: (A) wild-type, (B) *rev3Δ*, and (C) *mre11Δ rad50Δ xrs2Δ* mutant strains in PJ69-4A background. These strains were cotransformed with pairwise combinations of empty vector, bait (pGBT7-*REV7*) and prey (pGAD7/*MRE11*, *RAD50*, *XRS2*, *REV7* or *SAE2*) plasmids. Equal number of mid-log phase cells were spotted onto the SC/-Trp -Leu agar plates (upper panels) or SC/-Trp -Leu -His agar plates containing 3-AT (bottom panels). Cells were imaged after 48 h of growth at 30°C. The images shown in panels (A), (B) and (C) are representative of three independent experiments. (D) Quantitative parameters for interaction between ScRev7 and Rev1, Mre11, Rad50, Xrs2 or Mre11-Rad50 proteins.

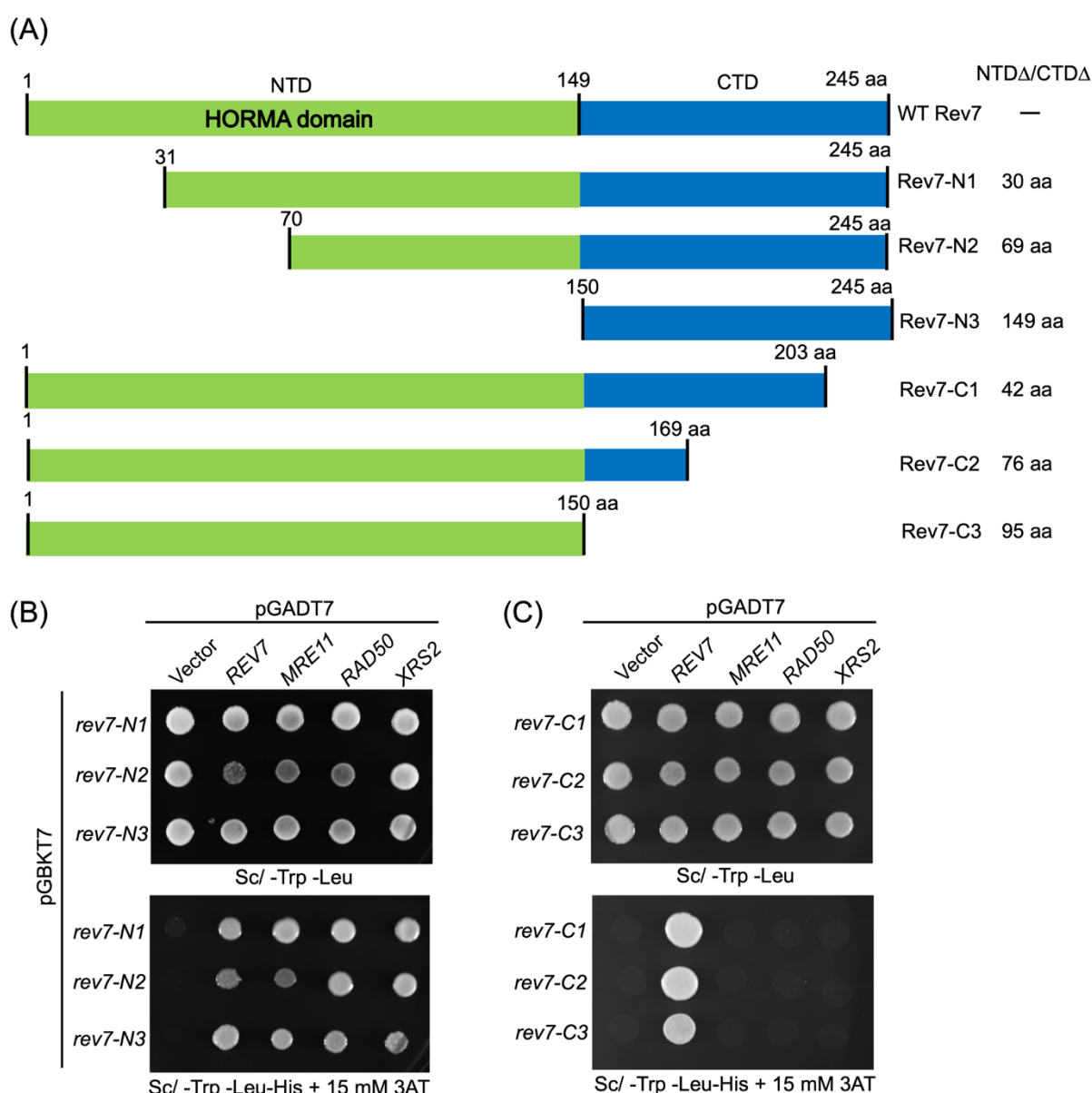


**Figure 2.** Deletion analysis revealed that the C-terminal 42 amino acids of ScRev7 are critical for its binding to the MRX subunits. **(A)** Schematic representation of the full-length and truncated ScRev7 variants. The truncated species lacking the indicated number of amino acids (aa) in the N-terminal domain (NTD $\Delta$ ) or C-terminal domain (CTD $\Delta$ ) is indicated on the right-hand side of the figure. **(B)** Representative images of spot assays of cells carrying pairwise combination of empty vector, bait and prey plasmids expressing N-terminally truncated species of Rev7 and full-length Rev7, Mre11, Rad50, Xrs2, respectively. **(C)** Same as panel **(B)**, but with the bait plasmids encoding C-terminally truncated Rev7 variants. Cells were imaged after 48h of growth at 30 °C. Y2H assay was performed as described in the legend to [Figure 1](#). Data are representative of three independent experiments.

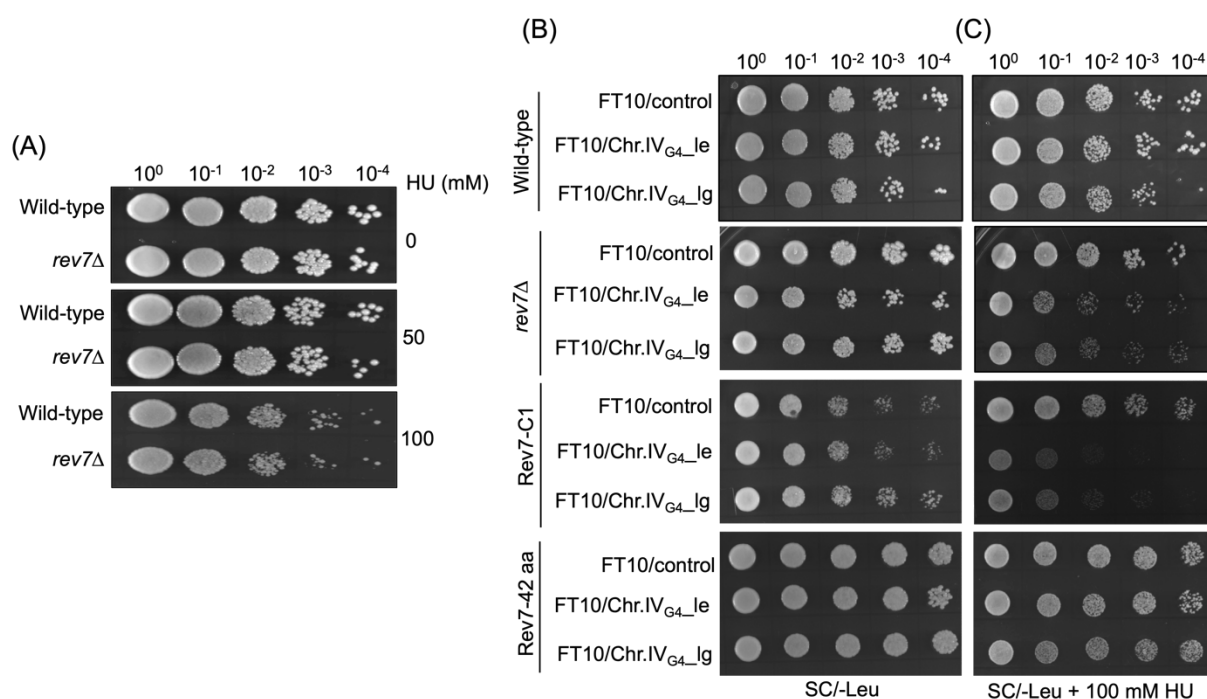


**Figure 3.** A 42-amino acid segment at the extreme C-terminus of ScRev7 renders cells resistant to the synergistic adverse effect of G-quadruplex DNA and HU. **(A)** *REV7* deletion does not affect HU sensitivity of *rev7 $\Delta$  cells. Representative images of YPD plates showing spot assay of wild-type W1588-4C strain and its derivative *rev7* mutant cells, in the absence or presence of 50 or 100 mM HU. **(B)** Representative images of SC/-Leu agar plates showing spot assay of WT, *rev7 $\Delta$ , *rev7*-C1 or *rev7*-42 aa cells harboring the indicated plasmids carrying G-quadruplex capable sequences derived from chromosome IV (Chr.IV<sub>G4</sub>). The cells were grown on SC/-Leu agar plates in the absence of HU. **(C)** Same as panel **(B)**, but the growth medium contained 100 mM HU. For serial dilutions, each strain was grown in SC/-Leu medium, normalized to OD<sub>600</sub> = 1.0, and serially diluted using yeast nitrogen base medium. Five  $\mu$ l aliquots from the serial dilutions were spotted onto the SC/-Leu agar plates with or without HU. FT10/Control plasmid lacks the G-quadruplex DNA insert. The abbreviations “le” and “Ig” stand for leading and lagging strands, respectively. Cells were imaged after 4 days of growth at 30 °C. Data are representative of three independent experiments.**

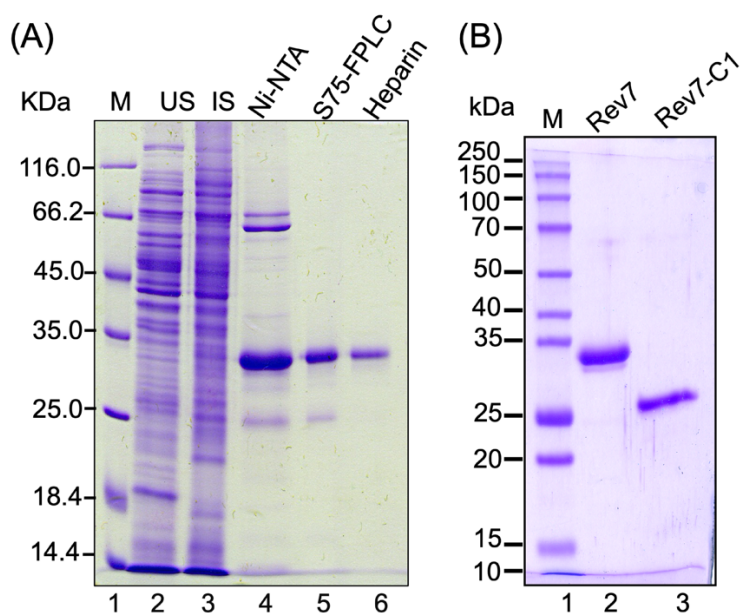


**Figure 4.** Purification of ScRev7 and ScRev7-C1 proteins. **(A)** SDS-PAGE analysis of protein samples from different stages of ScRev7 purification. Lane 1: standard protein markers; 2, uninduced cell lysate (10 µg); 3, induced cell lysate (10 µg); 4, Ni<sup>2+</sup>-NTA column eluate (3 µg); 5, Superdex S75 column eluate (1 µg); 6, eluate from heparin column (0.8 µg). **(B)** SDS-PAGE analysis of purified truncated ScRev7-C1 variant. Lane 1: standard protein markers. Lanes 2 and 3, purified full length ScRev7 and ScRev7-C1 variant.

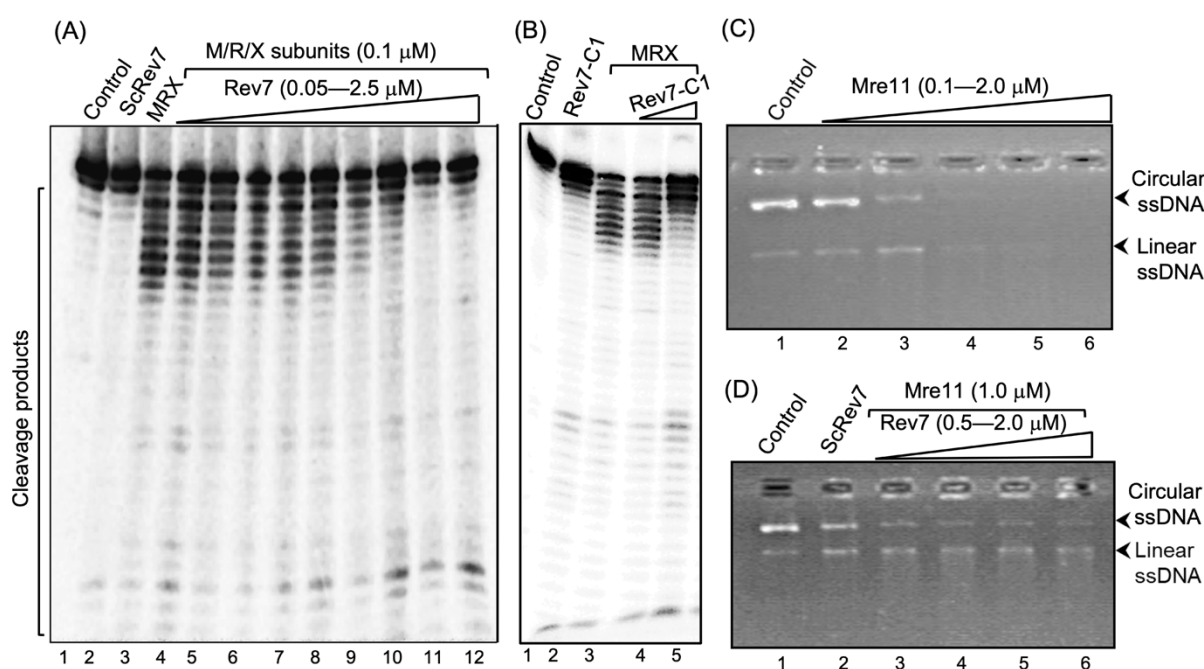


**Figure 5.** ScRev7 impedes both exo- and endonucleolytic activities of the MRX subunits. **(A)** A representative image showing the effect of ScRev7 on the exonuclease activity of MRX complex. Reaction mixtures containing 5 nM  $^{32}\text{P}$ -labelled 60 bp dsDNA were incubated in the absence or presence of M/R/X subunits and various amounts of ScRev7. Lane 1,  $^{32}\text{P}$ -labelled dsDNA. Lane 2, same as in lane 1, but with 2.5  $\mu\text{M}$  ScRev7. Lane 3, same as in lane 1, but with M/R/X subunits (0.1  $\mu\text{M}$  each). Lanes 4-12, same as in lane 3, but with 0.05, 0.1, 0.3, 0.5, 0.7, 1, 1.5, 2 and 2.5  $\mu\text{M}$  of ScRev7, respectively. **(B)** A representative image showing the effect of Rev7-C1 variant on the exonuclease activity of the MRX complex. Assay was performed as in panel **(A)**, but with ScRev7-C1 variant. Lane 1,  $^{32}\text{P}$ -labelled dsDNA. Lane 2, same as in lane 1, but with 2.5  $\mu\text{M}$  ScRev7-C1 variant. Lane 3, same as in lane 1, but with M/R/X subunits (0.1  $\mu\text{M}$  each). Lanes 4-5, same as in lane 3, but with 1.5 and 3.0  $\mu\text{M}$  of ScRev7-C1 variant, respectively. **(C)** A representative image showing Mre11 endonuclease activity on circular ssDNA. Reaction mixtures containing 100 ng M13 circular ssDNA were incubated without (lane 1) or with 0.1, 0.5, 1, 1.5 and 2  $\mu\text{M}$  Mre11, respectively (lanes 2-6). **(D)** A representative image showing the effect of ScRev7 on Mre11 endonuclease activity by ScRev7. Reaction mixtures containing 1  $\mu\text{M}$  Mre11 were pre-incubated with 0.5, 1.0 1.5 and 2  $\mu\text{M}$  of ScRev7 (lanes 3-6 respectively), prior to the addition of 100 ng of M13 circular ssDNA. Lane 1, circular ssDNA alone. Lane 2, same as in lane 1, but with 2  $\mu\text{M}$  of ScRev7. Increasing concentrations of the indicated protein is represented by open triangles at the top of the gel.

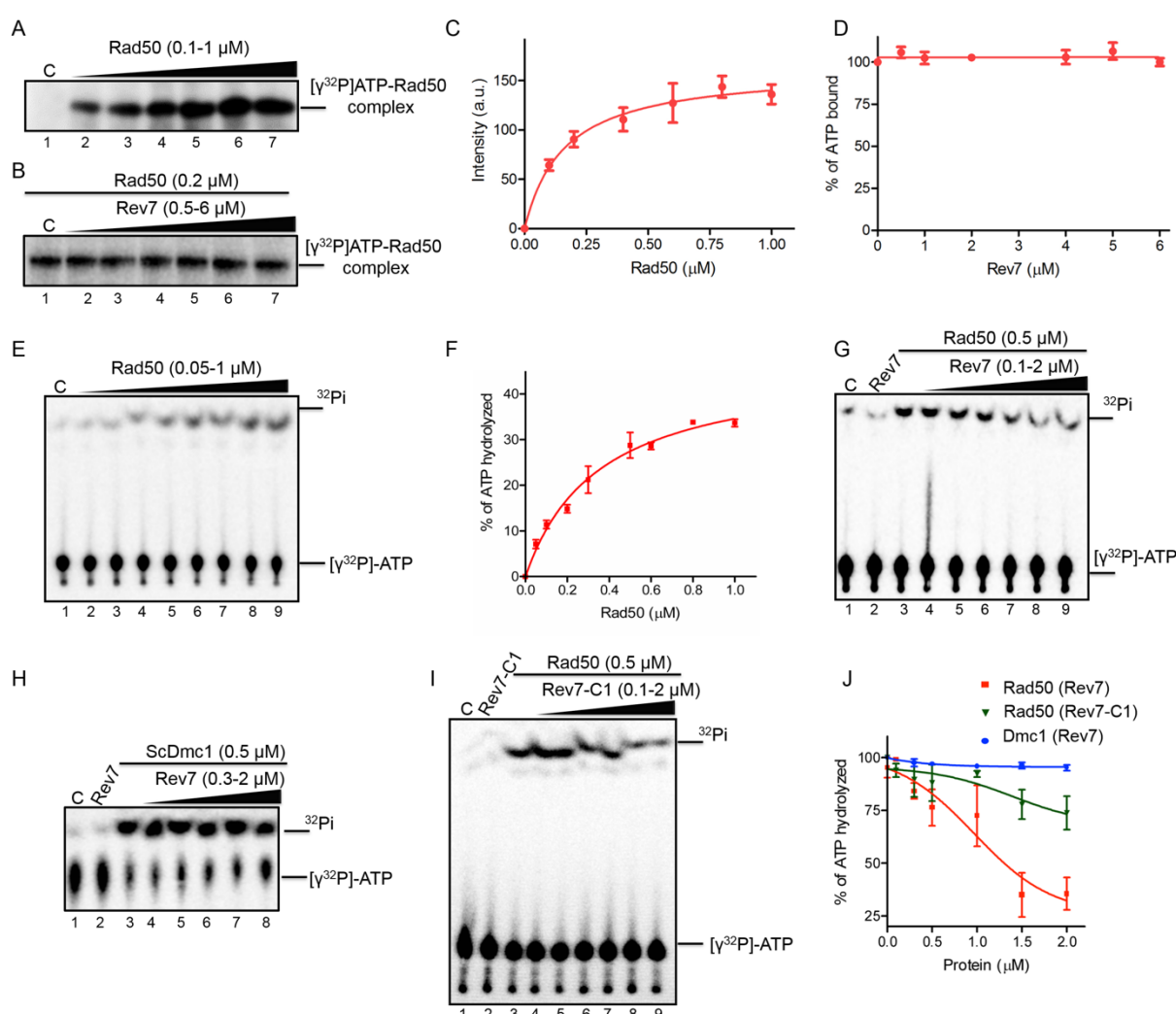


**Figure 6.** Rev7 inhibits the ATPase activity of Rad50 without impacting its ability to bind ATP. **(A)**, Rad50 binds [ $\gamma$ -<sup>32</sup>P]ATP in a dose-dependent manner. Lane 1, no protein. Lanes 2-7, reactions were performed with 0.1, 0.2, 0.4, 0.6, 0.8 and 1  $\mu$ M of Rad50 and 400 pmol [ $\gamma$ -<sup>32</sup>P]ATP. **(B)** ScRev7 does not affect the ability of Rad50 to bind ATP. Lane 1, Rad50 and 400 pmol [ $\gamma$ -<sup>32</sup>P]ATP. Lanes 2-7, same as in lane 1, but with 0.5, 1, 2, 4, 5, and 6  $\mu$ M of ScRev7, respectively. **(C)** Quantification of ATP binding by Rad50 as a function of its concentration. **(D)** Quantification of the effect of ScRev7 on ATP binding by Rad50. **(E)** ATPase activity of Rad50 as a function of its concentration. Reactions were performed in the absence (lane 1) or presence (lanes 2-9) of 0.05, 0.1, 0.2, 0.3, 0.5, 0.6, 0.8 and 1  $\mu$ M of Rad50, respectively. **(F)** Quantification of Rad50 ATPase activity as a function of its concentration. **(G)** ScRev7 abrogates ATP hydrolysis catalyzed by Rad50. **(H)** ScRev7 does not impact the ability of ScDmc1 to hydrolyze ATP. Lane 1 contained 400 pmol [ $\gamma$ -<sup>32</sup>P]ATP; lane 2, same as in lane 1, but with 2  $\mu$ M of ScRev7; lane 3, as in lane 1, but with 0.5  $\mu$ M of ScDmc1; lanes 4-8, as in lane 3, but with 0.3, 0.5, 1, 1.5 and 2  $\mu$ M ScRev7, respectively. **(I)** ScRev7-C1 variant impedes ATP hydrolysis catalyzed by Rad50. In panels (G) and (I) lane 1 contained 400 pmol [ $\gamma$ -<sup>32</sup>P]ATP; lane 2, same as in lane 1, but 2  $\mu$ M ScRev7/ScRev7-C1 variant; lane 3, as in lane 1, but with 0.5  $\mu$ M Rad50; lanes 4-9, as in lane 3, but with 0.1, 0.3, 0.5, 1, 1.5 and 2  $\mu$ M ScRev7/ScRev7-C1 variant, respectively. **(J)** Quantification of the inhibitory effect of ScRev7/ScRev7-C1 on ATP hydrolysis catalyzed by Rad50 or ScDmc1. The closed triangles on the top of gel images in panels **(A)**, **(B)**, **(E)**, **(G)**, **(H)** and **(I)** represent increasing concentrations of Rad50, ScRev7 or ScRev7-C1. Error bars indicate SEM, and data are representative of three independent experiments.

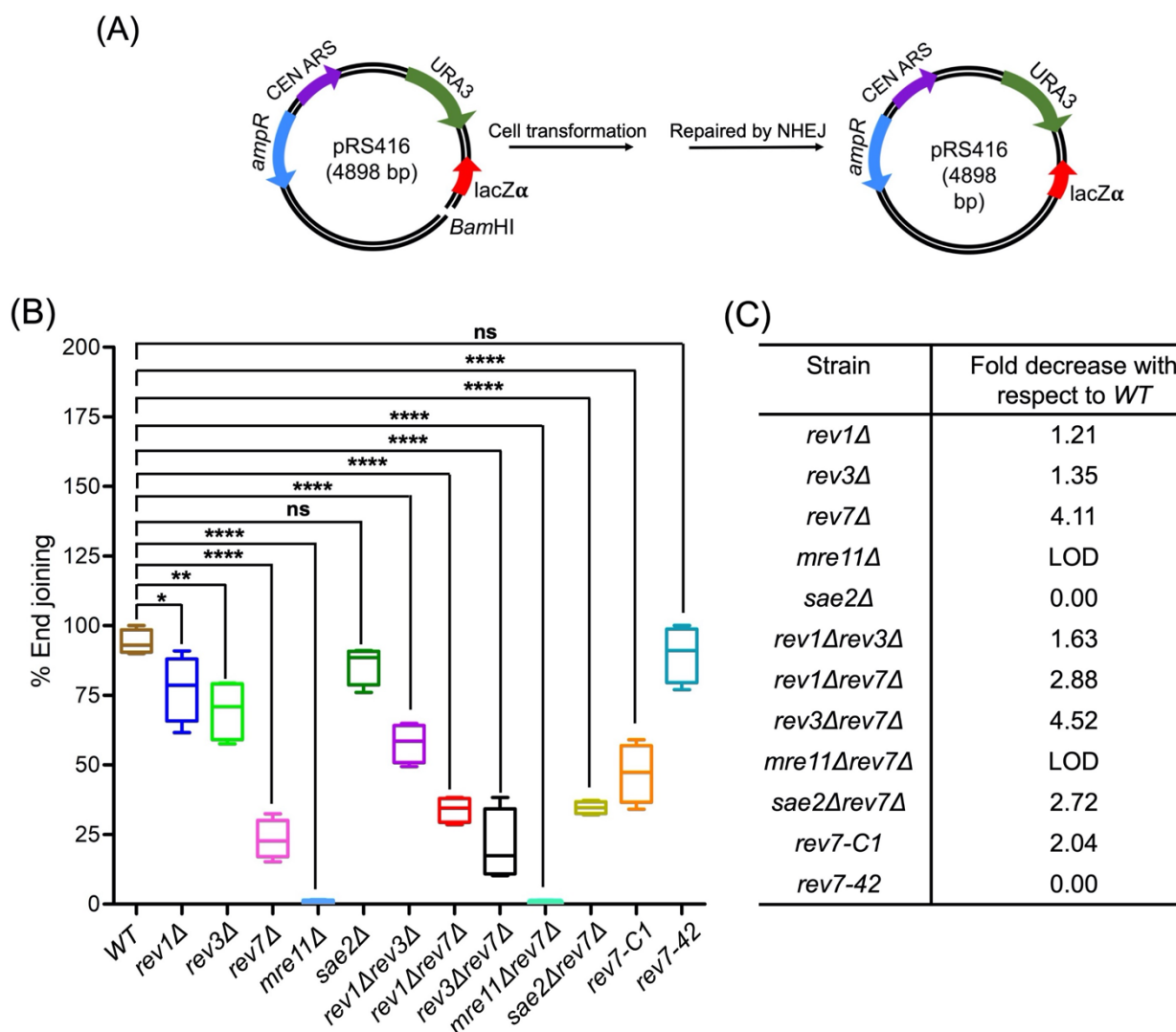


**Figure 7. *S. cerevisiae REV7* promotes NHEJ-mediated DSB repair.** (A) Map of the NHEJ reporter plasmid and the experimental workflow. Sixty ng of uncut or linearized pRS416 plasmid DNA was transformed into the WT (W1588-4C) and indicated isogenic mutants carrying single or double deletions. Transformants were selected on SC medium lacking uracil. (B) Quantification of NHEJ efficiency relative to WT cells. (C) Quantification of fold decrease in the efficiency of NHEJ relative to the WT. The boxes represent mean; whiskers, minimum and maximum values. “LOD” denotes below the level of detection compared with the WT. The data are presented as the mean  $\pm$  SEM of four independent experiments. n.s.: not significant, \* $p < 0.05$ , \*\* $p < 0.005$ , \*\*\* $p < 0.0001$  vs. control. The exact p-values are presented in *Supplementary Table S3*.

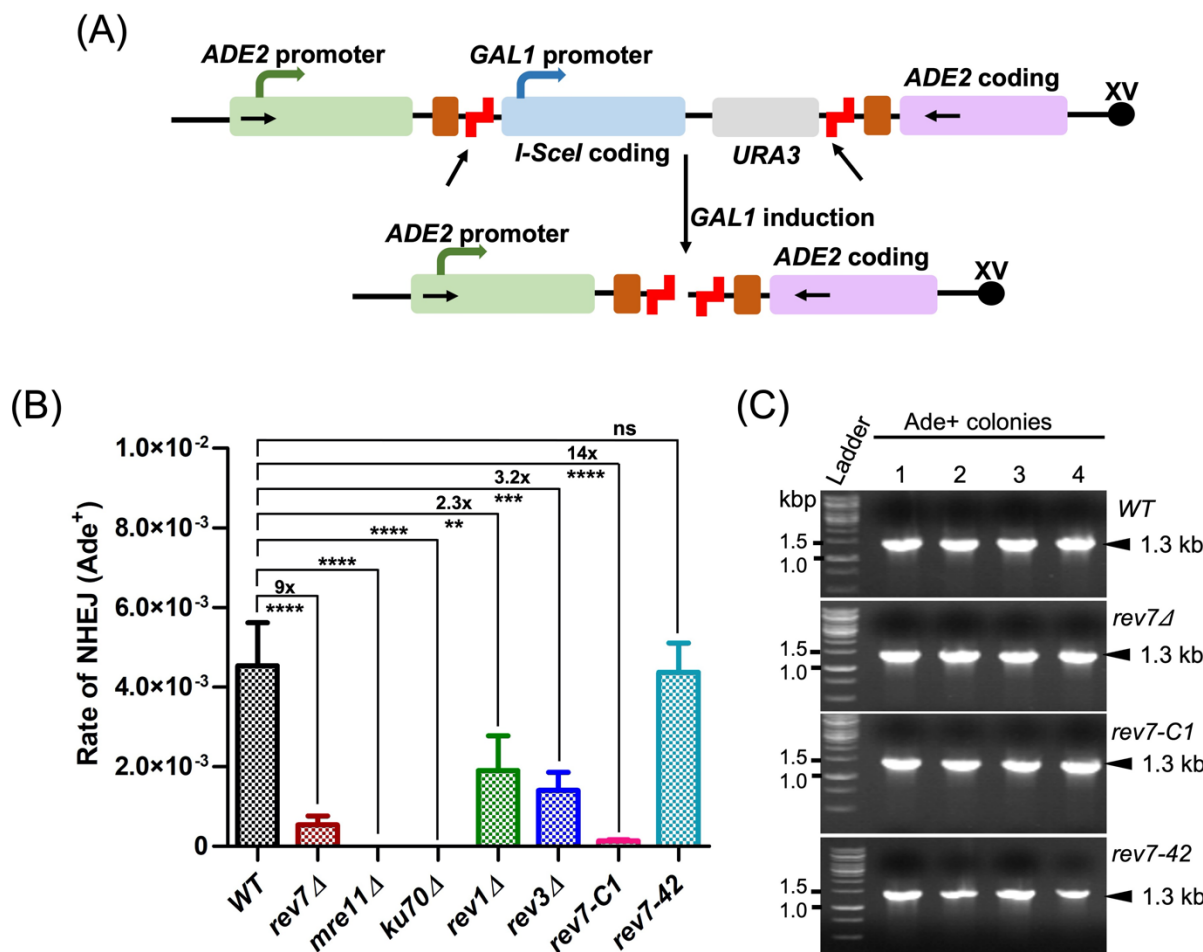


**Figure 8.** *S. cerevisiae REV7* facilitates chromosomal DSB repair via NHEJ pathway. **(A)** A schematic diagram showing the “suicide deletion” cassette at the *ADE2* locus of chromosome XV [redrawn from ref. Karathanasis and Wilson, 2002]. The arrows indicate the locations of PCR primers. Brown and staggered red boxes correspond to direct repeats and I-SceI cleavage sites, respectively. **(B)** Quantification of NHEJ efficiency in the wild-type YW714 and derivative mutant strains. **(C)** Representative gel images of PCR-amplified DNA products from Ade<sup>2+</sup> transformant cells. Data are means  $\pm$  SEM from three independent experiments. n.s.: not significant, \*\* $p < 0.005$ , \*\*\* $p < 0.001$ , \*\*\*\* $p < 0.0001$  vs. control, as assessed by one-way ANOVA Dunnett's multiple comparison test. The exact p-values are presented in *Supplementary Table S4*.

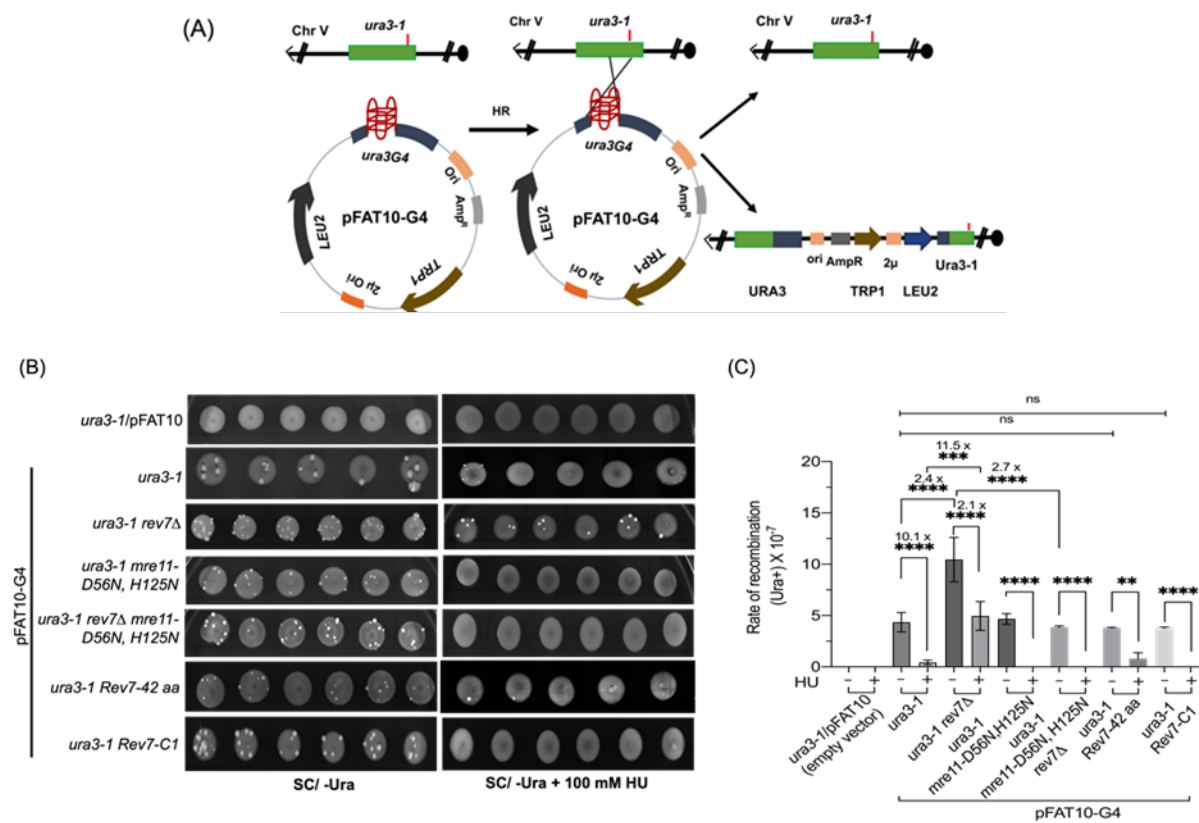


**Figure 9.** Deletion of *REV7* increases the frequency of mitotic HR. **(A)** Schematic representation of plasmid-chromosome recombination assay. The *ura3-1* and *ura3-G4* alleles are located on chromosome V and plasmid pFAT10-G4, respectively. Recombination between a plasmid borne *ura3-G4* allele and the chromosomal borne *ura3-1* allele would result in Ura<sup>+</sup> prototrophs. **(B)** Representative images of Ura3<sup>+</sup> papillae on SC/-Ura agar plates in the absence or presence of 100 mM HU. **(C)** Quantification of the rate of HR frequency in different strains. Data are presented as mean ± SD from three different experiments. ns, not significant, \*\*p < 0.01, \*\*\*p < 0.001, \*\*\*\*p < 0.0001 vs. control, as assessed using one-way ANOVA and Tukey's post hoc test.

## Supplemental figures and legends

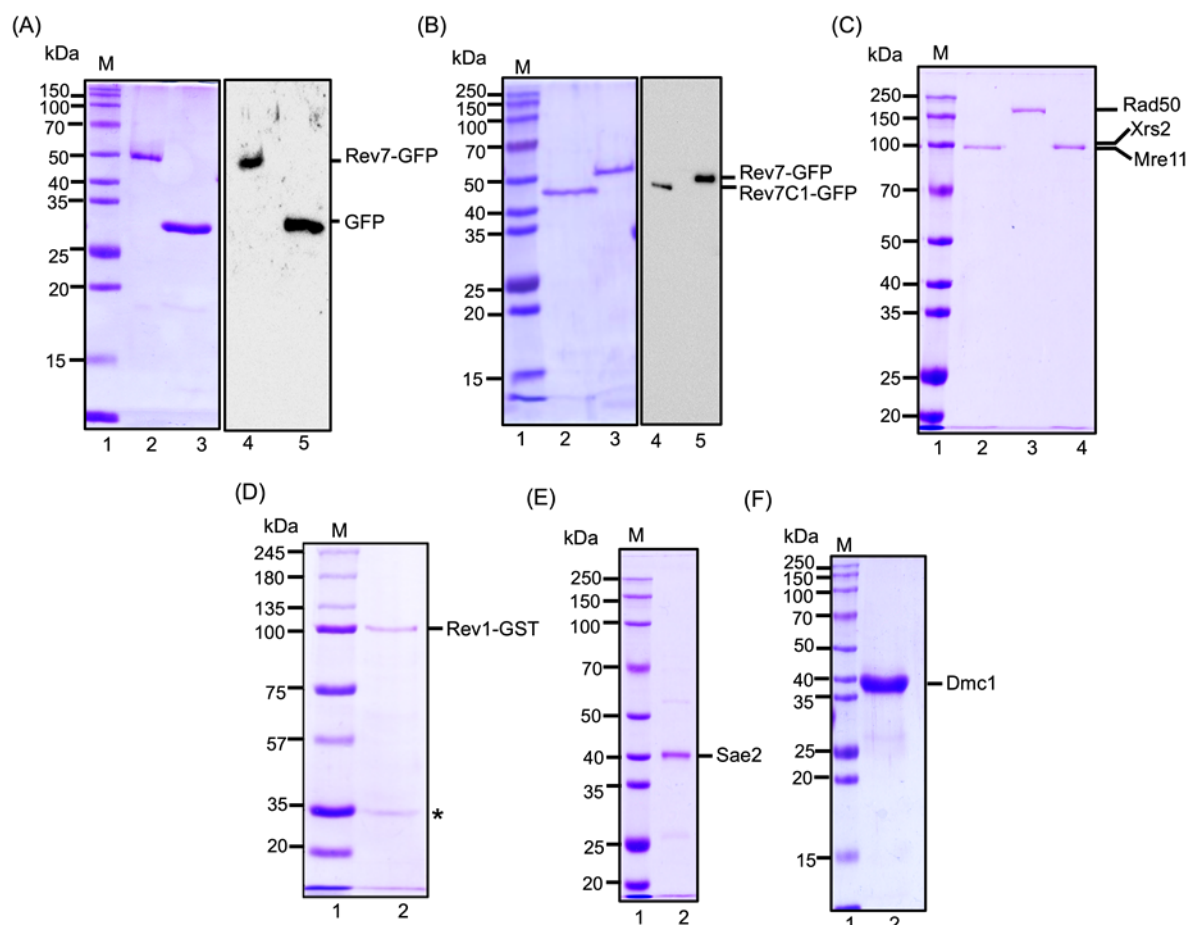


**Figure 1—figure supplement 1. SDS-PAGE analysis of purified proteins used in this study.** (A) SDS-PAGE and Western blot analysis of purified GFP-tagged ScRev7 and eGFP. Lane 1 (in panels A-F) standard molecular weight markers; lane 2, purified GFP-tagged ScRev7; lane 3, purified GFP. Western blot analysis of GFP-tagged Rev7 (lane 4) and eGFP (lane 5) using mouse anti-GFP antibodies. (B) Purified GFP-tagged Rev7-C1 (2) and GFP-tagged Rev7 (3). Western blot analysis of GFP-tagged Rev7-C1 (4) and GFP-tagged Rev7 (5) using mouse anti-GFP antibodies. (C) Purified MRX subunits; lane 2, Mre11; lane 3, Rad50; lane 4, Xrs2; (D) Purified GST-tagged Rev1; The faster migrating band (\*) corresponds to ScRev7, which co-purifies with GST-tagged Rev1 (Acharya et al., 2005). (E) Purified Sae2 and (F) Purified Dmc1.

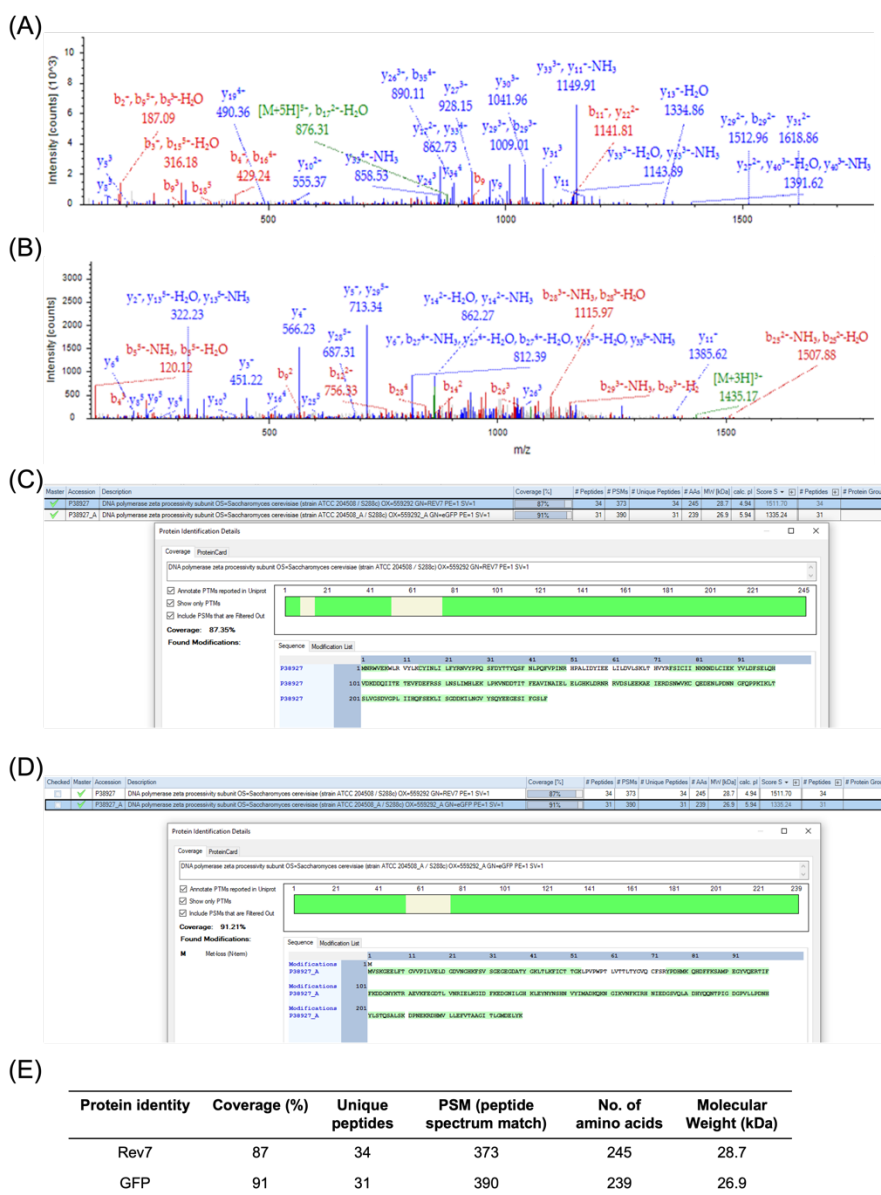


**Figure 1—figure supplement 2.** Representative spectra for unique peptides obtained after trypsin digestion of Rev7-GFP protein that match with **(A)** GFP sequence, **(B)** ScRev7 sequence. **(C)** Snapshot of sequence coverage (shown in green) obtained for Rev7 and **(D)** GFP. **(E)** Table summarizes data obtained for Orbitrap LC-MS performed using purified Rev7-GFP protein.

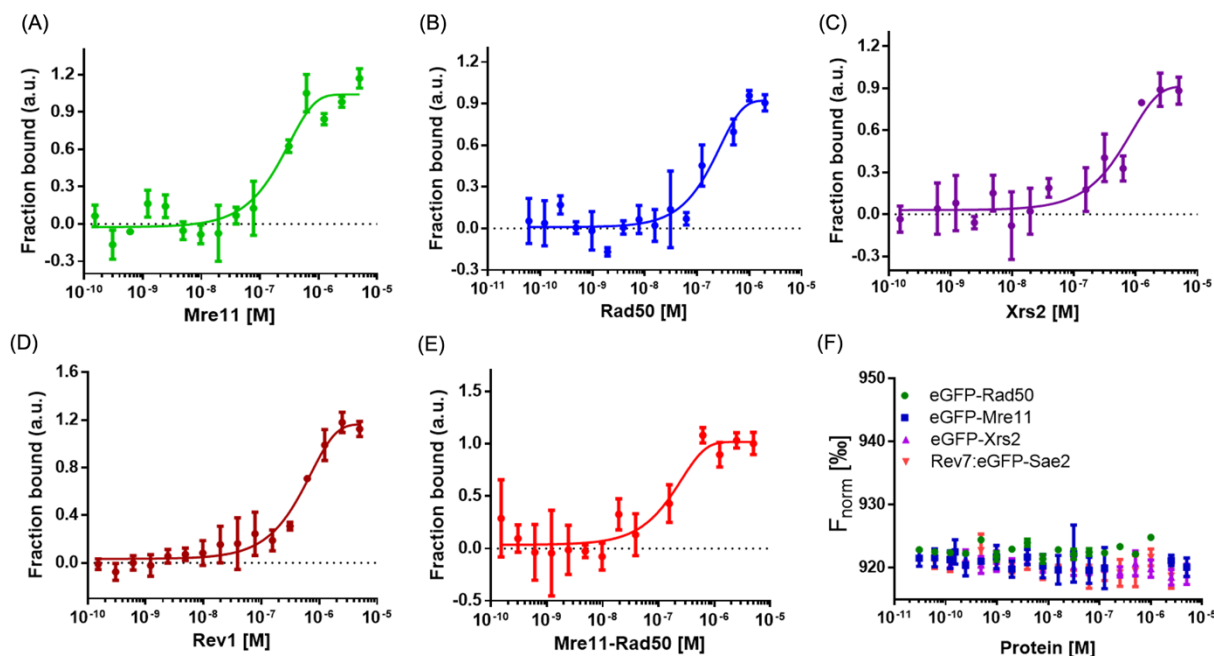


**Figure 1—figure supplement 3. Microscale thermophoresis reveals a direct interaction between Rev7 and MRX subunits.** Normalised MST binding curves were generated for the titration of (A) Mre11, (B) Rad50, (C) Xrs2, (D) Rev1, (E) the Mre11-Rad50 complex, and (F) Sae2 proteins against Rev7-eGFP. Panel F also includes datasets for the binding of Mre11, Rad50, and Xrs2 against eGFP. Error bars represent the standard error of the mean (SEM), and data are representative of three independent experiments.

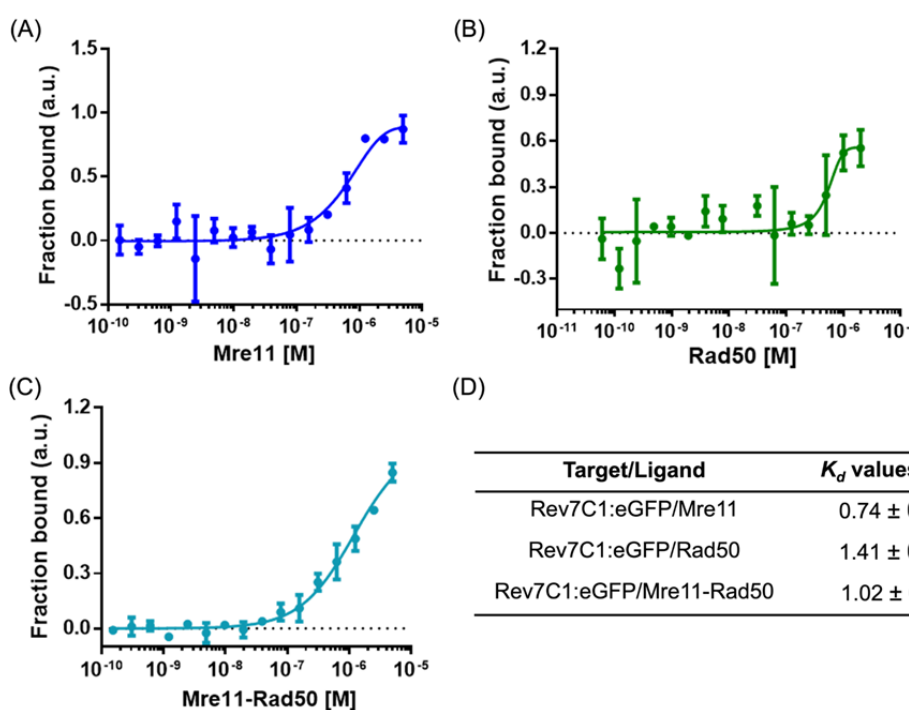


**Figure 1—figure supplement 4.** Rev7-C1 exhibits weak interactions with MRX subunits. Binding isotherms were obtained by incubating increasing concentrations of (A) Mre11 (0.00015 to 5 μM), (B) Rad50 (0.00006 to 2 μM), and (C) MR complex (0.00015 to 5 μM) with fixed concentration of Rev7C1:GFP protein (0.25 μM). (D)  $K_d$  values obtained upon fitting the curves in  $K_d$  model using MO affinity analysis software (Nanotemper). Data is representative of three independent experiments.

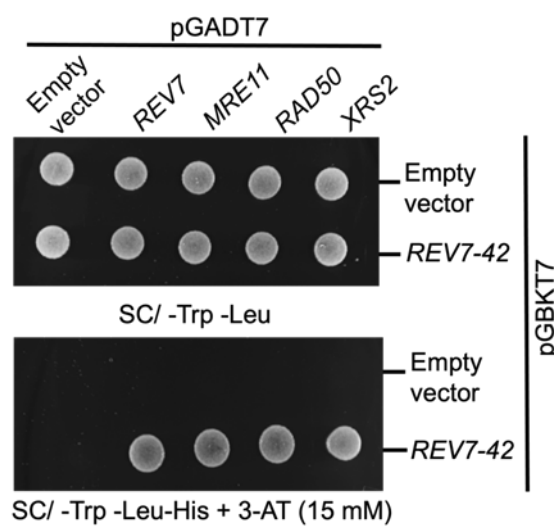


**Figure 2—figure supplement 1. The C-terminal 42 amino-acid region of Rev7 interacts with M/R/X subunits.** The PJ69-4A cells were co-transformed with empty vectors or vectors expressing Rev7-42 residue peptide or MRX subunits as indicated. Equal number of cells were spotted onto -Trp-Leu and -Trp-Leu-His selection plates containing 15 mM 3-AT and incubated at 30 °C for 2 days.

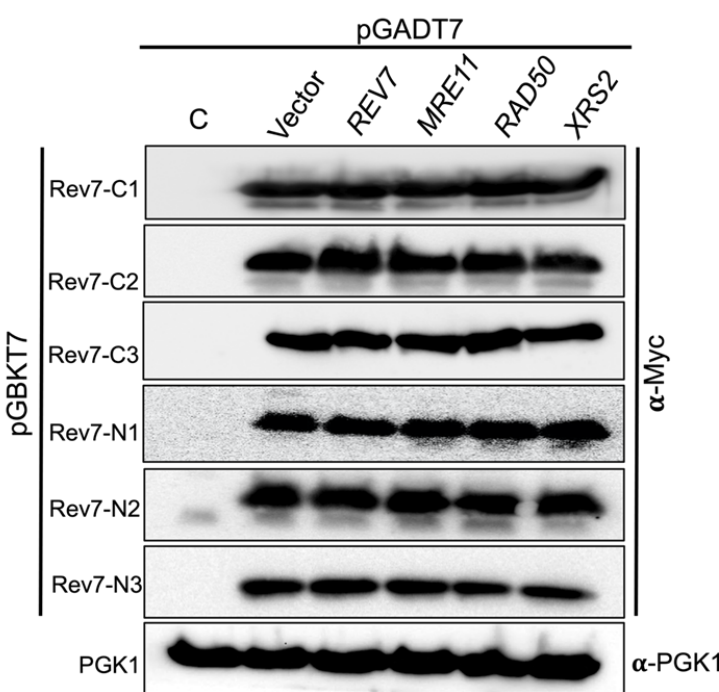


**Figure 2—figure supplement 2. Western blot showing the abundance of N- and C-terminally truncated variants of Rev7.** *S. cerevisiae* PJ69-4A cells were co-transformed with the indicated bait plasmid expressing c-Myc epitope tagged N- or C-terminally truncated variant of Rev7 (REV7-C1, REV7-C2, REV7-C3, REV7-N1, REV7-N2 or REV7-N3) with and a prey plasmid expressing *REV7*, *MRE11*, *RAD50* or *XRS2*. PGK-1 was used as the loading control and was probed with anti-PGK-1 antibodies. Sample loading was normalized to similar amounts by determining the protein concentration utilizing the dye-binding assay. Lane 'C' represents lysates from cells harboring empty bait and prey vectors.

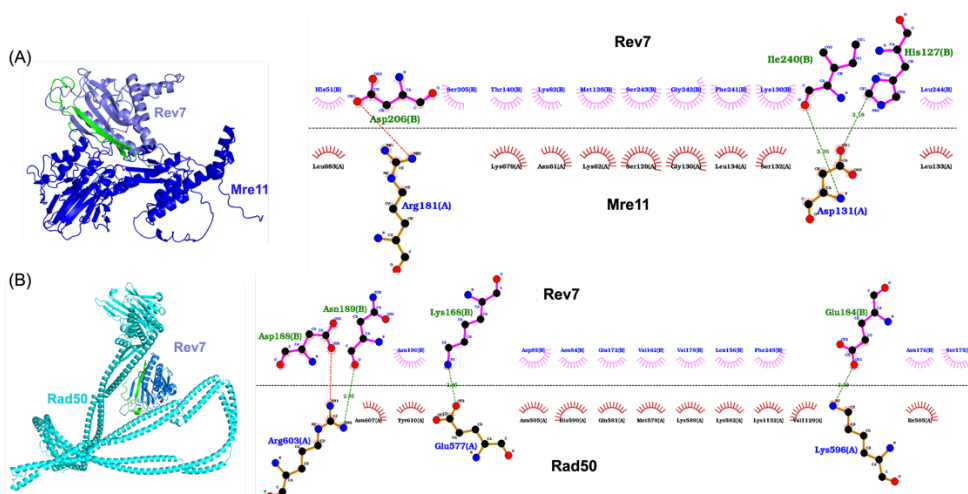


**Figure 2—figure supplement 3. AlphaFold-Multimer generated models of Rev7-Mre11 and Rev7-Rad50 protein complexes.** (A) Model of the Rev7-Mre11 heterodimer, Rev7, light blue, Mre11, deep blue. (B) Model of Rev7-Rad50 heterodimer, Rev7, light blue, Rad50, cyan. Alongside is the two-dimensional view of the corresponding protein-protein binding interface as generated by the LigPlot software. Numbers indicated on the dotted lines represent bond-lengths in Angstroms. The C-terminal safety belt region of Rev7 is coloured in green in both complexes. By convention, red, black and blue circles represent oxygen, carbon and nitrogen atoms respectively. The dashed line represents the interaction interface.

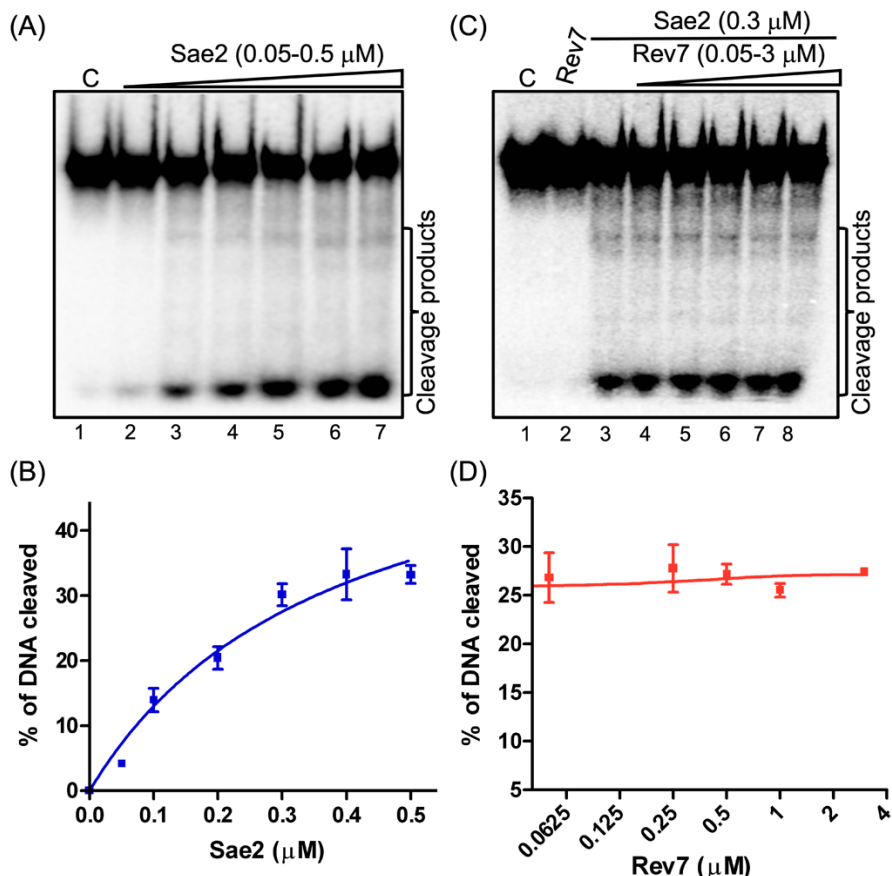


**Figure 5—figure supplement 1: Rev7 does not impact the endonuclease activity of Sae2.** (A) Sae2-catalyzed cleavage of  $^{32}\text{P}$ -labeled 60 bp dsDNA. Reaction mixtures containing 5 nM dsDNA were incubated with increasing concentrations of Sae2. Lane 1: control reaction without protein; Lanes 2–7: Sae2 at 0.05, 0.1, 0.2, 0.3, 0.4, and 0.5  $\mu\text{M}$ , respectively. (B) Quantification of Sae2 endonuclease activity as a function of its concentration. (C) A representative image demonstrating the effect of Rev7 on the endonuclease activity of Sae2. Lane 1: Control reaction of  $^{32}\text{P}$ -labeled dsDNA in the absence of Sae2; Lane 2: same as Lane 1 but with 3  $\mu\text{M}$  ScRev7; Lane 3: same as Lane 1 but with 0.3  $\mu\text{M}$  Sae2; Lanes 4–8: same as Lane 3 but with increasing concentrations of ScRev7 at 0.05, 0.25, 0.5, 1.0, and 3.0  $\mu\text{M}$ , respectively. (D) Quantification of the endonuclease activity catalysed by Sae2 from panel C. The closed triangles on the top of gel images in panels (A), and (C), represent increasing concentrations of Sae2 or ScRev7 respectively. Error bars indicate SEM, and data are representative of three independent experiments.

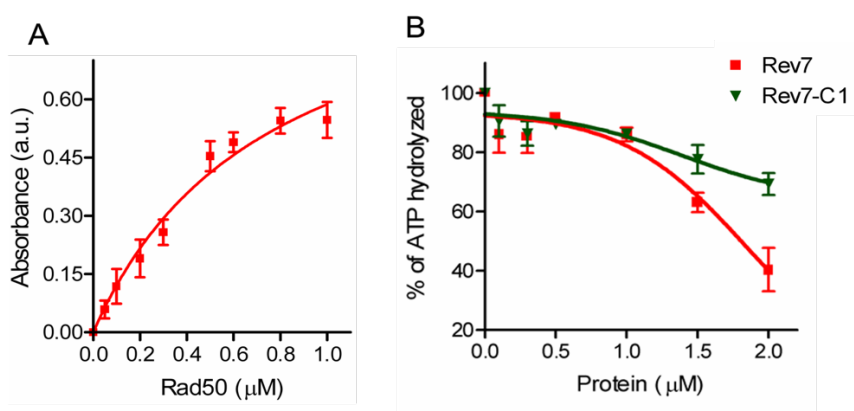


**Figure 6—figure supplement 1. ScRev7 inhibits the ATPase activity of ScRad50.** ATPase activity was measured using malachite green phosphate detection assay that quantifies the amount of Pi released upon ATP hydrolysis. (A) Increasing concentrations of ScRad50 (0, 0.05, 0.1, 0.2, 0.3, 0.5, 0.6, 0.8 and 1  $\mu\text{M}$ ) were incubated with reaction mixtures containing 20 mM Tris-HCl, pH 7.5, 50 mM KCl, 5% glycerol, 0.1 mM DTT, 0.2 mg/ml BSA, 150  $\mu\text{M}$  ATP and 1 mM MgCl<sub>2</sub>. Absorbance values were then monitored spectrophotometrically at 620 nm. (B) Same as (A), but fixed concentrations of ScRad50 (0.25  $\mu\text{M}$ ) were pre-incubated with increasing concentrations of ScRev7 or ScRev7-C1 (0, 0.1, 0.3, 0.5, 1, 1.5, 2  $\mu\text{M}$ ). The graphs were generated by non-linear regression analysis using GraphPad Prism (V. 5.0). Error bars represent standard deviation of data from two independent experiments.

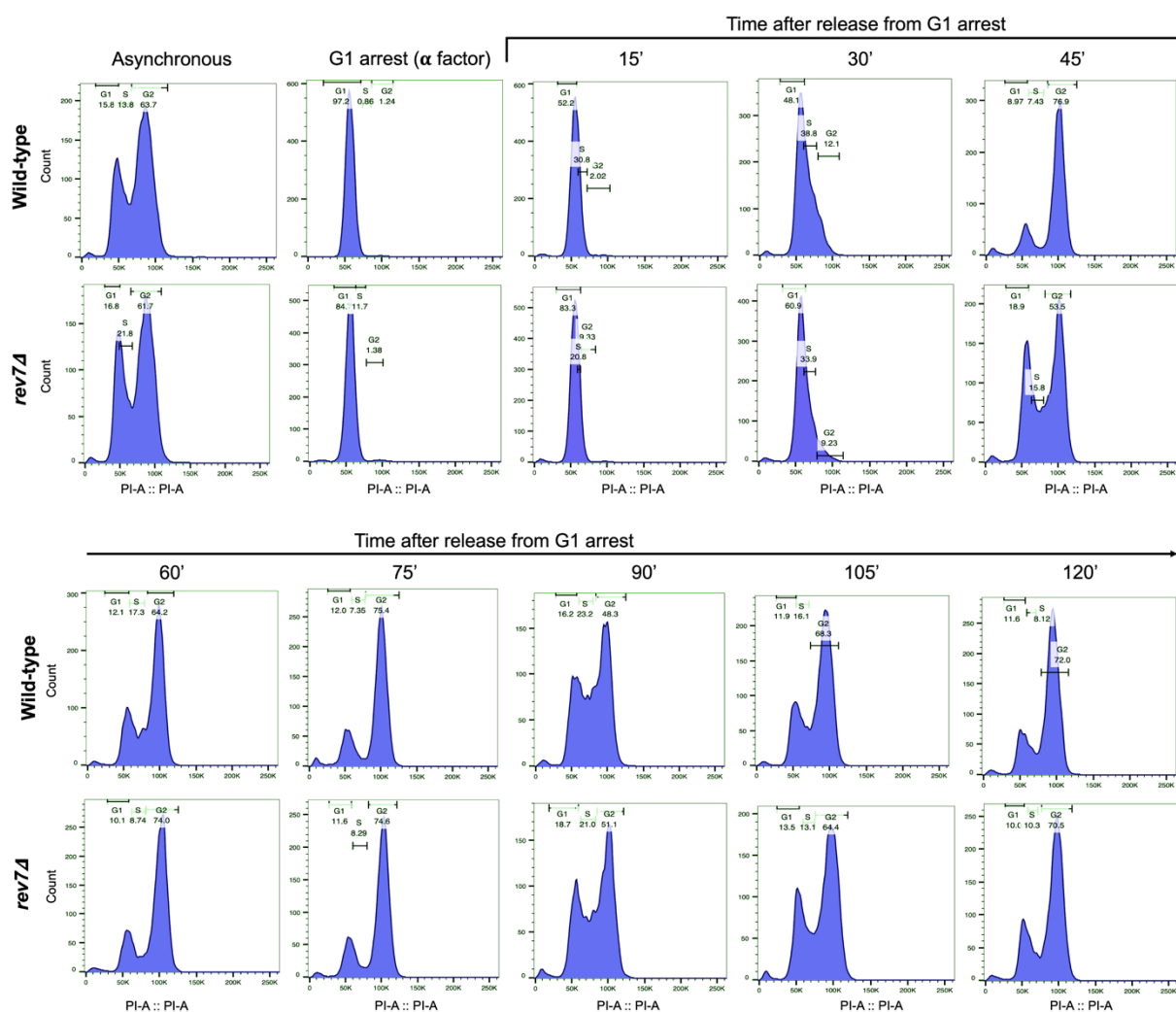


**Figure 7—figure supplement 1. Cell cycle analysis of wild-type and *rev7Δ* cells.** Cell cycle progression in wild-type and *rev7Δ* cells was analyzed by synchronizing an equal number of cells at the G1 phase using α-factor (100 ng/mL) in the growth medium. After releasing cells from G1 arrest, they were collected at specified time points and stained with propidium iodide for fluorescence-activated cell sorting (FACS) analysis. The histograms illustrate the distribution of cells in the G1, S, and G2 phases of the cell cycle for both wild-type and *rev7Δ* strains. Results shown are representative of two independent experiments.

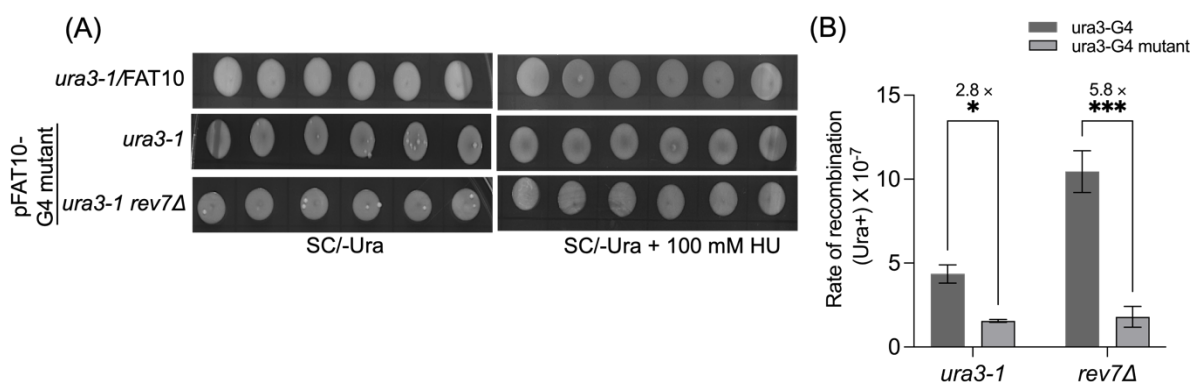


**Figure 9—figure supplement 1.** Mutation of G-quadruplex-forming sequences markedly attenuate the rate of HR frequency in *rev7Δ* cells. (A) Representative images showing *Ura3*<sup>+</sup> papillae on SC/-Ura agar plates in the absence or presence of 100 mM HU. Cells were imaged after six days of growth at 30 °C. (B) Quantification of the rate of HR frequency in *ura3-1* and *ura3-1 rev7Δ* strains carrying plasmids with unmutated and mutated *ura3*-G4 inserts in the absence of HU. Data are presented as mean ± SD from three different experiments. n.s., not significant, \* $p < 0.05$ , and \*\*\* $p < 0.001$  vs. control, as assessed using two-way ANOVA and Sidaks multiple comparison test.

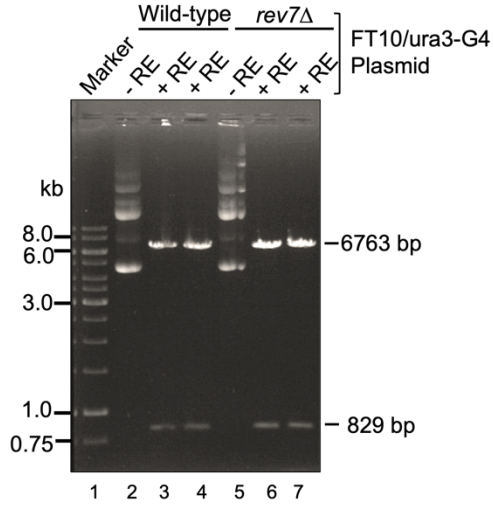


**Figure 9—figure supplement 2.** G-quadruplex capable sequences are stable in *rev7 $\Delta$*  cells during the HR assay. Total plasmid pFAT10-G4 DNA was isolated from cultures of WT and *rev7 $\Delta$*  cells. Samples of undigested and BamHI and Sph1 digested plasmid pFAT10-G4 DNA were analyzed by electrophoresis on a 0.6 % agarose gel and visualized after staining with ethidium bromide. Lane1: DNA marker; 2 and 5, represent undigested plasmid DNA from the WT and *rev7 $\Delta$*  cells respectively. Lanes 3 and 4, plasmid pFAT10-G4 DNA from the WT cells digested by BamHI and Sph1; 6 and 7, same as lane 3 and 5, but plasmid isolated from *rev7 $\Delta$*  cells. + RE and -RE indicate DNA digested by BamHI and Sph1 and undigested plasmid DNA respectively.

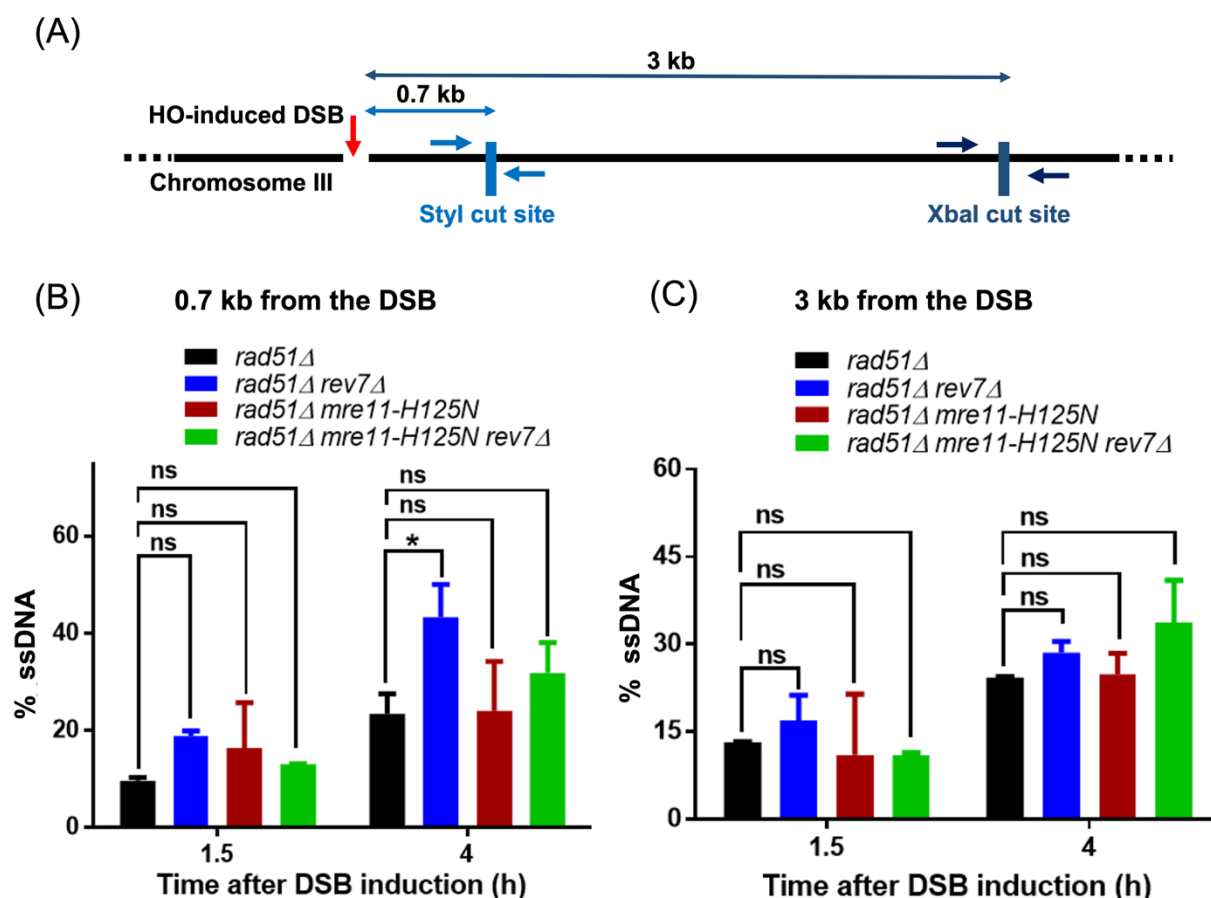


**Figure 9—figure supplement 3 Deletion of Rev7 enhances the speed of short-range end-resection in *S. cerevisiae*.** (A) Schematic diagram represents the positions of StyI (0.7 kb) and XbaI (3 kb) restriction sites with respect to HO endonuclease-induced DSB at the Chromosome III *MAT* locus. Arrows flanking the restriction sites mark the binding sites of forward and reverse primers used for qPCR analysis. The 5'—3' end-resection was physically assessed in the indicated strains by quantifying the percentage of ssDNA generated at 1.5 h and 4 h post induction of DSB, at a distance of (B) 0.7 kb and (C) 3 kb from the DSB. Two-way ANOVA was performed to determine the statistical significance of the datasets and graphs were generated using GraphPad Prism (Version 5.0). Data is representative of two independent biological replicates. ns, not significant.

## Supplementary Tables

**Table S1.** Inter-atomic distances and confidence parameters of amino acid residues mediating Rev7-Mre11 interactions.

Mre11 (position of amino acid residue)	Rev7 (position of amino acid residue)	Distance (Å)	Mre11-residue	Rev7-residue	Mre11-pLDDT	Rev7-pLDDT
A_0181	B_0206	0.73	ARG	ASP	74.44	65.25
A_0062	B_0126	1.14	LYS	MET	77.81	71.25
A_0130	B_0242	1.27	GLY	GLY	42.81	20.97
A_0134	B_0241	1.36	LEU	PHE	72.12	22.19
A_0131	B_0242	1.38	ASP	GLY	42.41	20.97
A_0132	B_0241	1.86	SER	PHE	51.47	22.19
A_0130	B_0243	2.16	GLY	SER	42.81	20.88
A_0130	B_0241	2.23	GLY	PHE	42.81	22.19
A_0131	B_0241	2.23	ASP	PHE	42.41	22.19
A_0679	B_0082	2.24	LYS	LYS	26.53	81.81
A_0131	B_0240	2.52	ASP	ILE	42.41	26.36
A_0130	B_0130	2.74	GLY	LYS	42.81	72.25
A_0181	B_0207	2.77	ARG	VAL	74.44	63.84

Residues highlighted in green are present in the C-terminal safety-belt region of Rev7 protein.

**Table S2.** Inter-atomic distances and confidence parameters of amino acid residues mediating Rev7-Rad50 interactions

Rad50 (position of amino acid residues)	Rev7 (positions of amino acid residues)	Distance (Å)	Rad50-residue	Rev7-residue	Rad50-pLDDT	Rev7-pLDDT
A_0603	B_0188	1.26	ARG	ASP	73.56	51.81
A_0582	B_0156	1.45	LYS	LEU	73	69
A_0599	B_0084	1.88	HIS	ASN	73.56	68.56
A_0596	B_0184	2.3	LYS	GLU	75.75	62.81
A_1132	B_0245	2.5	LYS	PHE	81	18.19
A_0581	B_0172	2.58	GLN	GLU	72.12	80.44
A_1129	B_0245	2.6	VAL	PHE	79	18.19
A_0599	B_0085	2.78	HIS	ASP	73.56	74.62
A_0577	B_0168	2.85	GLU	LYS	71.31	77.94
A_0603	B_0189	2.85	ARG	ASN	73.56	46.66

Residues highlighted in green are present in the C-terminal safety-belt region of Rev7 protein.

**Table S3.** The exact p-values for Figure 7B. The p-values were obtained by comparing the percentage of non-homologous end-joining observed for the indicated single- or double-gene deletions versus either the wild-type (WT) or *rev7Δ* strain, using non-parametric one-way ANOVA Dunnett test.

Reference strain	Strain	p-values
<b>WT</b>	<i>rev1Δ</i>	0.0461
	<i>rev3Δ</i>	0.0011
	<i>rev7Δ</i>	<0.0001
	<i>mre11Δ</i>	<0.0001
	<i>sae2Δ</i>	0.7111
	<i>rev1Δ rev3Δ</i>	<0.0001
	<i>rev1Δ rev7Δ</i>	<0.0001
	<i>rev3Δ rev7Δ</i>	<0.0001
	<i>mre11Δ rev7Δ</i>	<0.0001
	<i>sae2Δ rev7Δ</i>	<0.0001
<b>rev7Δ</b>	<i>rev7-C1</i>	<0.0001
	<i>rev7-42</i>	0.9910
	<i>rev1Δ rev7Δ</i>	0.2731
	<i>rev3Δ rev7Δ</i>	0.9958
	<i>mre11Δ rev7Δ</i>	0.0029
	<i>sae2Δ rev7Δ</i>	0.2220
	<i>rev7-C1</i>	0.0022
	<i>rev7-42</i>	<0.0001

**Table S4.** The exact p-values for Figure 8B. The p-values were obtained by comparing the percentage of non-homologous end-joining observed for the indicated single- or double-gene deletions versus either the wild-type (WT) or *rev7Δ* strain, using non-parametric one-way ANOVA Dunnett test.

Reference strain	Strain	p-values
<b>WT</b>	<i>rev7Δ</i>	<0.0001
	<i>mre11Δ</i>	<0.0001
	<i>ku70Δ</i>	<0.0001
	<i>rev1Δ</i>	0.0046
	<i>rev3Δ</i>	0.0009
	<i>rev7-C1</i>	<0.0001
	<i>rev7-42</i>	0.369
	<i>rev7-C1</i>	0.3664
<b>rev7Δ</b>	<i>rev7-42</i>	0.0002

**Table S5.** *S. cerevisiae* strains used in this study.

Strain	Genotype	Source
W1588-4C	<i>MATa ura3-1 trp1-1 leu2-3 112 his3-11 15 ade2-1 can1-100 ybp1-1 RAD5<sup>+</sup></i>	Paeschke <i>et al.</i> , 2011
KP013	<i>MATa ura3-1 trp1-1 leu2-3 112 his3-11 15 ade2-1 can1-100 ybp1-1 RAD5<sup>+</sup> bar1Δ::HIS3</i>	Paeschke <i>et al.</i> , 2011
KMY017	<i>MATa ura3-1 trp1-1 leu2-3 112 his3-11 15 ade2-1 can1-100 ybp1-1 RAD5<sup>+</sup> bar1Δ::HIS3 rev7Δ::kanMX4</i>	This Study
KMY042	<i>MATa ura3-1 trp1-1 leu2-3 112 his3-11 15 ade2-1 can1-100 ybp1-1 RAD5<sup>+</sup> bar1Δ::HIS3 rev1Δ::hphNT1</i>	This Study
KMY061	<i>MATa ura3-1 trp1-1 leu2-3 112 his3-11 15 ade2-1 can1-100 ybp1-1 RAD5<sup>+</sup> bar1Δ::HIS3 rev3Δ::KanMX4</i>	This Study
KMY018	<i>MATa ura3-1 trp1-1 leu2-3 112 his3-11 15 ade2-1 can1-100 ybp1-1 RAD5<sup>+</sup> bar1Δ::HIS3 mre11Δ::hphNT1</i>	This Study
KMY141	<i>MATa ura3-1 trp1-1 leu2-3 112 his3-11 15 ade2-1 can1-100 ybp1-1 RAD5<sup>+</sup> bar1Δ::HIS3 rev7Δ::rev7-C1 (203-245 aaΔ)-9MYC-hphNT1</i>	This Study
KMY143	<i>MATa ura3-1 trp1-1 leu2-3 112 his3-11 15 ade2-1 can1-100 ybp1-1 RAD5<sup>+</sup> bar1Δ::HIS3 rev7Δ::rev7-42 (1-203 aaΔ)-3MYC-KANMX4</i>	This Study
LSY1375	<i>MATa ura3-1 trp1-1 leu2-3 112 his3-11 15 ade2-1 can1-100 ybp1-1 RAD5<sup>+</sup> mre11-D56N, H125N</i>	Krogh <i>et al.</i> , 2005
LSY1091	<i>MATa ura3-1 trp1-1 leu2-3 112 his3-11 15 ade2-1 can1-100 ybp1-1 RAD5<sup>+</sup> sae2Δ::kanMX6</i>	Krogh <i>et al.</i> , 2005
KMY058	<i>MATa ura3-1 trp1-1 leu2-3 112 his3-11 15 ade2-1 can1-100 ybp1-1 RAD5<sup>+</sup> bar1Δ::HIS3 rev1Δ::hphNT1 rev3Δ::KanMX4</i>	This Study
KMY059	<i>MATa ura3-1 trp1-1 leu2-3 112 his3-11 15 ade2-1 can1-100 ybp1-1 RAD5<sup>+</sup> bar1Δ::HIS3 rev7Δ::kanMX4 rev3Δ::hphNT1</i>	This Study
KMY048	<i>MATa ura3-1 trp1-1 leu2-3 112 his3-11 15 ade2-1 can1-100 ybp1-1 RAD5<sup>+</sup> bar1Δ::HIS3 rev1Δ::hphNT1 rev7Δ::kanMX4</i>	This Study
KMY050	<i>MATa ura3-1 trp1-1 leu2-3 112 his3-11 15 ade2-1 can1-100 ybp1-1 RAD5<sup>+</sup> rev7Δ::kanMX4 mre11Δ::hphNT1</i>	This Study
KMY053	<i>MATa ura3-1 trp1-1 leu2-3 112 his3-11 15 ade2-1 can1-100 ybp1-1 RAD5<sup>+</sup> mre11-D56N, H125N rev7Δ::kanMX4</i>	This Study
KMY060	<i>MATa ura3-1 trp1-1 leu2-3 112 his3-11 15 ade2-1 can1-100 ybp1-1 RAD5<sup>+</sup> sae2Δ::kanMX6 rev7Δ::hphNT1</i>	This Study
KP038	<i>MATa ura3-52 lys2-801 ade2-101 trp1-Δ63 his1-Δ200 leu2-Δ1 pif1-m2</i>	Paeschke <i>et al.</i> , 2011
YW714	<i>MATα ade2::SD2-::URA3 his31 leu20 ura30</i>	Karathanasis and Wilson,

		2002
KMY136	<i>MATα ade2::SD2-::URA3 his31 leu20 ura30 rev7Δ::hphNT1</i>	This Study
KMY137	<i>MATα ade2::SD2-::URA3 his31 leu20 ura30 mre11Δ::hphNT1</i>	This Study
KMY144	<i>MATα ade2::SD2-::URA3 his31 leu20 ura30 rev1Δ::hphNT1</i>	This Study
KMY145	<i>MATα ade2::SD2-::URA3 his31 leu20 ura30 rev3Δ::hphNT1</i>	This Study
KMY146	<i>MATα ade2::SD2-::URA3 his31 leu20 ura30 rev7Δ::REV7-C1 (203-245 aaΔ)-9MYC-hphNT1</i>	This Study
KMY147	<i>MATα ade2::SD2-::URA3 his31 leu20. ura30 rev7Δ::REV7-42 (1-203 aaΔ)-3MYC-KANMX4</i>	This Study
PJ69-4A	<i>MATα trpl-901 leu2-3,112 ura3-52 his3-200 ga14Δ ga180Δ LYS2::GALI-HIS3 GAL2-ADE2 met2::GAL7-lacZ</i>	James <i>et al.</i> , 1996
KMY023	<i>MATα trpl-901 leu2-3,112 ura3-52 his3-200 ga14Δ ga180Δ LYS2::GALI-HIS3 GAL2-ADE2 met2::GAL7-lacZ rev3Δ::hphNT1</i>	This Study
KMY139	<i>MATα trpl-901 leu2-3,112 ura3-52 his3-200 ga14Δ ga180Δ LYS2::GALI-HIS3 GAL2-ADE2 met2::GAL7-lacZ mre11Δ::KANMX4 rad50Δ::URA3 xrs2Δ::HphNT1</i>	This Study
BJ5464	<i>MATα ura3-52 trp1 leu2-Δ1 his3-Δ200 pep4::HIS3 prb1-Δ1.6R can1 GAL</i>	Johnson <i>et al.</i> , 2006
LSY2172-24C	<i>MATα rad51::LEU2 ade3::GAL1-HO</i>	Mimitou and Symington, 2010
LSY2265-10D	<i>MATα rad51::LEU2 mre11-H125N::URA3::mre11-H125N ade3::GAL1-HO</i>	Mimitou and Symington, 2010
KMY170	<i>MATα rad51::LEU2 ade3::GAL1-HO rev7Δ::kanMX4</i>	This study
KMY171	<i>MATα rad51::LEU2 mre11-H125N::URA3::mre11-H125N ade3::GAL1-HO rev7Δ::kanMX4</i>	This study

**Table S6.** Sequences of primers

Primer names	Sequence (5'—3')	Plasmid DNA/primers
OSB01-FP	<b>GC GGATCC ATGAATAGATGGGTAGAGAAGTG</b>	pET28a_ScREV7, pET28a_ScREV7-C1
OSB02-RP	<b>GCAAGCTT CTTCAAATT CATTTCATT TTGCAC</b>	pET28a_ScREV7
OSB03-FP	<b>CATATG ATGAATAGATGGGTAGAGAAGTG</b>	pGBK7_ScREV7, pGADT7_ScREV7
OSB04-RP	<b>GGATC CT TCTCAA ATT CATTTCATT TTGCAC</b>	pGBK7_ScREV7, pGADT7_ScREV7

OSB05-FP	ATGCCT <b>CATATG</b> ATGGACTATCCTGATCCAGACAC ACAATAAGG	pGADT7_ScMRE11
MRE11_RP	ATGCCT <b>GAATT</b> CCTATTTCTTTCTTAGGAAGGAG GACTTCC	pGADT7_ScMRE11
OSB11-FP	ATCCAAGAAGAAAAAAAAATAGTAATCGTTGCGT CAGCTTATGCGTACGCTGCAGGTCGAC	REV7 Knockout
OSB12-RP	ACATTAATTAAATTCCATTCTCAAATTTCATT TGCACCTAACGATGAATTGAGCTCG	REV7 Knockout
OSB13-FP	ATATGCATATACGTCTACACTAC	REV7 Knockout
OSB14-RP	CTGCAGCGAGGAGGCCGTAAT (KANB)	REV7 Knockout
OSB33-FP	CGCG <b>GATCC</b> ATGAGCGCTATCTATAAATTATC	pESUMO_ScRAD50
OSB34-RP	CCGCTCGAGTCAATAAGTGACTCTGTTAATATC	pESUMO_ScRAD50 & pGADT7_ScRAD50
OSB35-FP	CCGG <b>AATT</b> CATGAGCGCTATCTATAAATTATC	pGADT7_ScRAD50
OSB36-FP	GGAATT <b>CCATATG</b> TGTTGGTAGTACGATACCAG	pGADT7_ScXRS2
OSB37-RP	<b>CGGGATC</b> CTTATCCTTTCTTCTTGA	pGADT7_ScXRS2
OSB52-FP	ATTGACGCAAGTTGTACCTGCTCAGATCCGATAAA ACTCGACTATGCGTACGCTGCAGGTCGAC	MRE11 Knockout
OSB53-RP	TGGTTATAAATAGGATATAATATAATAGGGATCA AGTACAACTAATCGATGAATTGAGCTCG	MRE11 Knockout
OSB54-FP	AAGGCATCTACAAATCTCATTG	MRE11 Knockout
OSB133-FP	AGGCAAAATCACAAATTGAGTGGGTCGATATTAA CAGAGTCACTTATCGTACGCTGCAGGTCGAC	RAD50 Knockout
OSB075-RP	TAATTAAATCAATCAAAGTCTATCCCTCGTAGATAT TATGGGTCTTATCGATGAATTGAGCTCG	RAD50 Knockout
OSB076-RP	TCCTGGTTAACACGGTG	RAD50 Knockout
OSB134-FP	ACGACGACGATGACGACGGTCCGAAGTTACGTT CAAAAGAAGAAAAGGACGTACGCTGCAGGTCGAC	XRS2 Knockout
OSB078-RP	TGCAAAATATAATTAAATGAAATTGAAATACTCGG AAAATTATCATTAATCGATGAATTGAGCTCG	XRS2 Knockout
OSB079-RP	TTGGAGTATTCAAAGAGGGCTAC	XRS2 Knockout
OSB55-FP	TTCTCAAAATAATCGATACTGCATTTCTAGGCATA TCCAGCGATGCGTACGCTGCAGGTCGAC	REV1 Knockout
OSB56-FP	AACTGCGTCTTACTGTATGCTGAAATGTTTTTT TTTTAATTCAATCGATGAATTGAGCTCG	REV1 Knockout
OSB57-FP	TTTACACAGACCAAGACGG	REV1 Knockout
OSB58-FP	TCAATACAAA <b>ACTACAAGTTGGCGAAATAAAAT</b> GTTTGGAAATGCGTACGCTGCAGGTCGAC	REV3 Knockout
OSB59-RP	ACAAATAACTACTCATTTGCGAGACATATCTG TGTCTAGATTAATCGATGAATTGAGCTCG	REV3 Knockout
OSB60-FP	ATCCCTGTGGCTCCTACC	REV3 Knockout
OSB116-FP	ATCCAAGAAGAAAAAAAATAGTAATCGTTGCGT CAGCTTATGAATAGATGGTAGAGAAGTG	rev7-c1 truncation (rev7-c1-9MYC-hphNT1)
OSB117-RP	GTCGACCTGCAGCGTACGGACTAAAGAAGTGAGT TTTATTTAGG	rev7-c1 truncation (rev7-c1-9MYC-hphNT1)
OSB118-FP	CCTAAAATAAA <b>ACTCACTCTTAGTCCGTACGCTG</b> CAGGTCGAC	rev7-c1 truncation (rev7-c1-9MYC-

		hphNT1)
OSB070-RP	TACTTAGAGACATTTAATTAAATTCCATTCTTCAAA TTTCATTTGCACTTAACATCGATGAATTGAGCTCG	rev7-c1 truncation (rev7-c1-9MYC- hphNT1)
OSB122-FP	ATCCAAGAAGAAAAAAAAAAATAGTAATCGTTGCGT CAGCTTATGGTTCTGACGTGGGCC	rev7-42 aa truncation (rev7-42-3MYC- KANMX)
OSB120-RP	GTCGACCTGCAGCGTACGAAACAAAGATCCAAAAA TGCTC	rev7-42 aa truncation (rev7-42-3MYC- KANMX)
OSB121-FP	GAGCATTGGATCTTGTTCGTACGCTGCAGG TCGAC	rev7-42 aa truncation (rev7-42-3MYC- KANMX)
OSB61-FP	GGAATTCCATATGTCATTCACCTGCCGCAGTTC	pGBK7_REV7-N1
OSB62-FP	GGAATTCCATATGACCCACGTTACAGATTTCC	pGBK7_REV7-N2
OSB63-FP	GGAATTCCATATGTTGAACTAGGACATAAGTTGG	pGBK7_REV7-N3
OSB64-RP	CGGGATCCTTAGACTAAAGAAGTGAGTTTATT AGG	pGBK7_REV7-C1
OSB65-RP	CGGGATCCTTATTCTGCTTTCTCCAAACTATC	pGBK7_REV7-C2
OSB66-RP	CGGGATCCTACAATTGATCGCATTAATAACTGC	pGBK7_REV7-C3
OSB80-FP	CGGGATCCATGTCGAAAGCTACATATAAG	pFAT10_ura3-G4
OSB81-RP	CCCGGTCCCCCAACGACAACACCCCAATCAACCA ATCGAACCTTC	pFAT10_ura3-G4
OSB82-FP	GGGTGTTGTCGTTGGGGGACCGGGATGACACC CGGTGTGGG	pFAT10_ura3-G4
OSB83-RP	ACATGCATGCTTAGTTGCTGCCGCATC	pFAT10_ura3-G4
OSB129-RP	CTCATAGCATCCAACGACAACACGCAATCAACCAA TCGTAACCTTC	pFAT10_ura3-G4 mutant
OSB130-FP	GCGTGTGTTGGATGCTATGAGATGACACCC GGTGTGGG	pFAT10_ura3-G4 mutant
OSB125-RP	GCAAGCTTTAGACTAAAGAAGTGAGTTTATT GG	pET28_ScRev7-C1
REV7GFP-FP	GCTCTAGAATGAATAGATGGGTAGAGAAG	pPROEX_ScREV7-eGFP
REV7GFP-RP	CCGCTCGAGGTTAATTAAACCCGGGGATCCGAAAC AAAGATCCAAAATGC	pPROEX_ScREV7-eGFP
OSB150-FP	ATGCCTCATATGATGGTACTGGTGAAG	pGADT7-SAE2
OSB151-RP	ATGCCTGAATTCTAACATCTTAGCATATA	pGADT7-SAE2
OSB152-RP	CCGCTCGAGGTTAATTAAACCCGGGGATCCGGACT AAAGAAGTGAGTTTATTAGG	pPROEX_ScREV7C1-eGFP

The bold letters correspond to restriction sites.

**Table S7.** Sequences of oligonucleotides used in the preparation of DNA substrates.

Oligonucleotide name	Sequence (5'—3')
----------------------	------------------

OSB 17 Duplex-41 bp	GCCGTGATCACCAATGCAGATTGACGAACCTTGCCCACGT
OSB 20 Duplex-41 bp	ACGTGGGCAAAGGTTCGTCAATCTGCATTGGTGATCACGGC
OSB 41 Duplex-60 bp	GGGTGAACCTGCAGGTGGCAAAGATGTCCTAGCAATGTAATCGT CAAGCTTATGCCGT
OSB 42 Duplex-60 bp	ACGGCATAAAGCTTGACGATTACATTGCTAGGACATCTTGCCCAC CTG CAGGTTCACCC
OSB28 (4G3) G4-DNA	AATTCT <u>GGGTGTGT</u> <u>GGGTGTGT</u> <u>GGGTGTGT</u> <u>GGGTGTGG</u>
OSB 92 (TP) G4-DNA	TGGACCAGACCTAGCAGCTAT <u>GGGGGAGCT</u> <u>GGGGAAAGGT</u> <u>GGGAA</u> TGTGA
ODN 6G3 G4-DNA	AATTCT <u>GGGTGTGT</u> <u>GGGTGTGT</u> <u>GGGTGTGT</u> <u>GGGTGTGT</u> <u>GGGTGTGG</u>
OSB132 (TP-G4mutant)	TGGACCAGACCTAGCACTATCTGCAAGTCAAGTTGACTACGTATAC ATA

**Table S8. Primers used for qPCR analysis.**

Primer	Sequence (5'—3')
0.7 kb (Forward)	TTTAGGATACTTCACGCTTTA
0.7 kb (Reverse)	TTAGCTTGTACCAAGAGGAA
3 kb (Forward)	GTCGTTCATATCTAAAGGAGTTAT
3 kb (Reverse)	CCTACCGCACCTTCTAAG
PRE1 (Forward)	AAATCTTACGGTGGCAA
PRE1 (Reverse)	CGCTAGAACATGACAGAACATCC
HO efficiency (Forward)	TCAATGATTAAAATAGCATAGTCGGGT
HO efficiency (Reverse)	CGTCAACCACTCTACAAAACCA